Doctorate Dissertation

博士論文

Collapse of the $\mathsf{N} = 28$ shell closure: single-particle structure of ^{43}S

(中性子数28における閉殻の消失: ^{43}Sの単一粒子構造)

A Dissertation Submitted for Degree of Doctor of Philosophy
December 2018

平成30年12月博士(理学)申請
Department of Physics, Graduate School of Science,
The University of Tokyo

東京大学大学院理学系研究科物理学専攻

Satoru Momiyama
籾山 悟至

Abstract

Thanks to the improvement of techniques to produce the unstable nuclei far from the valley of stability, the erosion of the well-established magic numbers and emergence of new ones in the atomic nuclei have been observed. In the neutron-rich nuclei below ^{48}Ca on the nuclear chart, the neutron shell gap at $N = 28$ has been found to be reduced and especially on ^{44}S and ^{43}S, the shape coexistence and coexistence/mixing of the different neutron configurations in the wave function has been discussed both theoretically and experimentally. Unless a number of efforts about the macroscopic nuclear system, however, the microscopic information about the neutron configuration of these nuclei has been unknown, which keeps the mechanism of the disappearance of the $N = 28$ magic number and the emergence of the deformed state in this region unclear.

To solve this problem, an in-beam γ-ray spectroscopy utilizing the one-neutron knockout reaction from ^{44}S to ^{43}S was performed in this thesis work. This reaction channel can selectively populate the neutron single-hole state and the excitation energies and cross sections of final states populated in this reaction reflect the evolution of the neutron single-particle orbits. One of the specific problem about these nuclei is that there is a low-lying isomeric state in ^{43}S which makes it difficult to distinguish if observed prompt γ-rays decay directly to the ground state or to this isomeric state.

In the experiment of this thesis work, the secondary beam of ^{44}S, produced by the accelerator complex of K500 and K1200 and the fragment separator A1900, bombarded a ^{9}Be secondary target. The prompt γ-rays emitted from the reaction residue was detected by the GRETINA array surrounding the target. The reaction residue passed through the S800 spectrograph where the particle identification and the measurement of the momentum was performed. At the very end of the S800, 32 CsI(Na) detector array, IsoTagger, was placed and the de-excitation from the isomeric state was observed.

The full level scheme of ^{43}S was constructed for the first time. By the analysis of parallel momentum distributions with the eikonal reaction theory, the assignment of the spin-parity of each final state was performed. The concentration of the strength of neutron knockout from $l = 1$ orbit was observed around 1.2 MeV, which is the direct observation of the quenching of the $N = 28$ shell gap microscopically. Through the comparison with the shell model calculations, the discussion about the neutron configuration in the three possible different bands in ^{43}S was attempted. Also it was suggested that the stronger cross-shell tensor force can explain the large neutron occupation beyond $N = 28$ shell gap like observed in the present work

Contents

Abstract **iii**

1 Introduction **1**
1.1 Nuclear structure 1
1.2 The erosion of the $N = 28$ magic number 5
1.3 Thesis objective and outline 9

2 Theoretical background **13**
2.1 Nuclear forces 13
2.2 Treatment of nuclear many-body system 15
2.2.1 Description of many-body states 15
2.2.2 Hartree-Fock calculation 16
2.2.3 Shell model calculation (configuration interaction) 16
2.2.4 Effective interactions for shell model 18
2.3 Theory of one-neutron knockout reaction 18
2.3.1 Factorization of the cross section 19
2.3.2 The eikonal reaction theory 20
2.3.3 Optical potential 21
2.3.4 Densities and form factors 23
2.3.5 Reaction mechanisms and cross sections 24
2.3.6 Momentum distributions 25
2.3.7 Reduction factor 26

3 Experimental setup **29**
3.1 Production of radioactive beam 29
3.2 The A1900 fragment separator 30
3.3 The S800 spectrograph 31
3.3.1 Particle trajectories 33
3.3.2 Time-of-flight 34
3.3.3 Ionization chamber 34
3.4 Gamma-ray detectors 35
3.4.1 The GRETINA array 35
3.4.2 The IsoTagger array 37
3.5 Readout and data acquisition system 38

4 Analysis **43**
4.1 S800 43
4.1.1 Cathode readout drift chambers 43
4.1.2 Time-of-flight 45
4.1.3 Ionization chamber 46
4.2 Analysis for GRETINA 47
4.2.1 Energy recalibration 48
4.2.2 Treatment of γ-ray event and addback analysis 50

4.2.3 Simulation of response function and deduction of efficiency . . . 52
4.2.4 Doppler correction 55
4.2.5 Treatment of background 56
4.3 Analysis for IsoTagger 57
4.3.1 Energy calibration 58
4.3.2 Timing calibration 60
4.3.3 Simulation of response function and deduction of efficiency . . . 60
4.4 Analysis on momentum distribution 63

5 Results **69**
5.1 Particle identification 69
5.2 Gamma-ray energy histograms 71
5.2.1 Prompt gamma-rays 71
5.2.2 Delayed gamma-rays 77
5.3 Parallel momentum distribution 81
5.4 Cross section 85

6 Discussion **87**
6.1 Level and decay scheme 87
6.2 Spectroscopic factors 92

7 Summary and outlook **99**

Acknowledgements **101**

Bibliography **103**

List of Figures

1.1 The nuclear chart (element or proton number Z versus neutron number N). . . . 2
1.2 The difference of the binding energy between experiment and the semi-empirical mass formula. . . . 3
1.3 Example of the calculation of single-particle orbits. . . . 4
1.4 Experimental $E(2^+)$ and $B(E2; 0^+ \to 2^+)$ in the $Z = 12$ to 20 isotopic chains against the neutron number N. . . . 6
1.5 Level scheme of ^{44}S constructed by [19]. . . . 7
1.6 ^{44}S wave function of the symmetry conserving configuration mixing calculation plotted in the (β, γ) plane. . . . 8
1.7 ^{43}S level scheme of the shell model calculation with the SDPF-U interaction. . . . 9
1.8 Nilsson orbits of the neutrons in ^{45}S. . . . 10
1.9 ^{43}S level scheme deduced by the previous one-neutron knockout experiment. . . . 11

2.1 Schematic picture of the monopole interaction of the tensor force. . . . 15
2.2 Schematics of the typical two mechanisms of the knockout reaction. . . . 24
2.3 Parallel momentum distributions calculated in the rest frame of the ^{44}S. 27
2.4 Compilation of the R_S against the difference of the proton and neutron separation energies. . . . 28

3.1 A schematic of the Coupled Cyclotron Facility and the A1900 fragment separator. . . . 29
3.2 A schematic of the S800 spectrograph. . . . 31
3.3 A schematic of the focal plane box of the S800. . . . 32
3.4 A schematic of the CRDC. . . . 33
3.5 A schematic of the crystal of the GRETINA array. . . . 35
3.6 Picture of the GRETINA mount. . . . 36
3.7 Picture of the IsoTagger array. . . . 37
3.8 Schematic diagram for the electric circuit of the CRDC detectors. . . . 38
3.9 Schematic diagram for the electric circuit of the PPAC detectors. . . . 39
3.10 Schematic diagram for the electric circuit of the ionization chamber. . 39
3.11 Schematic diagram for the electric circuit of the IsoTagger array. . . . 40
3.12 Schematic diagram for the electric circuit of the plastic scintillators for timing measurement. . . . 40

4.1 Gain matching of 224 channels of the downstream CRDC. . . . 44
4.2 CRDC mask calibration. . . . 44
4.3 Correction of CRDC y position vs time. . . . 45
4.4 Correction to the ToF with regard to the dispersive position (x) and dispersive angle (a) at the focal plane. . . . 46
4.5 Gain matching of 16 channels of ionization chamber. . . . 47

4.6 Position correction of ionization chamber. 47
4.7 Energy recalibration of a single crystal of GRETINA. 48
4.8 Energy recalibration of whole GRETINA array. 49
4.9 Example of the indication of the sub-segment position resolution of GRETINA. 51
4.10 Improvement of the peak-to-total ratio of prompt γ-rays with addback procedure of GRETINA. 51
4.11 Resolution and threshold functions of a single crystal of GRETINA. . 52
4.12 Efficiency of GRETINA without addback. 53
4.13 Efficiency of GRETINA with addback. 54
4.14 Ratio of simulated and measured efficiencies of GRETINA. 55
4.15 γ-ray energies versus measured timings in GRETINA for the one-neutron knockout setting. 57
4.16 γ-ray energy histogram of GRETINA before Doppler correction for the one-neutron knockout settings. 58
4.17 Result of energy calibration of IsoTagger in the one-neutron knockout setting. 59
4.18 Result of timing calibration of IsoTagger. 60
4.19 Resolution and threshold functions of each crystal of IsoTagger. 61
4.20 Efficiency deduction for the 320 keV isomeric transition. 62
4.21 Efficiency of whole IsoTagger array. 63
4.22 Measured charge value in PPAC for unreacted setting. 66
4.23 Correction on d_{ta} with regard to the PPAC x position. 67
4.24 Correction of d_{ta} and $P_{//}$ by the PPAC x position for unreacted and one-neutron knockout settings. 67

5.1 Particle identification plots for both incoming and outgoing particles. . 70
5.2 Particle identification plots for both incoming and outgoing particles for unreacted setting. 71
5.3 Estimation of the uncertainty due to the placement of the outgoing PID gate. 72
5.4 Prompt γ-ray energy histogram after Doppler correction for the one-neutron knockout reaction channel from ^{44}S to ^{43}S. 72
5.5 Fitting of response functions to the prompt gamma-ray energy histogram without addback. 73
5.6 Two dimensional γ-γ coincidence matrix. 75
5.7 Background subtracted γ-γ coincidence spectra in GRETINA. 76
5.8 Two possible partial level schemes constructed from prompt γ-γ coincidence in GRETINA. 77
5.9 Comparison of γ-γ coincidence spectra with the simulation. 78
5.10 Delayed γ-ray energy and timing spectra in one-neutron knockout reaction. 80
5.11 Background subtracted delayed coincidence spectrum between GRETINA and IsoTagger. 80
5.12 γ-ray energy histogram of $^{44}\mathrm{S} \rightarrow {}^{44}\mathrm{S}$ channel measured by the IsoTagger array. 81
5.13 Parallel momentum distributions of the one-neutron knockout reaction coincident with γ-rays. 83
5.14 $P_{//}$ of the ground state of ^{43}S populated in the one-neutron knockout reaction. 84
5.15 Acceptance plots of d_{ta} and a_{ta}. 84

5.16 Inclusive cross section deduced for each run. 86

6.1 Level schemes of ^{43}S deduced from the present experiment and predicted by shell model calculations. 88
6.2 Decay schemes of ^{43}S drawn separately for each band. 90
6.3 Systematics of the C^2S weighted energy centroids of the $f_{7/2}$ and $p_{3/2}$ orbits. 94
6.4 Influence of the tensor force on the level scheme of ^{43}S. 96

List of Tables

4.1 Standard radiation sources used for the calibration of the GRETINA. Values are taken from [101]. . . . 49
4.2 Observed background γ-rays related to the reaction with neutrons. . . . 58
4.3 Standard radiation sources used for the calibration of the IsoTagger. Values are taken from [101, 106]. . . . 59

5.1 Observed γ-ray energies, efficiency-corrected intensities, and coincidence information for ^{43}S. The errors of γ-ray energies and yields include only the statistical errors. . . . 79
5.2 Reduced χ^2 values for the theoretical momentum distribution compared to the experimental data. . . . 82
5.3 Inclusive and exclusive cross sections to bound final states. . . . 86

6.1 Calculated ESPEs of $p_{3/2}$ and $f_{7/2}$ orbits in Ca, Ar, and S isotopes at $N = 28$. . . . 96
6.2 Calculated C^2S sum of three different interactions. . . . 97

Terminology

N, Z	neutron and proton number
A	mass number $N + Z$
BE	binding energy
n	principal quantum number
l	orbital angular momentum
j	total angular momentum
s	spin of a nucleon
m	projection of j onto laboratory axis
t_z	isospin
K	projection of j onto intrinsic symmetry axis
J^π	spin-parity of a state
T	total isospin of nucleons
(β, γ)	deformation parameters
$npnh$	n-particle-n-hole excitation
ν, π	neutron and proton single particle orbit
$B(E2)$	reduced transition probability of $E2$ transition
$E(2_1^+)$	excitation energy of 2_1^+ state in even-even nucleous
C^2S	spectroscopic factor
$P_{//}$	parallel momentum
S_n, S_p	neutron and proton separation energy
g-factor	dimensionless magnetic moment
$B\rho$	magnetic rigidity
ToF	time-of-flight
PID	particle identification

Chapter 1

Introduction

1.1 Nuclear structure

The material around us is made of atoms. The idea that an atom consists of negatively-charged electrons and a nucleus which was proposed by Rutherford [1] based on the experiments of Geiger and Marsden [2]. Though more than a century has passed since the discovery of the nucleus, it still remains an interesting subject due to its complex nature.

The nucleus is made up of protons with positive charge and neutrons without electric charge, totally called nucleons. They are bound by the strong nuclear force which is attractive at short distances compensating the electric force which acts in long range and repulsively between protons. The average binding energy per nucleon amounts to about 5-10 MeV in almost all nuclei. Although the nucleus carries more than 99.9% of the mass of the atom, the nucleons are confined to an about 10^4 smaller region, a few fermi, compared to atoms which are on the order of Å in size. The nucleus is therefore a quantum system. Besides a nucleus is a many-body system, nucleons carry spin 1/2 and obey the Fermi-Dirac statistics, which results in the complex correlation that two nucleons are not simultaneously in the same state. Additionally, the nuclear force, a residual effect of the strong interaction between quarks, cannot be treated in a simple analytic form.

Despite the complexity mentioned above, there are some simple properties of the structure of the nucleus. Figure 1.1 is the nuclear chart whose X and Y axis correspond to the neutron number N and proton number Z for each nucleus. In this chart, black squares correspond to the stable elements. The collection of these elements is called the valley of stability. In the light mass region, this valley is located along $N = Z$ line but then goes to more neutron-rich region in the heavier mass region. This can be understood as the interplay between the short-range nuclear force which favors the strong proton-neutron combination and the repulsive Coulomb force which decreases the binding energy of a nucleus with increasing Z. An early attempt to model a nucleus is the Bethe-Weizsäcker formula for the binding energy based on the liquid drop model of the nucleus [4]. This model treats the nucleus as a drop of an incompressible fluid of protons and neutrons, in analogy to a drop of water of H_2O molecules. This formula consists of five terms. The volume term reflects the attractive force in the bulk, which is proportional to the volume or the number of nucleons A. Besides the Coulomb term for the repulsive force between protons, the surface term models the tension of the nuclear surface, which should be proportional to the surface area of the nucleus, $A^{2/3}$. Also, it is expected that nuclei with an equal number of protons Z and neutrons N have a lower energy than that with asymmetric Z and N for a given $A = Z + N$, called as the symmetry energy. Because a staggering of the binding energies between even and odd Z or N is observed, a pairing term is added and attractive for even Z

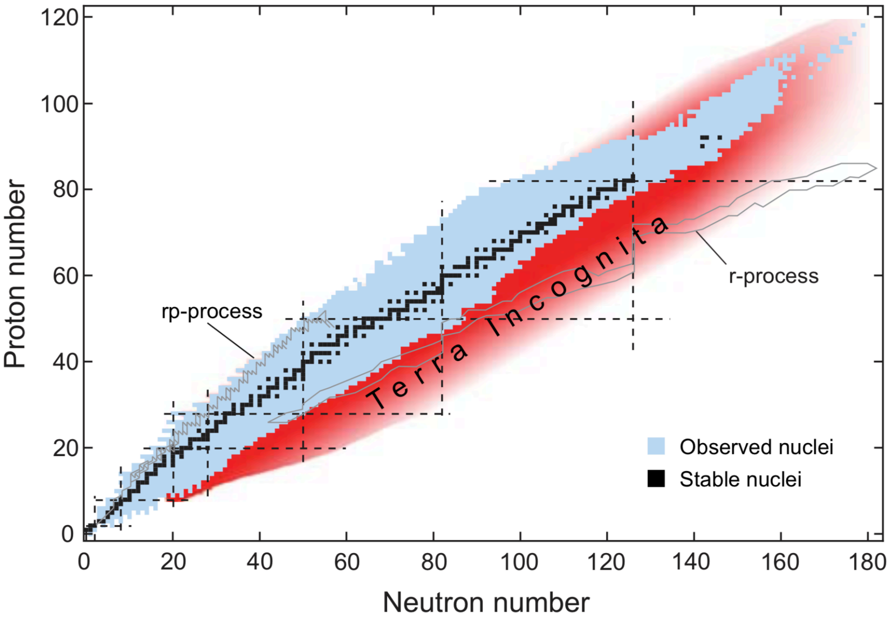

Figure 1.1: The nuclear chart (element or proton number Z versus neutron number N). Stable elements (valley of stability) are shown as black squares. The blue and red areas show the isotopes that have been experimentally and those that are predicted but not observed, respectively. Taken from [3].

and N and repulsive for odd Z and N,

$$\delta(N,Z) = \begin{cases} a_P A^{-1/2} & \text{odd } Z \text{ and odd } N, \\ -a_P A^{-1/2} & \text{even } Z \text{ and even } N, \\ 0 & \text{odd } A. \end{cases} \tag{1.1}$$

The resulting semi-empirical mass formula is

$$BE = a_V A - a_S A^{2/3} - a_C \frac{Z^2}{A^{1/3}} - a_A \frac{(N-Z)^2}{A} + \delta. \tag{1.2}$$

The five parameters in this formula are deduced by fitting to experimental data.

One of the features worth noting is that the binding energies of almost all nuclei are well reproduced within 10 MeV by this formula and that the binding energy per nucleon is about 8 MeV almost everywhere on the nuclear chart. In the Figure 1.2, however, it is clearly visible that nuclei with $N = 28,\ 50,\ 82,$ and 126 have larger binding energies than predicted by Equation (1.2). Note that the same structure is present at nuclei with $N = 2,\ 8,$ and 20 but it is difficult to see in this figure. If the same systematics of binding energies against the proton number is investigated, the same pattern is apparent. Additionally, nuclei with these special numbers of neutrons or protons have higher neutron or proton separation energies than the $N+1$ or $Z+1$ nucleus, and the first excited state is also located at very high excitation energy. These particular numbers have been called "magic numbers" and the emergence of these numbers has been one of the major subjects of nuclear physics research [6].

In the 1930's constructing the microscopic picture to predict magic numbers was attempted in the framework of the shell model. The simplest model is the independent

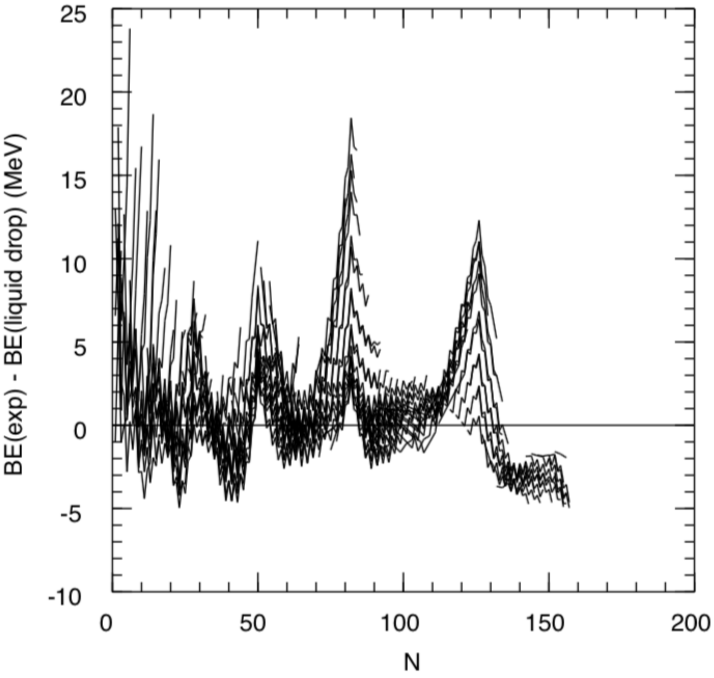

Figure 1.2: The difference of the binding energy between experiment and the semi-empirical mass formula as a function of the neutron number of the nucleus. Taken from [5].

particle model. In this model, the strong nuclear force is treated as a mean field potential generated by all nucleons and each nucleon is assumed to move independently in this potential. In the simplest case, the shape of the potential is assumed to be a harmonic oscillator. It is also known that the nuclear force is of short range, which leads to the reasonable assumption that the mean field potential can be similar shape as the density of nucleus. Alternative to the harmonic oscillator is thus the parameterizations as a Woods-Saxon potential,

$$V(r) = -V_0 f_{WS}(r), \tag{1.3}$$

$$f_{WS} = \frac{1}{1+e^{(r-R_0)/a_0}}. \tag{1.4}$$

Typically, the potential depth is $V_0 = 50$ MeV, the nuclear radius is $R_0 = 1.25A^{1/3}$, and the diffuseness is $a_0 = 0.7$ fm [7]. By solving the Schrödinger equation for this potential, each nucleon is filling a single-particle eigenstate, or orbital, characterized by its discrete energy and quantum numbers n, l, and j, where n is the number of nodes in the radial part of the wave function of the single nucleon, and l and j denote the orbital and total angular momentum of the state. The results of calculations with the harmonic oscillator or the Woods-Saxon potential are shown in the left and the central panel of Figure 1.3. Note that this simple model can reproduce the magic numbers up to 20, but it fails for the larger ones.

It was first proposed independently in 1949 by Mayer [8, 9], and Haxel, Jensen, and Suess [10] that the addition of a strong, attractive, one-body spin-orbit potential could explain the correct order of orbitals and thus the magic numbers,

$$V_{LS} = (l \cdot s) V_{LS} \frac{d}{dr} f_{WS}(r). \tag{1.5}$$

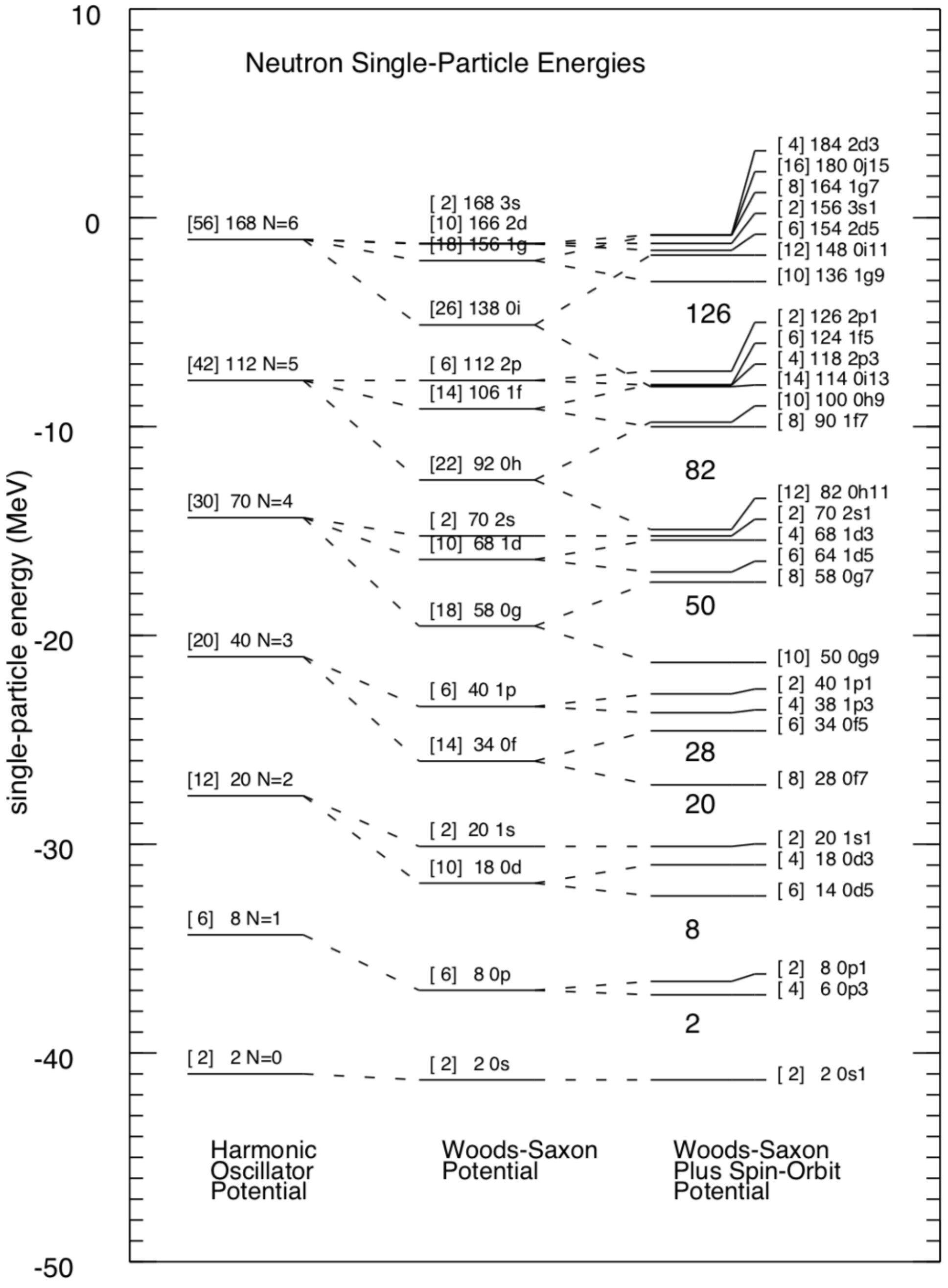

Figure 1.3: Example of the calculation of single-particle orbits. These calculations are for neutron single-particle states in ^{208}Pb with three different potentials. Taken from [5].

This spin-orbit force can be cancelled out from the other nucleons from all directions completely inside the nucleus, but such kind of cancelation can not exist at the surface of the nucleus. This is why the potential in Equation (1.5) is surface-peaked. Typically V_{LS} is chosen about 20 MeV. The result of a calculation of single-particle orbits with this spin-orbit term is shown in the rightmost of the Figure 1.3, reproducing all magic numbers, even beyond 28.

Though the spin-orbit term in the mean field can solve the problem of magic numbers, it is worth noting that the reason for the large spin-orbit coupling remains an open question. Relativistic mean field theories can predict a strong spin-orbit splitting but these theories are phenomenological and the magnitude of the parameters of the potential is deduced by the fitting to the experimental data [11]. In the non-relativistic framework, spin-orbit term can emerge from various sources and there may be the cancellation of these sources, leading to the difficult situation to predict the exact amount of the spin-orbit coupling [12]. This means that investigating the evolution of the spin-orbit splitting in the different situation, like nuclei with different mass or N/Z ratio, can shed light to the source of this part of potential.

1.2 The erosion of the $N = 28$ magic number

Owing to the capability to produce exotic nuclei using accelerator facilities, the disappearance of conventional magic numbers and the emergence of new magic numbers have been reported [13]. In addition to the study of the nuclear structure, the microscopic origin of such kind of structural changes has been in the focus of the modern nuclear physics research on both the theoretical and experimental sides. In this section, the disappearance of the $N = 28$ magic number, the first magic number originating from the strong spin-orbit interaction, is described as the main subject of this thesis' work [14].

Often the first excited state in even-even nuclei is a 2^+ state while the ground state is always 0^+ state. As mentioned in the previous section, the excitation energy of the first excited state of the magic nucleus is higher than that of the mid-shell nucleus. Complementarily, the reduced $E2$ transition probability from the 2^+ state to the ground state, $B(E2; 2^+ \to 0^+)$, is a good indicator if the nucleus has a collective nature or not. This is because a collective state can be considered as a state in which many particles are excited coherently from the closed core. The $B(E2)$ value of such kind of state can be 10 or 100 times larger than that of a single-particle excitation. For a good shell closure, on the other hand, the first excited state is not a the collective state and the decay to the ground state thus exhibits a small $B(E2)$ value. Figure 1.4 shows the systematics of the $E(2^+)$ and $B(E2; 0^+ \to 2^+)$ values for $Z = 12$ to 20. In the Ca isotopic chain ($Z = 20$), it is clearly seen that $E(2^+)$ at $N = 20$ and 28 are very high compared to those between. The opposite trend can be seen in the $B(E2)$ for this isotopic chain. Here, ^{42}Ca and ^{44}Ca have a high $B(E2)$ value, which, in contrast, is quite small at ^{40}Ca and ^{48}Ca. These experimental results show the magicity at $N = 20$ and 28 in the Ca isotopes. When the systematic trend of these values along the isotonic chain is studied, the situation changes drastically. When $E(2^+)$ values of $N = 28$ isotones are compared with each other, it drops quite drastically in the ^{46}Ar, two protons less than the doubly-magic ^{48}Ca nucleus. The $B(E2)$ values along the $N = 28$ line show a gradual increase up to ^{44}S (note that the value for ^{42}Si has not been measured yet). All of these results suggest a break down of the $N = 28$ magic number.

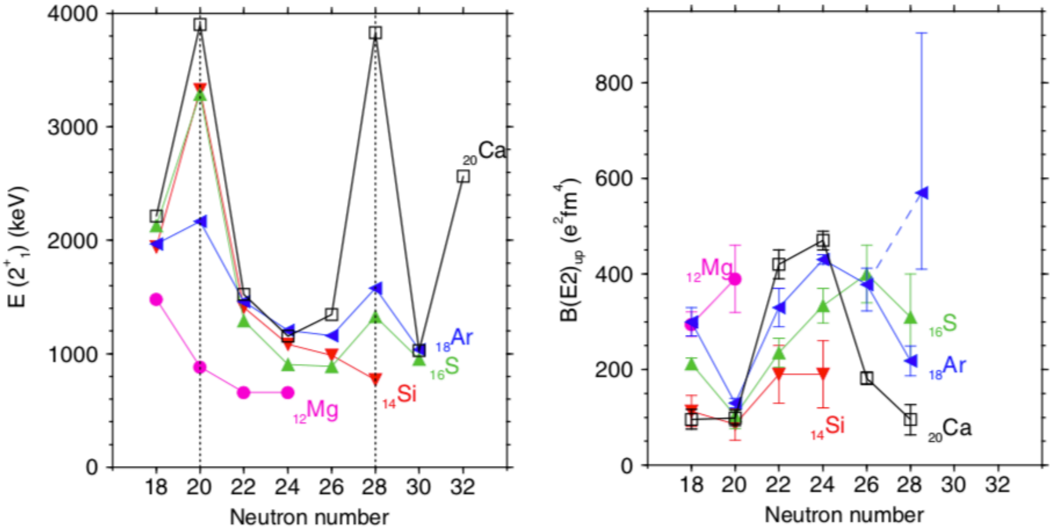

Figure 1.4: Experimental $E(2^+)$ (left) and $B(E2;0^+ \to 2^+)$ (right) in the $Z = 12$ to 20 isotopic chains against the neutron number N. Taken from [14].

The microscopic mechanism of such kind of shell quenching has been an intensive subject of both experimental and theoretical research. In the shell model framework, the tensor component in the nuclear force which is thought to have a crucial role in nuclei with asymmetric N/Z ratio, is considered as the source of the reduction of the gap between $f_{7/2}$ and $p_{3/2}$ orbits [15]. More details of the tensor force will be described in §2.1. Besides the shell quenching of neutron orbits, there can also be a reduction of the gap between the proton $d_{5/2}$ and $s_{1/2}$ orbits, which may be explained by the same theory of the tensor force. In addition to or triggered by this shell quenching, strong quadrupole correlations arise, which are induced by nucleons in orbits with an orbital angular momentum difference of two, $\Delta l = 2$ [15, 16]. This condition is fulfilled for both the proton and neutron orbits for nuclei around ^{44}S leading to the rich variety of the features relating to deformation, or shape coexistence for example [17, 18]. For instance, a rapid shape change of the ground state in the $N = 28$ isotones is predicted. Below ^{48}Ca, ^{44}S, ^{42}Si, and ^{40}Mg are thought to have the prolate, oblate, and again prolate ground state shapes [14]. From the point of view of both the nuclear structure itself and the mechanism of these structures, ^{44}S and nuclei around it need to be investigated.

Finally, experimental and theoretical results available in the literature on ^{44}S and ^{43}S, which are the main subjects of this thesis work, are compiled. The erosion of the $N = 28$ shell gap was first pointed out by a β-decay experiment [20]. Following Coulomb excitation [21] and mass measurement [22] experiments also support the collective nature of this nucleus [14]. In-beam γ-ray spectroscopic studies of ^{44}S [19, 23, 24] revealed the level structure beyond the 2^+_1 state of this nucleus. One of the experimental results of this nucleus [19] is shown in Figure 1.5. An interesting feature is the 4^+_1 state at 2459 keV [19, 25]. This state can be interpreted as the $K = 4^+$ isomer studied by the recent life time measurement [25] which can be in the lightest nucleus among those manifesting high-K isomerism [26]. Besides these works, the 0^+_2 state of this nucleus was found at 1365 keV with a 2.6 μs half-life [27, 28] and the monopole strength of the transition between the 0^+_2 and the ground state was measured [28] revealing the weak configuration mixing and the possible shape-coexistence. Compiling these studies, the coexistence of the three different neutron

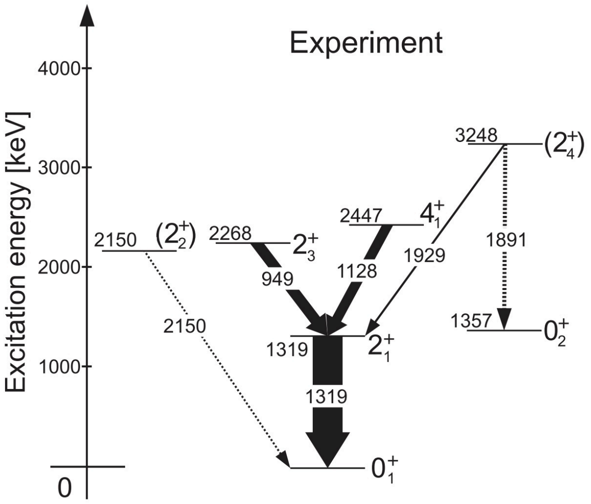

Figure 1.5: Level scheme of ^{44}S constructed by [19]. Through the comparison with the shell model calculation, the ground state band (the 0^+_1 and 2^+_1 states) is considered to be the $2p2h$ neutron intruder configuration with the prolate deformation, though the 0^+_2 state is the $0p0h$ normal configuration with the spherical shape. The 4^+_1 state is thought to be the $K = 4^+$ isomeric state of $1p1h$ configuration.

configurations, from 0 to 2 particle-hole excitation across the $N = 28$ shell gap, are experimentally suggested.

For ^{43}S, less experimental results are available so far. One of the reasons is the complex level structure of this nucleus due to the isomeric state at 320 keV with about 415 ns half-life[22, 29–31]. From a g-factor measurement of this isomeric state, the spin-parity of this state was determined as $7/2^-$ and that of the ground state was inferred to be $3/2^-$ considering the multipolarity of the electro-magnetic transition indirectly [29]. Through the measurement of the spectroscopic quadrupole moment of this isomer, this state was found to have rather large moment compared to the expected neutron single-hole configuration [31]. Also a Coulomb excitation [32] and a one-neutron knockout reaction [33] experiment were performed. Both of them suggested a collective nature of the deformed ground state but only a few excited states could be characterized due to the presence of the low-lying isomer. Recently, a life time measurement of low-lying excited states has been reported and possible three different band structure with different shapes is suggested [34].

Considering the proton configurations of these nuclei, experiments studying the one-proton knockout reaction from [35, 36] and to [37] ^{44}S have been performed. In these works, though the $Z = 14$ sub-shell closure was confirmed, the degeneracy of proton $d_{3/2}$ and $s_{1/2}$ orbits was suggested.

From the theoretical side, several works attempted to explain the structure of ^{44}S with different shapes or neutron configurations. One of the most intensive works are the calculations of mean field approach [38–42]. For instance, in a calculation considering the beyond-mean-field effect, configuration mixing rather than shape coexistence is thought to occur in ^{44}S [38, 39]. The collective wave function of each state calculated by [38] is shown in Figure 1.6. The ground state band (the 0^+_1 and the 2^+_1 states) of ^{44}S is predicted as a deformed but γ-soft state, which implies the mixing of different deformed states, and the second band (the 0^+_2 and the 2^+_2 states) is predicted as prolate deformed. This calculation successfully reproduces the level

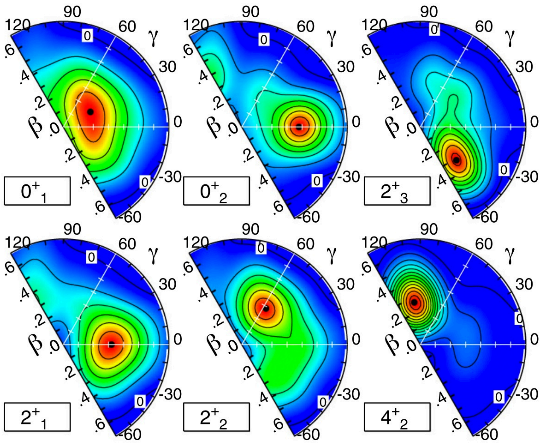

Figure 1.6: ^{44}S wave function of the symmetry conserving configuration mixing calculation plotted in the (β, γ) plane. Taken from [38]. See text for detail.

scheme of ^{44}S and the monopole strength of the transition between the 0^+ states. Though there are some limitations of the calculation methods and differences of the calculated results with each other, the deformation of each band structure and the influence of the configuration mixing are discussed in these works [40–42].

In the shell model framework, calculations with the SDPF-U and SDPF-MU effective interactions, which will be explained in §2.2.4, suggest a shell quenching at $N = 28$ due to the tensor force resulting in the large variety of deformed structures in ^{44}S and ^{43}S. Especially the ground state of ^{44}S is predicted as prolate deformed but its minimum in the potential energy surface is rather broad implying triaxial deformation [15]. Also the $K = 4^+$ band is reproduced in the calculation with SDPF-MU interaction [26]. In the calculations with SDPF-U interaction, the proton configuration is predicted to be a $2p2h$ excitation beyond the $Z = 14$ sub-shell and a near degeneracy of the $d_{3/2}$ and $s_{1/2}$ orbits is suggested in ^{44}S. For the neutron side, the $2p2h$ configuration is thought to dominate the wave function of the ground state, resulting in the possible triaxially deformed state [43]. For ^{43}S, this calculation predicts three band structures [43]. On the ground state which is considered as the axially prolate deformed state, a $K = 1/2^-$ rotational band is predicted. The isomeric state is not predicted spherical in shape, which is naively expected if this state is a single-hole state with a $(f_{7/2})^{-1}$ configuration, but instead a triaxially deformed state. As the third band, excited states with a neutron $2p2h$ configuration are predicted constituting a $K = 5/2^-$ rotational band with prolate deformation.

Also, calculations of ^{43}S with the antisymmetrized molecular dynamics (AMD) framework exist [16]. In this result, the ground state is a prolate deformed state in the $K = 1/2^-$ rotational band and the isomeric state is predicted as a triaxial state of $K = 7/2^-$ band. These features resemble the results of shell model calculations, but the AMD calculation suggests the third band ($K = 3/2^-$) with oblate shape, resulting in the coexistence of the three different shapes.

As discussed in the AMD work above and other mean field calculations, nucleon single particle orbits in the deformed nucleus are discussed. Especially a few works of the Nilsson models are present to discuss the shape of ^{43}S and the level scheme of this nucleus as shown in Figure 1.8 [44, 45]. As mentioned in the caption, Figure 1.8 is the calculation for ^{45}S but it can be reasonably assumed that the deformation and the evolution of neutron single particle orbits of these nuclei resemble with each other.

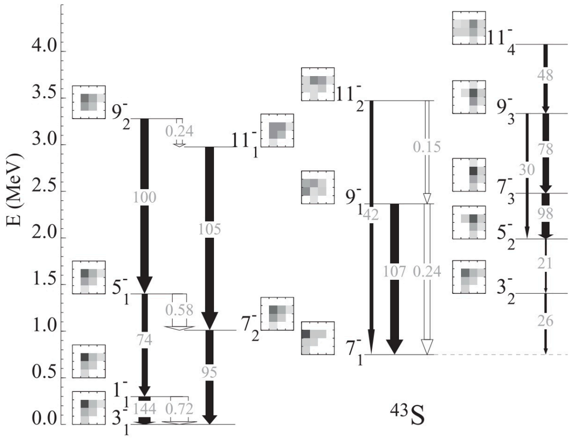

Figure 1.7: ^{43}S level scheme of the shell model calculation with the SDPF-U interaction. Taken from [43]. Filled (empty) arrows are the $E2$ ($M1$) transition probabilities in e^2fm^4 (μ_N^2). Two-dimensional graphics filled with gray boxes are the wave function components, where neutron (proton) $0p0h$ is the left (bottom) of X (Y) axis.

Note that the g-factor measurement work estimate the momentum of inertia of the deformed band of ^{43}S and the decoupling parameter by combining its experimental result and calculations of mean field approach, shell model, and particle rotor model [29].

Besides the nuclear structure of these sulfur isotopes, there are some attempts to explain the mechanism of the deformation of them microscopically. As mentioned above, the tensor force has a crucial role [15, 26] but it is pointed out by another work that central term also has the important contribution to the shell evolution of $N = 28$ gap [46]. Other than the shell model approach, the Hartree-Fock calculation assuming the axial deformation reveals that the tensor force is the possible source of the deformation in neutron-rich $N = 28$ isotopes [47]. Some other works of both relativistic and non-relativistic Hartree-Fock calculations, however, suggest that the tensor force has only a minor influence on Z or $N = 28$ gap [48–50].

1.3 Thesis objective and outline

As compiled in the previous section, a rich variety of structural studies related to the deformation of ^{44}S and ^{43}S has been reported both experimentally and theoretically. In contrast, the mechanism of such kind of structure in these nuclei remains unclear. Especially quantities related to the deformation have only been observed for few low-lying states of ^{43}S.

To tackle this problem, an in-beam γ-ray spectroscopy experiment utilizing the one-neutron knockout reaction from ^{44}S to ^{43}S was performed in this thesis work. As mentioned above, the evolution of the proton orbits has already been measured by proton knockout experiments [36]. The information about the neutron single-particle orbits or neutron configuration of the wave function, on the other hand, have not yet been obtained. By using the one-neutron knockout reaction, neutron single-hole states can be selectively populated. Energies and production cross sections of these states are related to the evolution of the neutron single-particle orbits and the neutron configuration of the ground state of ^{44}S, respectively. Note that the usefulness of this reaction channel to achieve the information on the neutron part of the wave function

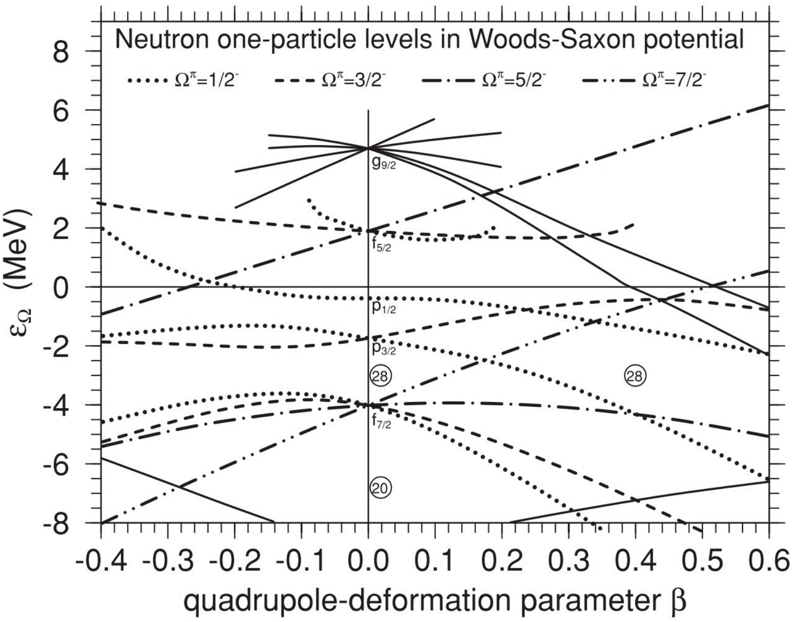

Figure 1.8: Nilsson orbits of the neutrons in ^{45}S. The energy of each neutron single particle orbit is plotted against the deformation parameter β. Taken from [45].

will be described in the next chapter in detail. Thus, the quenching of the $N = 28$ shell gap can be directly observed in the neutron-rich sulfur isotopes. Additionally, derivation of the neutron configuration can trigger the discussion about the importance of the neutron configurations for the deformation or shape coexistence in these nuclei. Through the comparison with theoretical predictions, further discussion about the development of the deformation in this region and the reduction of $N = 28$ shell gap will be made. Prior to obtain the excitation energy and production cross section of each state in this reaction channel, however, the full level scheme of ^{43}S needs to be constructed. This task is the main subject of this thesis work leading to a discussion on the band structure and deformation of excited or ground states. As mentioned in the previous section, an experiment with exactly the same reaction has already been performed, but the level scheme of ^{43}S remained unknown, especially in the higher excitation energy as shown in Figure 1.9, because of the presence of the isomeric state. Thus it was impossible to assign γ-rays to decays to the ground or the isomeric state. This problem was solve in this work, and the full level scheme of ^{43}S was constructed in this work.

In the following chapters, first the theories of nuclear structure and reaction related to this work will be shown. The general theory of Hartree-Fock and shell model calculations will be described in §2. The former was utilized as input to the reaction calculation and later was performed for the discussion of the structure of ^{43}S. In the following section, the general feature and formalism of one-nucleon knockout reaction theory will be described. How useful this reaction is to probe the microscopic information of the wave function will be first introduced and the reaction model used in this work will be detailed accompany with the calculation procedure.

In §3, the experimental setup of the present experiment will be described. First, it is shown how to produce, collect, and separate the exotic nuclei of interest. The structure of the reaction residue was deduced by measuring the energies and yields of the de-excitation γ-rays. So the setup of the γ-ray detectors follows. In the setup

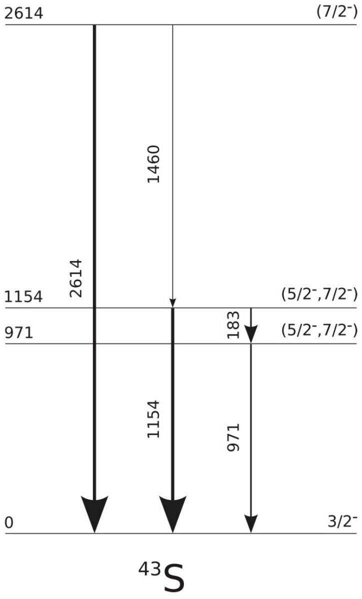

Figure 1.9: ^{43}S level scheme deduced by the previous one-neutron knockout experiment. As shown here, most of the prompt γ-rays were not placed. Especially, the level scheme on the isomeric state at 320 keV have been completely unknown so far. Taken from [33].

of the present experiment, the assignment of the spin-parity of the final state can be achieved by the analysis of the parallel momentum distribution of the reaction residue. How to derive this quantity will be also described in chapter 3.

The analysis performed in the present work will be detailed in the following two chapters. In §4, the analysis related to the calibration of detectors will be described. In §5, further treatment and derivation of the physics observables will be shown. The discussion about the results of this experiment deduced from these analysis will be performed in §6 and compared with the level scheme and spectroscopic factors deduced by the shell model calculation. Finally, the summary of this thesis work and the future outlook will be given in §7.

Chapter 2

Theoretical background

In this chapter, the theoretical description of nuclear structure and reactions will be briefly introduced. Not only the description of the nuclear force, which may explain the change of the magic numbers in the exotic nuclei, but also the theoretical approach used in the analysis and interpretation of the result of the present work will be given.

2.1 Nuclear forces

Protons and neutrons consist of up and down quarks. The strong force between quarks and gluons is described by quantum chromodynamics (QCD). Thus the force between nucleons should also be deduced in the QCD framework as the remnant of the interaction among the bound triplet of quarks. In quantum electrodynamics (QED), the other theory in the standard model, the coupling of the interaction $\alpha \approx 1/137$ is small and only weakly depends on the momentum making a perturbative expansion possible [51–53]. The strong coupling α_s, on the other hand, increases if the momentum decreases and becomes greater than 1 near the QCD momentum scale $\Lambda_{QCD} \approx 250$ MeV/c [53]. Considering the energy region of nuclear physics is small enough, for example the Fermi energy in a nucleus is around 30 MeV, QCD cannot be treated in perturbation theory. In this situation, effective theories of the nuclear force should be used for the quantitative prediction.

Though quarks have color charges and interact with other quarks by exchanging gluons, a nucleon is color-neutral and the interaction between nucleons is rather long distance. This situation resembles the interaction of neutral atoms. A long distances, more than 2 fm, the nuclear force is attractive but only small amount dying exponentially. In this region, the nuclear force can be modeled as the exchange of a pion. At medium range, like from 0.5 to 2 fm, other heavier mesons as the ρ and ω can contribute as the potential propotional to e^{-mr}/r resulting in the strongly attractive nature. Like the van der Waals force for atoms, the interaction in this region is thought to come from the fluctuations in color-charge density. In the short range region less than 0.5 fm, there is a strong repulsion due to the Pauli exclusion principle. Besides these two-body nucleon-nucleon interaction, three-body or higher-body parts of the potential can also have a significant effect on the nuclear structure.

The nuclear force in the long range mentioned above can be the main part because the average nucleon-nucleon distance in a nucleus is more than 2 fm. The nuclear force between two nucleons in this distance can be modeled as the exchange of a pion, which is the psuedoscaler ($J^\pi = 0^-$) isovector ($T = 1$) meson [54]:

$$V_\pi(r) = \frac{f_\pi^2}{4\pi m_\pi}(\tau_1 \cdot \tau_2)(\sigma_1 \cdot \nabla_1)(\sigma_2 \cdot \nabla_2)\frac{e^{-m_\pi r}}{r}. \tag{2.1}$$

Here, 1 and 2 are the labels of two nucleons, $r = |\vec{r}_1 - \vec{r}_2|$, σ and τ are the spin and isospin Pauli matrices, ∇ is the spatial derivative, $m_\pi \approx 140$ MeV is the pion mass, and the f_π is the coupling parameter of pion. This potential can be decomposed into scaler and tensor parts:

$$V_\pi = \frac{f_\pi^2}{12\pi}(\tau_1 \cdot \tau_2)\left[(\sigma_1 \cdot \sigma_2)\left(\frac{e^{-m_\pi r}}{r} - \frac{4\pi}{3}\delta^3(r)\right) + \mathbf{S}_{12}\left(\frac{1}{r} + \frac{3}{m_\pi r} + \frac{3}{(m_\pi r)^2}\right)\frac{e^{-m_\pi r}}{r}\right]. \tag{2.2}$$

Here, the tensor operator $\mathbf{S}_{12}$ is defined as

$$\mathbf{S}_{12} \equiv (\vec{\sigma}_1 \cdot \hat{r})(\vec{\sigma}_2 \cdot \hat{r}) - \frac{1}{3}\vec{\sigma}_1 \cdot \vec{\sigma}_2 \tag{2.3}$$

$$= \sqrt{\frac{8\pi}{15}}[\sigma_1, \sigma_2]^{(2)} \cdot Y^{(2)}, \tag{2.4}$$

where σ_1 and σ_2 are coupled to form a rank-2 tensor, $Y^{(2)}$ is the rank-2 spherical harmonic for the relative coordinate of two nucleons, and the dot means scaler product. As shown above, the one-pion exchange potential has a central term that depends on the distance r between two nucleons and a tensor term that depends both on a combinations of the relative positions and the orientation of the spins.

One of the interesting points is the effect of the tensor force on the nuclear structure [55]. For simplicity, only the monopole component (i.e. angle-averaged) of the tensor force will be discussed here. Suppose two nucleons in orbits a and b with quantum numbers (n_a, l_a, j_a) and (n_b, l_b, j_b), respectively, this component can be written as

$$\bar{V}_{ab}^T = \frac{\sum_J (2J+1)\,\langle j_a j_b \,|\, V \,|\, j_a j_b\rangle_{J,T}}{\sum_J (2J+1)}. \tag{2.5}$$

By averaging over all J couplings of the total angular momentum of the two nucleons, this expresses the average effect between nucleons in the orbits a and b. The total angular momentum of an orbit with given l are $j_< = l - \frac{1}{2}$ or $j_> = l + \frac{1}{2}$. One of the important feature of the tensor monopole term is that $\bar{V}_{j_<,j'_>}$ and $\bar{V}_{j_>,j'_<}$ are attractive, while $\bar{V}_{j_<,j'_<}$ and $\bar{V}_{j_>,j'_>}$ are repulsive.

This feature of the tensor force has been thought to play an important role for the nuclear structure of the exotic nuclei away from the stability line. In region of interest for this work, the splitting between the proton (π) $d_{5/2}$ and $d_{3/2}$ from $N = 20$ to $N = 28$ can be an example of shell evolution (see Figure 2.1). In this situation, the naive neutron (ν) configuration has 20 neutrons fill orbits up to the neutron $d_{3/2}$ orbit and the remaining ones occupy the $f_{7/2}$ orbit. As mentioned above, the monopole part of the tensor component is attractive for $\pi d_{5/2} - \nu f_{7/2}$ ($j_> j_>$), while it is repulsive for $\pi d_{3/2} - \nu f_{7/2}$ ($j_< j_>$). Moving from $N = 20$ to 28, neutrons are filling the $\nu f_{7/2}$ orbit and the gap between the proton orbitals $\pi d_{5/2}$ and $\pi d_{3/2}$ shrinks. Going down from ^{48}Ca, a doubly magic nucleus with $Z = 20$ and $N = 28$, along the $N = 28$ isotone line, removing protons from the $d_{3/2}$ orbit raises the $\nu f_{7/2}$ orbit by reducing the attractive interaction. The same situation can occurs for the $\pi d_{3/2} - \nu p_{3/2}$ orbits, above the $N = 28$ shell gap. Because the $1p_{3/2}$ orbit has a node in the radial wave function, reducing the radial overlap of the $\pi d_{3/2}$ and $\nu p_{3/2}$ orbits, the increase in energy of the $\nu p_{3/2}$ orbit can be smaller than that of the $\nu f_{7/2}$ orbit. This is a possible explanation for the breakdown of $N = 28$ shell gap.

One of the features of the tensor monopole component worth noting is the sum rule of

$$(2j_< + 1)\bar{V}_{j_<,j'}^T + (2j_> + 1)\bar{V}_{j_>,j'}^T = 0, \tag{2.6}$$

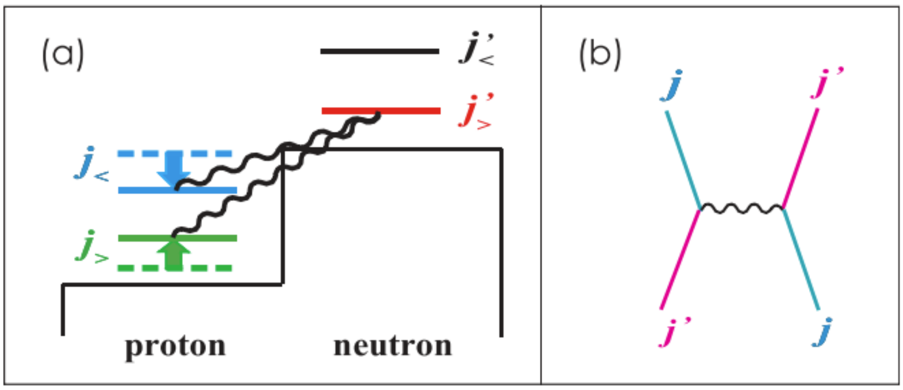

Figure 2.1: Schematic picture of the monopole interaction of the tensor force. (a) shows the interaction between a proton in $j_{>,<} = l \pm \frac{1}{2}$ and a neutron in $j'_{>} = l' + \frac{1}{2}$. It shows the situation where the energy of $j_{>}$ orbit increases and that of $j_{<}$ decreases because of the occupation of neutrons in $j'_{>}$ orbit. (b) shows the exchange process contributing to the monopole interaction. Taken from [55].

where the total isospin of the interacting nucleon pair can be either $T = 0$ or $T = 1$ and $j' = j'_{<}$ or $j' = j'_{>}$ are possible. This is derived analytically by angular momentum algebra. In a nucleus, this equation implies that the effect of the tensor monopole force is cancelled out if both $j_{<}$ and $j_{>}$ orbits are fully occupied. On the other hand, this means that the shell evolution originating from the tensor force is maximized if the $j_{>}$ orbit is fully occupied and the $j_{<}$ orbit is completely empty. As a result, the tensor force plays an important role for the shell structure of ^{44}S, the main nucleus of interest in this work, or ^{42}Si, compared to ^{48}Ca, because naively the $\nu f_{7/2}$ and $\pi d_{5/2}$ orbits are fully occupied but the $\nu f_{5/2}$ and $\pi d_{3/2}$ orbits are approximately empty.

2.2 Treatment of nuclear many-body system

Here, a few methods to solve the quantum many-body system are just briefly introduced. This section discusses how to calculate the eigenvalues of the Hamiltonian and expectation values of operators based on the effective interaction introduced in the last section.

2.2.1 Description of many-body states

Suppose the one-body wave function $\phi_i(\vec{r}_i)$ obeys the Fermi-Dirac statistics, an A-body fermionic wave function $\Phi(\vec{r}_1, \vec{r}_2, \ldots, \vec{r}_A)$ can be constructed by products of $\phi_i(\vec{r}_i)$. Requiring that this A-body wave function is anti-symmetrized against the exchange of any two particles, the Slater determinant of A particles is written as

$$\Phi(\vec{r}_1, \vec{r}_2, \ldots, \vec{r}_A) = \frac{1}{\sqrt{A!}} \det \begin{bmatrix} \phi_1(\vec{r}_1) & \phi_2(\vec{r}_1) & \ldots & \phi_A(\vec{r}_1) \\ \phi_1(\vec{r}_2) & \phi_2(\vec{r}_2) & \ldots & \phi_A(\vec{r}_2) \\ \vdots & \vdots & \ddots & \vdots \\ \phi_1(\vec{r}_A) & \phi_2(\vec{r}_A) & \ldots & \phi_A(\vec{r}_A) \end{bmatrix}. \tag{2.7}$$

In the framework of the second quantization, the same state can be represented as a Fock state by applying the creation operators $a_i^\dagger$ to the vacuum:

$$\left|\Phi^A\right\rangle = \frac{1}{\sqrt{A!}} a_A^\dagger \dots a_2^\dagger a_1^\dagger \left|0\right\rangle . \tag{2.8}$$

In this formalism, the antisymmetrization is treated through the anticommunication of the creation and annihilation operators:

$$\left\{a_i, a_j^\dagger\right\} = \delta_{ij}, \quad \left\{a_i, a_j\right\} = 0 = \left\{a_i^\dagger, a_j^\dagger\right\} . \tag{2.9}$$

The actual eigenstate of the Hamiltonian can be constructed by a linear combination of A-body Slater determinants.

2.2.2 Hartree-Fock calculation

The lowest-energy single Slater determinant can be found by the variational method, the Hartree-Fock or self-consistent mean-field method [56]. In this framework, each nucleon is treated as moving independently in a mean field potential generated by all the other nucleons. This means the conflicting situation that the wave function, which is the answer of this many-body problem, should be known in order to calculate the potential, resulting in the iterative method as below. For the start of the calculation procedure, the ground state is constructed by a reasonable set of the single-particle orbits occupied by nucleons obeying the Pauli principle. The mean field potential is generated from these orbits and the one-body Schrödinger equation is solved for each nucleon. From these new orbitals, a new mean field potential is calculated leading to an iterative procedure to find self-consistent wave functions of single-particle orbits.

Phenomenological interactions are often used for the Hartree-Fock calculation. In the present work, the Skyrme interaction is used. This interaction consists of the two-body interaction terms and the density dependent terms. Because the Skyrme interaction is phenomenological, its interaction terms are fit to the experimental data and there are many kinds of parameter sets. In this work, the SkX interaction is used [57]. Skyrme-Hartree-Fock calculations can well reproduce nuclear properties like binding energies and root-mean-square radii for closed-shell nuclei in which there is a large gap above the Fermi surface. Note that these kinds of calculations neglect the many-body correlations beyond the mean field and cannot reproduce the detailed nuclear structure well. In addition, because this framework is a variational method for searching the lowest energy state, Hartree-Fock calculations are not suited or justified to calculate excited states of nuclei. In the present work, Skyrme-Hartree-Fock calculations are performed for the calculation of the optical potentials and form factors for the knockout reaction.

2.2.3 Shell model calculation (configuration interaction)

Another approach to solve the ground or excited states of a nuclear system is to express the interaction is the form of a matrix in some chosen basis (usually constructed from Slater determinants)

$$H_{ij} = \left\langle \Phi_i \middle| \hat{K} + \hat{V} \middle| \Phi_j \right\rangle \tag{2.10}$$

and diagonalize it to obtain the eigenvalues. Here, $\hat{K}$ and $\hat{V}$ denote the kinetic energy and the interaction between the nucleons, respectively. The resulting eigenstates are then constructed by linear combinations of Slater determinants,

$$|\Psi_i\rangle = \sum_j c_{ij} |\Phi_j\rangle . \tag{2.11}$$

Ideally, an infinite dimensional basis and a realistic interaction should be used. In general, however, the interaction is limited to two-body terms and the basis is truncated to make the calculation feasible.

For the basis of the calculation, the eigenstates of the three-dimensional harmonic oscillator potential are a common typical choice. In this basis, the eigenstates are labeled by the radial quantum number n, the orbital angular momentum l, the total angular momentum $j = l \pm \frac{1}{2}$, and its projection m_j. Their energy eigenvalues are written as $\left(N + \frac{3}{2}\right) \hbar\omega$, where $N = 2n + l$ and ω is the oscillator frequency of the harmonic potential [58]. Then the difference of the nuclear interaction $\hat{V}_N$ from the harmonic oscillator potential $\hat{V}_{HO}$ is treated by perturbation theory,

$$\hat{H} = \hat{H}_{HO} + \hat{V}_N - \hat{V}_{HO} \equiv \hat{H}_{HO} + \hat{V}. \tag{2.12}$$

The eigenstates of the harmonic oscillator Hamiltonian constitute the oscillator basis and the corresponding eigenvalues can be described as $\langle j|\hat{H}_{HO}|i\rangle = N_i \hbar\omega\delta_{ij}$ by the diagonalized form. Here, the constant $\frac{3}{2}\hbar\omega$ is neglected. If the potential is written using only the two-body matrix elements (TBME), omitting the three-body or higher parts of the interaction, the perturbation potential is described as $\langle ab|\hat{V}|cd\rangle_{JT}$. Here, the total angular momentum J and isospin T of the two nucleons in orbits a and b are converted to those of c and d by the nuclear potential. In the ground state solved by the method described in the previous section, neutrons and protons occupy the energetically low orbits resulting in the lowest energy state as the ground state. In this configuration interacting (or mixing) shell model, on the other hand, the residual interaction, $\hat{V}$, mixes the wave function of multi-particle-multi-hole components describing the particle occupation in higher orbits as a result of the diagonalization.

To make the calculation feasible, orbits in higher energy (with high N) are truncated. Additional reduction of the active Hilbert space, or model space, is performed by the truncation of low N orbits. This means that a frozen, fully occupied, core is assumed and any particle excitation from this core is not considered. A doubly magic nucleus, like ^{16}O, is generally a good candidate for the core because the large shell gap in both proton and neutron orbits can be considered to highly suppress the particle excitation beyond the shell gap. The remaining orbits where the calculation is performed are called valence space. In this valence space, the zero-body term is calculated as the sum of the one-body and two-body matrix elements over the orbits in the core;

$$E_0 = \sum_{a\in\text{core}} \langle a|\hat{H}_{HO}|a\rangle + \frac{1}{2} \sum_{a,b\in\text{core}} \langle ab|\hat{V}|ab\rangle . \tag{2.13}$$

Like the constant term in the energy of the harmonic oscillator basis, this zero-body term can be omitted in the calculation because it is irrelevant for the calculation of the excitation spectra. Also an additional one-body term,

$$\delta\epsilon_a = \sum_{b\in\text{core}} \langle ab|\hat{V}|ab\rangle , \tag{2.14}$$

is used for the calculation of the single-particle energy (SPE) of state a as $\epsilon_a =$

$N_a\hbar\omega + \delta\epsilon_a$. Again, omitting higher-body terms, the interaction can be described by the TBME and the single-particle energies.

2.2.4 Effective interactions for shell model

Following the treatment described in the previous section, the remaining task is the description of the interaction. Ideally, the interaction should be derived from the interaction between free nucleons. Such an interaction can be taken from nucleon-nucleon scattering data, for instance. The result using this interaction, however, can only be accurate if the contribution from the out of the truncated model space is small.

In general, such kind of contribution cannot be neglected and additional procedures to make the calculation feasible are necessary. One of the possible methods is to abandon the direct connection between the potential and the underlying nucleon-nucleon interaction and to treat the TBME as free parameters of the effective interaction. In this approach, the TBMEs are constrained to reproduce the experimental data of the nuclei of interest. Also the SPEs are estimated from the experimental data, from the difference of the binding energies of the neighboring nuclei for example.

For the shell model calculations shown in this thesis work, this phenomenological method was used. Two kinds of the effective interaction, SDPF-U [59] and SDPF-MU [15] interactions were used. For the calculations with these calculations, an ^{16}O core is assumed and entire *sd*-*pf* shells are included in the interaction. The model space for the protons is restricted to the *sd* shell and that for the neutrons is in *pf* shell. Thus, these interactions consist of three parts: $\pi(sd)$-$\pi(sd)$, $\nu(pf)$-$\nu(pf)$, and $\pi(sd)$-$\nu(pf)$ components. The difference between the two interactions is that in the derivation of the SDPF-U interaction matrix elements are parametrized and fit to the experimental data, while the SDPF-MU interaction assumes the interaction consists of the central potential plus tensor component and all the matrix elements are calculated [60].

2.3 Theory of one-neutron knockout reaction

In the following part, the theoretical framework of the one-nucleon knockout reaction is described. Prior to the further discussion, it is useful to describe why the one-neutron knockout reaction was chosen in this experiment and how this reaction is suitable for the detailed investigation of the nuclear structure.

As mentioned in the previous chapter, the nuclear structure itself and the mechanism of the change of the structure is the main subject of this thesis work, like many other research activities on exotic nuclei [13]. For this purpose, not only the feature of the nucleus of interest, its level structure or the deformation of states, for instance, but also the microscopic information should be derived. Especially the proton and neutron configuration or the evolution of single-particle orbits around $N = 28$, $Z = 16$ is of interest of the present experiment. One of the advantages of the one-nucleon knockout reaction is its high selectivity to populate single-hole states, which are described as the core nucleus plus a hole of the knocked out nucleon in an orbit around it [7]. Though the wave function of a state can be a mixture of many terms, the component populated in the one-nucleon knockout reaction is the simple single-hole state. Thus, this reaction channel can probes the composition of the wave function of the nucleus of interest and determine the occupation numbers of the single-particle orbits.

Other aspects, not related to the theoretical advantage mentioned above, are the applicability of the method to radioactive beams [61, 62]. Now the structure of the unstable nucleus, which decays to another nucleus, is of interest. Since it is impossible to prepare the exotic nuclei as a target, the reaction has to be performed in inverse kinematics. Here the probe is the target nucleus and the nucleus of interest is the beam. In the present work, the beam of exotic nuclei was produced by fragmentation reactions at intermediate beam energy. This beam energy is suitable for one-nucleon knockout reactions and additional deceleration or acceleration of the beam is not necessary. Also, a thick target can be used at this beam energy maximizing the luminosity of the setup and making it feasible to observe the reaction even with the beam of extremely weak intensity.

2.3.1 Factorization of the cross section

If the transition operator of the nucleon knockout reaction is written as $\mathcal{O}_\alpha^{ko}$, the reaction amplitude for removing a nucleon with quantum numbers $\alpha = (n, l, s, j, m, t_z)$ from an initial state $\left|\Psi_i^A\right\rangle$ to a final state $\left|\Psi_i^{A-1}\right\rangle$ can be described as

$$\mathcal{A}_\alpha^{fi} = \left\langle \Psi_f^{A-1} \middle| \mathcal{O}_\alpha^{ko} \middle| \Psi_i^A \right\rangle . \tag{2.15}$$

Note that this operator also depends on the target nucleus and the beam energy. The definitions of the quantum numbers denoted as α are the principal quantum number, the orbital angular momentum, the spin, the total angular momentum, the projection of the total angular momentum, and the isospin of the nucleon or its orbit. The reaction cross section can be written as

$$\sigma_\alpha^{fi} = \left|\mathcal{A}_\alpha^{fi}\right|^2 . \tag{2.16}$$

If the time scale of the knockout reaction is fast enough, compared to the internal motion of the nucleus, the sudden approximation can be applied and the knockout operator can be assumed to be proportional to the annihilation operator a_α because the knocked out nucleon can be considered as frozen and the $A-1$ core can be also treated as the spectator during the reaction:

$$\mathcal{A}_\alpha^{fi} \Rightarrow \mathcal{C}_\alpha^{fi} \left\langle \Psi_f^{A-1} \middle| a_\alpha \middle| \Psi_i^A \right\rangle . \tag{2.17}$$

Here, $\mathcal{C}_\alpha^{fi}$ is a complex number. Though this is a very naive interpretation, one may consider the possibility to extract the occupation number $n(\alpha)$ of the single-particle or -hole state as

$$n(\alpha) = \left\langle \Psi^A \middle| a_\alpha^\dagger a_\alpha \middle| \Psi^A \right\rangle , \tag{2.18}$$

from this quantity. As mentioned above, the projection of the total spin m is one of the quantum number of the knocked out nucleon but in most experiments, like the present experiment, the polarizations of both the incoming and outgoing particles are not measured. This means that the cross section is the average of the projection of the incoming particle M_i and the sum of all the possible projections of the reaction residue M_f. The cross section of the one-nucleon knockout reaction can be described as [62]

$$\sigma_k^{fi} = \frac{1}{2J_i + 1} \sum_{M_i M_f} \left|\mathcal{C}_k^{fi}\right|^2 \left|\left\langle \Psi_f^{A-1} \middle| a_{k,m} \middle| \Psi_i^A \right\rangle\right|^2 , \tag{2.19}$$

where k represents all quantum number except for m. Note that m is constrained to $m = M_i - M_f$ by angular momentum conservation. Also the approximation that the average of $\mathcal{C}_k^{fi}$ over M_i and M_f is made. This is an assumption valid for a spherical projectile but exact if either of J_i or J_f are zero, which was achieved in the present experiment as $J_i = 0$. By the Wigner-Eckart theorem, the remaining sum results in

$$\begin{aligned} \sigma_k^{fi} &= \left|\mathcal{C}_k^{\overline{fi}}\right|^2 \frac{1}{2J_i+1} \left|\left\langle \Psi_f^{A-1} \middle\| a_k \middle\| \Psi_i^A \right\rangle\right|^2 \\ &= \sigma_k^{\mathrm{sp}} S_k^{fi} \quad \left(\text{where} \quad \left|\Psi_i^A\right\rangle = a_k^\dagger \left|\Psi_f^{A-1}\right\rangle\right). \end{aligned} \tag{2.20}$$

The term σ_k^{sp} is called the single-particle cross section and only depends on the reaction theory. The other term, S_k^{fi}, is the spectroscopic factor which can be calculated only from the structure of the initial and final states. This value is written as $C^2 S_k^{fi}(T)$, or for simplicity C^2S. Since structural calculations in the present work are mainly based on the shell model calculations, these results are affected by the unphysical center-of-mass motion of the shell model calculations and small center-of-mass correction should be applied for the spectroscopic factor calculated by the harmonic oscillator basis as [63]

$$C^2 S \rightarrow \left(\frac{A}{A-1}\right)^N C^2 S, \tag{2.21}$$

where $N = 2n + l$ is the previously mentioned quantum number of the oscillator shell.

From Equations (2.17), (2.19), and (2.20), the spectroscopic factor is related to the occupation number of a certain orbit, more strictly speaking, the overlap of the wave function of the initial state of the mass A nucleus and that of the final state described as a nucleon in a certain orbit coupled to the core of the mass $A-1$ nucleus. This means that a large spectroscopic factor characterizes the state as a single-hole state in this reaction. In general, the wave function can be a complex mixture of many components, resulting in a weak spectroscopic strength for the one-nucleon knockout reaction. From the value of the spectroscopic factor and the excitation energy of each state, the location of the single-particle strength can be quantitatively described by the weighted average of excitation energy. This value can be discussed as the effective energy of the single-particle orbit.

Through the calculation of the single-particle cross section, the comparison between experimentally measured one-neutron knockout cross section and the theoretically calculated one can be achieved. Experimentally, the spectroscopic factor for a one-nucleon knockout reaction is obtained from the measured cross section divided by the single-particle one. This analysis obviously depends strongly on the framework of the calculation of the single-particle cross section, which means the spectroscopic factor is not a direct observable of the experiment [64]. However, at least, the spectroscopic factor can be compared in a chosen analysis scheme. In the following part of this section, the framework of the reaction theory taken in this work will be described in detail.

2.3.2 The eikonal reaction theory

By applying the sudden approximation mentioned in §2.3.1 and assuming the core as a spectator, where the excitation and the internal reconfiguration of the core during the reaction are neglected, the single-particle cross section σ_k^{sp} is calculated by the Glauber (eikonal) reaction theory [65]. The wave function of the incoming nucleus is separated into the center-of-mass and relative parts as

$$\Psi_i^A(\vec{r}_1, \vec{r}_2, ..., \vec{r}_A) = \psi_{CM}(\vec{R}_{CM}) \otimes \psi_{\mathrm{rel}}(\vec{r}_1, \vec{r}_2, ..., \vec{r}_A). \tag{2.22}$$

The center-of-mass part can be modeled by a plane wave with the wave vector $\vec{k}$ in the free space,

$$\psi_{CM}(\vec{r}) = e^{i\vec{k}\cdot\vec{r}}. \tag{2.23}$$

This plane wave is distorted by the optical potential $U(r)$ in approaching the target. In this framework, the optical potential is assumed to be local and not to change in time, which means that the target recoil and breakup are omitted in the calculation. If the beam energy of the incoming particle is large enough, the change of the reduced Compton wavelength ($\lambda\!\!\!^{-} = k^{-1}$) against the radial coordinate can be assumed small, $\left|\frac{d\lambda\!\!\!^{-}}{dr}\right| \ll 1$, the WKB approximation [66] can be applied. Here, the wave number k can be treated as a slowly-varying function of the position

$$\begin{aligned} k(r) &= \sqrt{(E-U(r))^2 - m^2} \\ &\approx k_\infty - \frac{k_\infty U(r)}{2E_k} \qquad (\text{where } U(r) \ll E_k \ll m). \end{aligned} \tag{2.24}$$

In this equation, E is the total energy at infinity, $r \to \infty$, $E_k = E - m$ is the kinetic energy of the incoming particle, and $k_\infty = \sqrt{E^2 - m^2}$. The approximation of the second line is valid since for the present experimental conditions $U(r) \lesssim 50$ MeV, $E_k \sim 100$ MeV/u, and the mass of the nucleus $m \sim 1$ GeV/u. If the shape of the optical potential is approximated as the Woods-Saxon potential with parameters of the depth U_0 and the diffuseness a_0, the following conditions can be estimated:

$$\begin{aligned} \frac{dU}{dr} &\leq \frac{U_0}{4a_0} \\ \frac{d\lambda\!\!\!^{-}}{dr} &\lesssim \lambda\!\!\!^{-}_\infty \left(1 - \frac{U}{2E_k}\right)^{-2} \frac{1}{2E_k}\frac{U_0}{4a_0}. \end{aligned} \tag{2.25}$$

The typical values are $U_0 = 50$ MeV and $a_0 = 0.7$ fm, resulting in $k_\infty \sim 400$ MeV for the beam energy of the present experiment, which supports the application condition of the WKB approximation mentioned above. Assuming the potential as azimuthally symmetric and using the approximation of Equation (2.24), the center-of-mass wave function can be described as [65]

$$\psi_{CM}(R) = e^{ik_\infty z} e^{i\chi(b,z)}, \tag{2.26}$$

where the eikonal phase $\chi(b,z)$ is defined as

$$\chi(b,z) = -\frac{k_\infty}{2E_k}\int_{-\infty}^{z} U(b,z)dz. \tag{2.27}$$

From this, the elastic S-matrix in the eikonal limit can be deduced as

$$\mathcal{S}(b) = e^{i\chi(b,+\infty)}. \tag{2.28}$$

If the potential is real, $|\mathcal{S}(b)|^2 = 1$ and the far-field angular distribution for the elastic scattering can be achieved by integrating over all impact parameters. For a complex potential, $|\mathcal{S}(b)|^2$ can be smaller than 1 because of the loss of the flux to other reaction channels.

2.3.3 Optical potential

Here, the heuristic derivation of the optical potential, which reproduces a first-order approximation of a more rigorous consideration, will be described [67]. Suppose a projectile nucleon incident on a target nucleus whose density of nucleons, treated as the scattering centers, is described as ρ_t, then the probability of the scattering $P(z)$ can be derived. If the nucleon-nucleon scattering cross section is written as σ_{NN} and the impact parameter of the incident nucleon as $\vec{b} = (b, \phi)$, the probability $dP(z)$ of scattering within an infinitesimal path length between z and $z + dz$ is

$$dP(\vec{b}, z) = \left(1 - P(\vec{b}, z)\right) \sigma_{NN} \rho_t(\vec{b}, z) dz. \tag{2.29}$$

$1 - P(\vec{b}, z)$ denotes the probability of the nucleon surviving up to z. The condition of $P(z = -\infty) = 0$ provides the boundary condition resulting in

$$1 - P(\vec{b}, z) = \exp\left[-\sigma_{NN} \int_{-\infty}^{z} \rho_t(\vec{b}, z) dz\right]. \tag{2.30}$$

The quantity $1 - P(\vec{b}, z)$ mentioned above may be identified as the elastic S-matrix $\left|\mathcal{S}(\vec{b}, z)\right|^2$. Considering Equation(2.28), the imaginary part of the eikonal phase is

$$\text{Im}\{\chi(\vec{b})\} = \frac{1}{2}\sigma_{NN} \int_{-\infty}^{\infty} \rho_t(\vec{b}, z) dz. \tag{2.31}$$

Then, comparing the equation above and (2.27), the imaginary part of the nucleon-nucleus optical potential can be written as

$$\text{Im}\{U(\vec{b}, z)\} = \frac{-E_k \sigma_{NN}}{k_\infty} \rho_t(\vec{b}, z). \tag{2.32}$$

The derivation above is restricted to the situation where the projectile is a nucleon, but this can be reasonably extended to nucleus-nucleus scattering through the integration of the nucleon density in the projectile nucleus, ρ_p, resulting in the folded potential as

$$\text{Im}\{U(\vec{b}, z)\} = \frac{-E_k \sigma_{NN}}{k_\infty} \int d^3 r \rho_t(\vec{r}) \rho_p(\vec{r} - \vec{R}(\vec{b}, z)). \tag{2.33}$$

Here, $\vec{R}(\vec{b}, z)$ is the vector between the target and projectile centers. This derivation is often referred to as the $t\rho\rho$ approximation and identical to the first-order optical potential of multiple-scattering theory [68].

In the condition of the present experiment, it has been found that the real part of the optical potential has a relatively small effect on the resulting cross section. From this fact, the potential is parametrized as

$$U_{NN} = (i - \alpha)\text{Im}\{U_{NN}\}, \tag{2.34}$$

where $\alpha_{pn} = 1.0$ and $\alpha_{pp} = \alpha_{nn} = 1.87$ at 100 MeV [69]. These parameters are deduced by the fitting to the nucleon-nucleus reaction cross section data down to 100 MeV. To apply this analysis to slower beam, the additional parameter sets are used for the beam energy down to 30 MeV/u [70]. Additionally, the finite range of the nucleon-nucleon interaction is approximated by a Gaussian and the full optical potential can be described as

$$U_{NN}(b, z) = (i - \alpha)\frac{-ik_\infty \sigma_{NN}}{2E_\infty} \int d^3 r_t d^3 r_p \rho_t(\vec{r}_t) \rho_p(\vec{r}_p) \exp\left[-\frac{(\vec{r}_t - \vec{r}_p - \vec{R}(b, z))^2}{\gamma^2}\right], \tag{2.35}$$

where $\gamma_{np} = \gamma_{nn} = \gamma_{pp} = 0.5$ fm are taken from [71]. It can be reasonably assumed that these parameters corresponds to the form factor of each nucleon and are not influenced by the nuclear structure. Actually, these parameter sets can reproduce the reaction cross sections of ^{12}C-^{12}C and ^{27}Al-^{12}C systems at 83 MeV/u and proton-^{9}Be system at 60 MeV/u [72–74]. Also calculated one-nucleon knockout cross sections for nuclei around ^{12}C have good agreement with experimental values in wide energy range from around 250 to 2000 MeV/u [75]. Besides these validations, the deduced absolute spectroscopic factor of the isomeric state of ^{43}S in this work is quite consistent with the estimated one from the g-factor measurement. This discussion will be made in §6.2 justifying the whole treatment of the reaction calculation in the present work.

2.3.4 Densities and form factors

For the derivation of the nucleus-nucleus optical potential described in the previous section, the calculation of the target and core densities is necessary as can be seen in Equation (2.35). The core density is derived by the Skyrme-Hartree-Fock calculation described in 2.2.2. The target density is modeled as a Gaussian. Compared to the target density calculated by the Hartree-Fock or a quantum Monte Carlo calculation, the difference of the overall single-particle cross section results in the order of 1-2%.

The other remaining parameter is the core-valence two-body wave function, or form factor $\phi(r)$. In early work [76] it was found that the calculated cross section can be strongly affected by the root-mean-squared (rms) radius of the two-body wave function. In almost all the experiment with the exotic nuclei, however, the two-body wave function of the nucleus of interest is completely unknown. Thus taking consistent method to calculate the form factor of the unstable nuclei is important. In the present work, the so-called well-depth prescription proposed in [76] is chosen. The two-body wave function is deduced by solving the Schrödinger equation for a nucleon in a Woods-Saxon potential:

$$V(r) = -V_0 f_{WS}(r) + (l \cdot s) V_{LS} \frac{d}{dr} f_{WS}(r) \tag{2.36}$$

$$f_{WS} = \frac{1}{1 + e^{(r-r_0)/a_0}}. \tag{2.37}$$

The parameters V_0, V_{LS}, r_0, and a_0 need to be fixed. The diffuseness a_0 and the spin-orbit depth V_{LS} are found to have only small influence on the calculated cross section, so a_0 and V_{LS} are chosen to be 0.7 fm and 6 MeV [76]. The remaining parameters, the potential depth V_0 and the radius r_0, are adjusted to reproduce the binding energy and the rms radius of the single-particle orbit calculated by the Skyrme-Hartree-Fock calculation. The asymptotic form of the radial wave function must be an exponential decaying with a constant determined by the binding energy. In this step, r_0 is fixed by using the Skyrme-Hartree-Fock result, r_{HF}, as

$$r_0 = \sqrt{\frac{A}{A-1}} r_{HF} \tag{2.38}$$

For the calculation of the one-neucleon (here we concentrate on one-neutron case) knockout from the ground state of the incoming particle, the binding energy is written as $E_f - E_i = S_n + E_x$, where S_n is the neutron separation energy of the projectile and E_x is the excitation energy of the final state.

One of the remarks worth noting is that the optical potential of the fully occupied orbits, $\nu 0d_{3/2}$ or $\nu 1s_{1/2}$ for instance, are similar shape with the Woods-Saxon potential

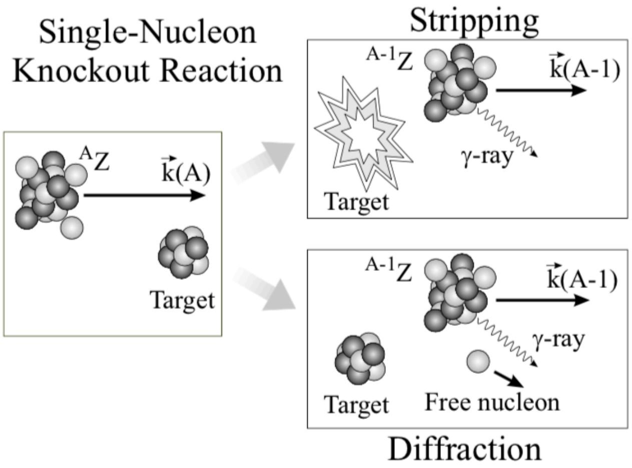

Figure 2.2: Schematics of the typical two mechanisms of the knockout reaction. In the stripping process, the knocked out nucleons are interacting with the target nucleus resulting the excitation of the target. In the diffraction process, the nucleons are elastically removed from the projectile. Taken from [80].

described as Equation (2.37). For the partially occupied $\nu 0f_{7/2}$ or weakly-occupied $\nu 1p_{3/2}$ orbits which is above the Fermi surface of the Hartree-Fock result, however, show the significantly greater depth of the potential. This can be attributed to the correlations beyond the mean field which can be thought to play an important role of binding the orbits near the Fermi surface. To reproduce the binding energy measured experimentally or calculated in the Hartree-Fock approach, an unrealistic mean field parameter V_0 is necessary. The treatment of the form factor for such kind of orbits has not been satisfactory solved [77–79].

Related to this problem, the single-particle cross sections for orbits above the Fermi surface can have a substantial uncertainty against the small change of the parameters like V_0 or r_0, or the resulting rms radius of the form factor. This is also a reason to choose a consistent analysis method for the calculation of the single particle cross section. Again, it is worth noting that the well-depth prescription is chosen for the present analysis to enable us to compare the present work with the other experimental results consistently.

2.3.5 Reaction mechanisms and cross sections

The cross section of the one-nucleon knockout is divided into two reaction mechanisms, stripping and diffraction [61], as can be seen in Figure 2.2. In the stripping mechanism, the valence nucleon is scattered by the target due to the imaginary part of the optical potential, written as $1 - |\mathcal{S}_v|^2$, while the core of the incoming particle survives, described as $|\mathcal{S}_c|^2$. This process results in the inelastic nucleon removal with the excitation of the target nucleus. The cross section of this reaction mechanism is then described as [81]

$$\sigma_{\mathrm{str}} = \frac{1}{2J+1} \sum_m \int d^2b \, \langle \phi_0^m | \, |\mathcal{S}_c|^2 \left(1 - |\mathcal{S}_v|^2\right) | \phi_0^m \rangle \, . \tag{2.39}$$

Here, J is the angular momentum of the incoming particle, b is the impact parameter between the projectile core and the target, ϕ_0^m is the core-valence form factor, described in the previous section.

The second part, the elastic nucleon removal, is made by two components. One is the diffraction process due to the imaginary part of the potential and the other is the refraction process due to the real part. These two process are added coherently and described as [81]

$$\sigma_{\text{diff}} = \frac{1}{2J+1} \sum_{mm'} \int d^2b \int d^3k \left| \left\langle \phi_{\vec{k}}^{m'} \middle| \mathcal{S}_c \mathcal{S}_v \middle| \phi_0^m \right\rangle \right|^2 . \tag{2.40}$$

In the following discussion, the sum of these two process will be called the diffraction mechanism for simplisity. The equation above describes the excitation of the core and the valence nucleon into a continuum state with relative momentum $\vec{k}$. Inserting the closure relation below

$$\sum_{m'} \int d^3k \left| \phi_{\vec{k}}^{m'} \right\rangle \left\langle \phi_{\vec{k}}^{m'} \right| = 1 - \sum_{m'i} \left| \phi_i^{m'} \right\rangle \left\langle \phi_i^{m'} \right| \tag{2.41}$$

in Equation (2.40),

$$\sigma_{\text{diff}} = \frac{1}{2J+1} \sum_{mm'} \int d^2b \left(\langle \phi_0^m \| \mathcal{S}_c \mathcal{S}_v |^2 | \phi_0^m \rangle - \sum_i \left| \left\langle \phi_i^{m'} \middle| \mathcal{S}_c \mathcal{S}_v \middle| \phi_0^m \right\rangle \right|^2 \right) \tag{2.42}$$

is derived. Note that i denotes the label of the bound states. The first term of Equation (2.42) corresponds the situation that both the core and the target survive and the second term is that both of them result in the bound final states. A further approximation can be made with the assumption that the ground state is the only bound state, $\left\langle \phi_i^{m'} \middle| \mathcal{S}_c \mathcal{S}_v \middle| \phi_0^m \right\rangle \approx 0$ for $i \neq 0$. This results in neglecting the sum of the second term and only the ground state is considered in Equation (2.40), which is often a good assumption [81].

The two reaction mechanism above can be distinguished by the resulting state of the target nucleus: in the stripping process the target nucleus is excited, though in the diffraction process it remains in the ground state. In the present experiment, ^{9}Be is used as the reaction target as described in §3.3. Because this nucleus does not have any other bound state than the ground state, these two process can possibly be separated by measuring the recoil in coincidence, which was not pursued in the present setup. However, this condition means that the total cross section of the single-nucleon knockout reaction can be described as the incoherent sum of two process without any interference [61],

$$\sigma_{\text{ko}} = \sigma_{\text{str}} + \sigma_{\text{diff}} . \tag{2.43}$$

Typically, the cross section of the stripping process dominates the total cross section. Note that there is also a contribution from the Coulomb breakup process but here it is neglected because a light target nucleus is chosen.

2.3.6 Momentum distributions

By the sudden approximation, the momentum of the struck out nucleon $\vec{k}_v$ can be written in terms of those of the incoming and outgoing particle, $\vec{k}_A$ and $\vec{k}_{A-1}$, as

$$\vec{k}_v = \frac{A-1}{A} \vec{k}_A - \vec{k}_{A-1} . \tag{2.44}$$

This means that by measuring the momentum of the reaction residue $\vec{k}_{A-1}$, the momentum of the valence nucleon can be extracted through the recoil of the knockout reaction. The probability for a particular momentum of the reaction residue $\vec{k}$ is given by the Fourier transformation of the position-space core-valence wave function to the momentum-space one. In the present setting, however, the hadronic nucleus is used as the target, which means the reaction probability is surface-peaked and is not equal anywhere in the nucleus. Thus the reaction probability in the nucleus should be weighted depends on the position in the nucleus. Generally, the transverse momentum, perpendicular to the beam axis, suffers from Coulomb effects and the parallel momentum can be treated easier experimentally. The parallel momentum distribution of the stripping process is described as

$$\frac{d\sigma_{\mathrm{str}}}{dk_z^c} = \frac{1}{2J+1}\sum_m \int d^2b_v \left(1-|\mathcal{S}_v|^2\right) \int d^2\rho |\mathcal{S}_c|^2 \left| \int dz \frac{e^{ik_z^c z}}{2\pi}\phi(\rho, z)\right|^2 , \tag{2.45}$$

where $\vec{b}_v$ is the impact parameter of the valence nucleon and $(\vec{\rho}, z)$ is the relative position vector between the core and the valence nucleon.

In the calculation the momentum distribution of the diffraction process is assumed to be identical to that of the stripping mechanism. The calculated momentum distributions are then compared with the experimentally observed ones and the orbital angular momentum l of the struck out nucleon is deduced. Figure 2.3 shows the theoretical parallel momentum distributions for neutron knockout from $l = 1$ to 3 orbits in ^{44}S calculated in the rest frame of ^{44}S. The shape, especially the width, of the distribution can be used to distinguish the orbital angular momentum value of knocked out neutron, which is the same manner to the comparison of the angular distributions in the transfer reaction.

2.3.7 Reduction factor

Though the one-nucleon knockout reaction has been established as a powerful tool of the spectroscopic study, there are some open questions related to the treatment or description of the reaction itself. One of those topics, which is of interest for the present study, is the so-called reduction factor R_S [76, 82]. This value is defined as the ratio of the observed cross section of the one-nucleon knockout to all the bound state below the particle threshold, and the theoretical one:

$$R_S = \frac{\sigma_{exp}}{\sigma_{th}}. \tag{2.46}$$

It should be noted that the calculation of σ_{th} involves typically the reaction model (such as the eikonal model) and the structure model (the shell model in this case) which are based on the different Hamiltonians. Thus, an unified theory to calculate the nuclear reaction and the shell structure using the same Hamiltonian would be desired as the future work. For the direct comparison with the experimental cross section, the theoretical cross section to populate a specific state by one-nutron knockout reaction is described as

$$\sigma(J^\pi) = \left(\frac{A}{A-1}\right)^N C^2S(J^\pi)\sigma_{sp}(J, S_n + E_x(J^\pi)). \tag{2.47}$$

Note that the first term in the right side of Equation 2.47 is the center-of-mass correction mentioned in Equation 2.21, the second term is the spectroscopic factor obtained

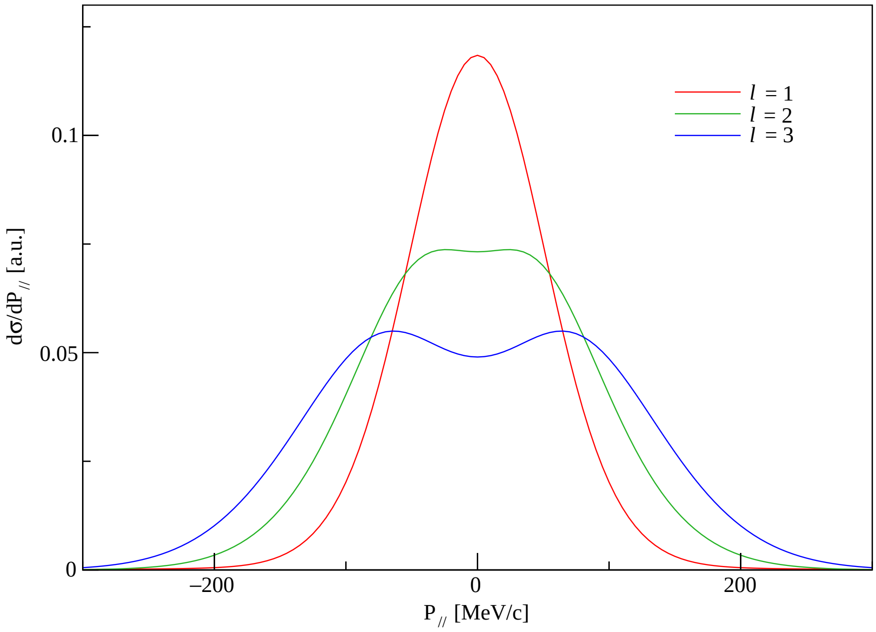

Figure 2.3: Parallel momentum distributions calculated in the rest frame of the ^{44}S. Equation 2.45 was used for the calculation. Red, blue and green lines show the momentum distribution of the neutron knockout from $l = 1$, 2, and 3 orbitals. The single-particle cross section is scaled to that of neutron knockout from $l = 1$ orbit.

by the structure calculation, the shell model in this work, and the third term is the single-particle cross section for the state with the excitation energy of E_x.

Historically, the reduction factor was studied through the one-nucleon transfer and quasi-free electron induced knockout reactions. It was found that the experimentally observed spectroscopic strength was smaller than the theoretical prediction, using the shell model calculation for instance, even for reactions from or to doubly-magic nuclei, where the single-particle or -hole structure was strongly expected [83]. For the proton transfer reaction, this discrepancy between the experimental and theoretical spectroscopic strength was confirmed by using a different reaction, the quasi-free proton knockout induced by electrons $(e, e'p)$. Over a large region of the nuclear chart, the reduction factor was found to be $R_S \approx 0.6 - 0.7$ [84]. Thanks to the improvement of the accelerator facilities, many experimental data of both stable and unstable nuclei are now available for both proton and neutron knockout with various binding energies. It has then been found that R_S has a characteristic trend shown in Figure 2.4 against the separation energy difference below [75, 76, 82]:

$$\Delta S = \begin{cases} S_n - S_p & \text{neutron knockout,} \\ S_p - S_n & \text{proton knockout.} \end{cases} \tag{2.48}$$

For the stable nuclei, $\Delta S \sim 0$, the deduced R_S is consistent with that of $(e, e'p)$ reactions and transfer reactions [85]. In the unstable region, this trend means that R_S goes up around 1 for knockout of loosely bound nucleon, such as neutron knockout from neutron-rich nucleus for example.

Though these reactions have been firmly established both experimentally and theoretically as a spectroscopic tool, the source of the reduction factor in these reactions

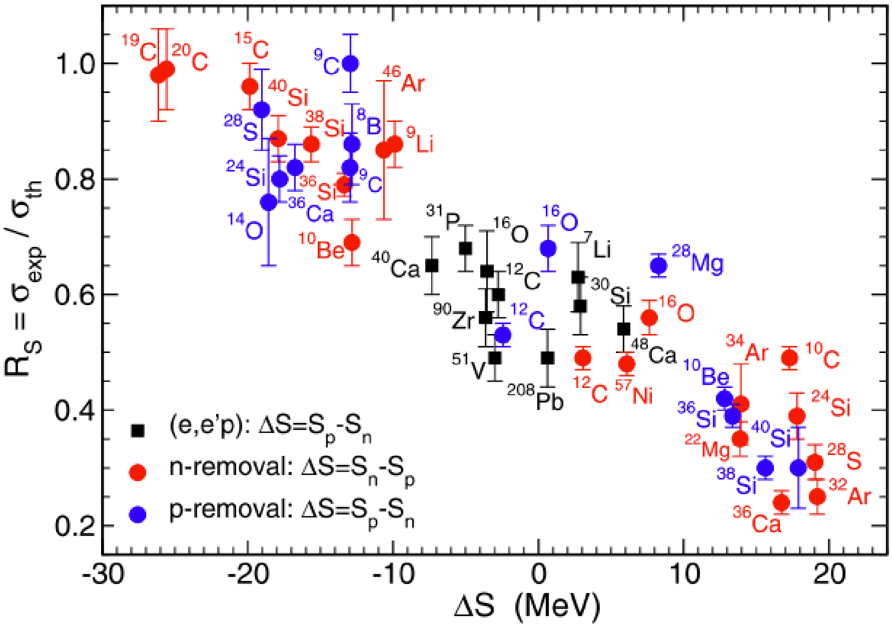

Figure 2.4: Compilation of the R_S against the difference of the proton and neutron separation energies. The red, blue, and black points correspond to the one-neutron, one-proton knockout reaction, and electron-induced proton knockout reaction data, respectively. Taken from [82].

are still treated as an open question. Note that the reduction of the spectroscopic strength has been found in completely different types of reactions, which implies R_S is not related to the treatment of a single reaction type. There are many works to approach this problem and the emergence of the reduction factor is now attributed as missing correlations in the nuclear structure theory, short-range correlations, for example. In the present study, the experimental setup was not designed to investigate the relationship between the observed cross section and the microscopic nuclear correlation, and the structure of a certain nucleus is the main subject. Thus the reduction factor R_S is treated as an empirical parameter as shown in Figure 2.4 like the many other studies on the nuclear structure using one-nucleon knockout reactions. For the consistency with previous studies, the reduction factor is taken to be $R_S = 0.83(4)$ [33], where $S_p = 2.12(6) \times 10^4$ keV and $S_n = 5080(7)$ keV for ^{44}S [86]. As mentioned in §2.3.3, the validation of the whole treatment to deduce the absolute spectroscopic factor will be confirmed in §6.2.

Chapter 3

Experimental setup

In this chapter, the experimental setup of this thesis' work is described. The present experiment was performed at the Coupled Cyclotron Facility [87] at the National Superconducting Cyclotron Laboratory at Michigan State University. A secondary beam of ^{44}S was produced by the fragmentation reaction of a ^{48}Ca primary beam by utilizing the cyclotron complex of K500 and K1200 [88] and separated by the A1900 fragment separator. The reaction of interest was taken place at the ^{9}Be reaction target at the pivot position of the S800 spectrometer [89]. The rigidity of the S800 was centered on the one-neutron knockout residue. In some runs, unreacted beam particles were centered for the calibration of some quantities. De-excitation γ-rays were observed by a combination of the GRETINA array [90] of high-purity germanium detectors, surrounding the reaction target, and the IsoTagger array of CsI(Na) detectors [91], placed at the very end of the S800. The entire detector setup, including the signal processing and the data taking system, will be detailed in the following sections.

Prior to the further information, the definition of some parameters is useful. The coordinates of particles x and y denote the dispersive and non-dispersive position, and a and b correspond the angle of the particle trajectory in dispersive and non-dispersive direction, respectively. The position along the beam line is defined as z.

3.1 Production of radioactive beam

^{44}S is unstable, it decays via β decay with a half life of 123(10) ms [20], which means it is necessary to produce this nuclei from other stable nuclei. Figure 3.1 shows the schematic of the accelerators and the following fragment separator to produce the radioactive isotope beam. The production of the radioactive beam of ^{44}S as the main

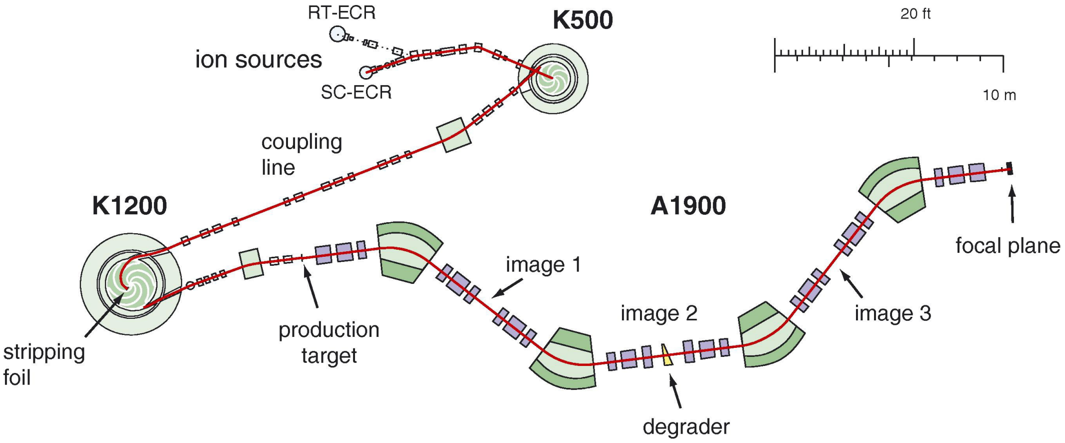

Figure 3.1: A schematic of the Coupled Cyclotron Facility and the A1900 fragment separator. Taken from [92].

component was achieved by the in-flight fragmentation reaction of a stable ^{48}Ca beam. First, metallic ^{48}Ca was heated in an oven to produce a vapor. The neutral atoms were then ionized by an electron cyclotron resonance (ECR). Here electrons were confined by the magnetic field and driven by the radio-frequency (RF) electric field. They collide with the neutral ^{48}Ca atoms and ionize them. Singly or doubly ionized were then injected in the first superconducting cyclotron, K500 [88].

A cyclotron confines a charged particle with a static and uniform magnetic field and accelerates it with an RF electric field whose frequency is adjusted to the cyclotron frequency, ω_c, of the charged particle:

$$\omega_c = \frac{qB}{\gamma m}, \qquad \rho = \frac{P}{qB}, \tag{3.1}$$

where q, m, and P denote the charge, mass, and momentum of the charged particle, γ is the relativistic factor $\gamma = 1/\sqrt{1-\beta^2}$, where β is the ratio of the velocity of the particle, v, to the light speed, $\beta = v/c$, B is the applied magnetic field, and ρ is the radius of the trajectory of the particle. From this equation, the radius of the particle trajectory becomes larger as the particle momentum is increased by the acceleration through the RF field. Finally, the particle reaches the outer edge of the K500 cyclotron with $\beta \sim 0.15$ and extracted by the electrostatic deflectors.

Charged particles were transported through the coupling line and injected into the second superconducting cyclotron K1200 [88] for further acceleration. According to Equation (3.1), to further accelerate particles, one needs to increase the size of the accelerator for larger radius of the particle trajectory, increase the strength of the magnetic field, and/or increase the charge of the particle. For this purpose, a carbon stripper foil was placed near the center of the K1200 and all the electrons of ^{48}Ca particles were fully stripped here. Then the primary ^{48}Ca^{20+} beam was accelerated up to approximately $\beta \sim 0.5$. In the present experiment, the primary beam intensity was about 12 pnA during the beam time.

3.2 The A1900 fragment separator

The primary beam with an energy of 140 MeV/u impinged onto a ^{9}Be production target with a thickness of 705 mg/cm^2. By the fragmentation reaction here, a cocktail of secondary beam particles with smaller masses and different N/Z ratios compared to the primary beam were produced. To collect the produced particles and separate out the isotope of interest from other reaction residues, the A1900 fragment separator [92, 93] is placed downstream of the production target, as shown in Figure 3.1.

The A1900 consists of 24 superconducting quadrupole magnets and four 45° superconducting dipoles with maximum magnetic rigidity, $B\rho$, of 6 Tm. This separator has the large momentum and angular acceptance of $\Delta P/P = 5\%$ and $\Delta\Omega = 8$ msr. The collection efficiency is almost 100% for the fragments $A \sim 50$ with 150 MeV/A. The A1900 has three intermediate image planes between the dipoles. Slits and a degrader for the separation of the isotopes were placed at these image points. The focal plane of the A1900 separator, downstream of the fourth dipole, is the injection point of the beam transport lines to the various experimental areas. As will be described in §3.3.2, here was the extended focal plane (XFP) where a plastic scintillator was located.

The particle separation was performed by the $B\rho - \Delta E - B\rho$ method. By the selection of magnetic rigidity in the first half of the A1900 up to the second intermediate image, which was achieved by the adjustment of the magnetic filed of the

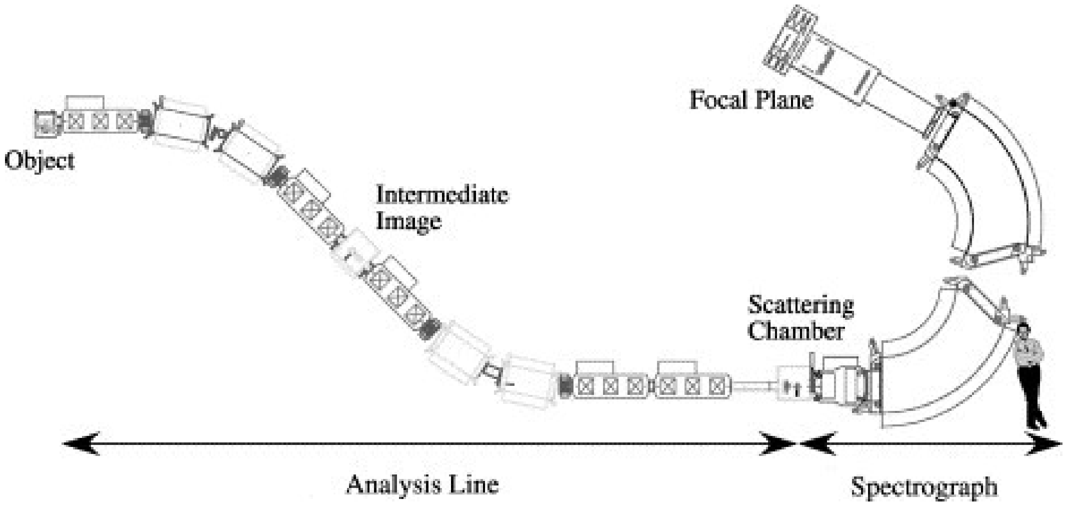

Figure 3.2: A schematic of the S800 spectrograph. Taken from [89].

first and second dipoles and the fixed radius of curvature of the beam line, P/q values of particles in the secondary beam was chosen from Equation (3.1). Because of the high beam energy, the velocity, or the energy and momentum per nucleon, are approximately conserved before and after the fragmentation reaction. Also assuming the fragmentation products are fully-stripped is valid in the case of for medium-mass nuclei with the high beam energy. Considering those above, selection on P/q equals to one on A/Z. This selection is achieved with slits on the intermediate images, dispersed in momentum by dipoles, restricting the range of radii of curvature ρ for the beam to pass.

This $B\rho$ filter allows all particles with the same A/Z to pass. For the further separation, the secondary beam passed through an Al wedge degrader placed on the second intermediate image. By the collision with the atomic electrons in this degrader, beam particles lose part of their energy (ΔE) according to the Bethe-Bloch formula [94]:

$$-\frac{dE}{dx} = \frac{4\pi e^4 n_e Z^2}{m_e \beta^2}\left[\log\left(\frac{2m_e\gamma^2\beta^2}{I}\right) - \beta^2\right], \tag{3.2}$$

where e is the electron charge, n_e is the electron density of the material, Z is the atomic number of the charged particle passing through, m_e is the electron mass, and I is the ionization potential of the material. Note that this degrader was wedge shaped [93] to conserve the momentum dispersive condition downstream. Assuming again the constant velocity β, the energy loss in the degrader depends only on Z of the beam particle and thus its remaining momentum depends on Z. By another $B\rho$ selection with slits, the desired range of Z can be selected, and in total restricted range of A and Z can be chosen. For this separation method, the thickness of the wedge degrader and the acceptance of momentum $\Delta P/P$ should be properly chosen. In the present experiment, an Al degrader with the thickness of 450 mg/cm^2 was used and the momentum window was restricted to 1%, which was also related to the resolution of the momentum measurement after the secondary target.

3.3 The S800 spectrograph

From the focal plane of the A1900, the cocktail secondary beam was delivered to the secondary ^{9}Be target with a thickness of 375 mg/cm^2 located at the pivot point of

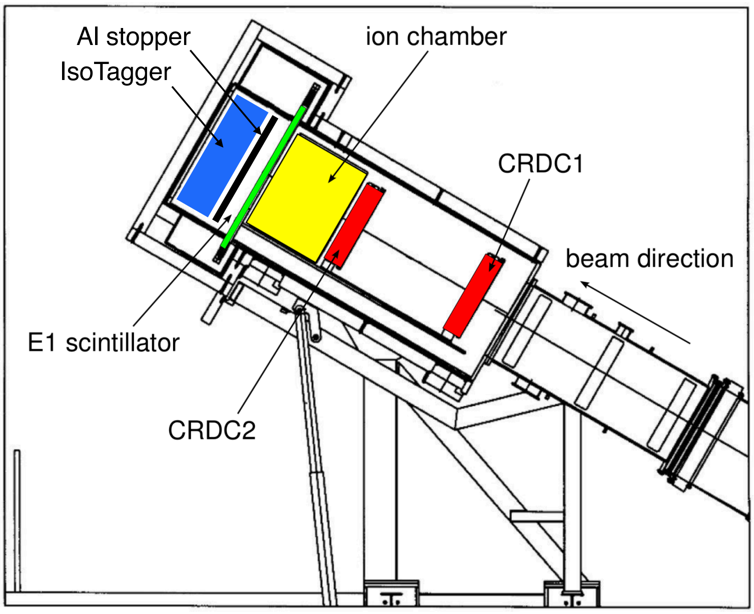

Figure 3.3: A schematic of the focal plane box of the S800. The IsoTagger array was placed downstream of the E1 scintillator. Taken and modified from [95].

the S800 spectrograph [89], as is shown in Figure 3.2. This was where the reaction of interest took place. The S800 is a large acceptance and high resolution spectrometer relying on superconducting magnets. The spectrometer spans vertically and the particle identification (PID) of both incoming and outgoing isotopes was performed here. The S800 consists of three parts: the analysis line, the spectrograph itself, and the focal plane box.

The analysis line, leading to the secondary target position, is used for the beam diagnostics and tuning the optics mode of whole spectrometer. It is made of two pairs of two 22.5° dipoles and five quadrupole triplets with a maximum magnetic rigidity of 4.9 Tm. The very beginning of the analysis line is the object focal plane (OBJ) and the focal plane between two dipole pairs is the intermediate image (II). The assemble of the magnets and thus the optics of the analysis line is symmetric for OBJ-II and II-secondary target. The detectors placed on OBJ and II will be described in the following sections.

The spectrometer part consists of a superconducting quadrupole doublets and two superconducting dipoles spanning from the secondary target to the focal plane. Its angular acceptance is ±5° in non-dispersive and ±3.5° in dispersive direction, resulting in the total solid angle of 20 msr. Its maximum rigidity is 4 Tm and momentum acceptance is 5%. In the present experiment, the optics of the S800 spectrometer was operated in focused mode. In this mode, the secondary beam was focused in OBJ and secondary target position and the focal plane was momentum dispersive, with a momentum dispersion of 9.5 cm/%.

Located at the very end of the S800 is the focal plane and several detectors for particle identification (PID) and measurement of particle trajectory were equipped in the focal plane box [95]. Figure 3.3 shows a sketch of the focal plane box and detectors. Note that the IsoTagger array, which will be described in §3.4.2 was placed downstream of the E1 scintillator in this figure. The details will be described in the following subsections.

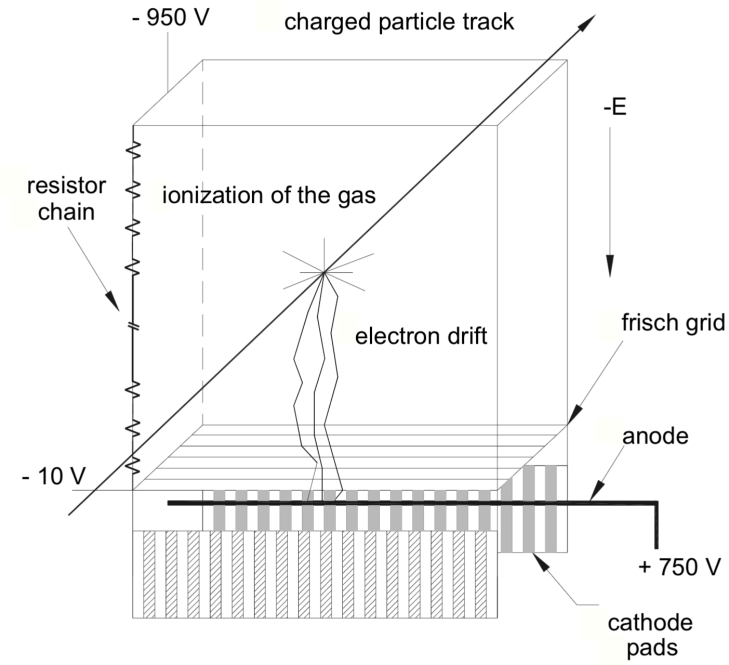

Figure 3.4: A schematic of the CRDC. Taken from [96].

3.3.1 Particle trajectories

The focal plane box is equipped with two cathode readout drift chambers (CRDCs). The upstream CRDC is located at the nominal focal plane of the S800 spectrograph and the other one is placed 1073 mm downstream. Both detectors have the active area of 26 cm × 56 cm, in non-dispersive and dispersive direction, respectively, and the active depth of 1.5 cm [95]. These chambers are filled with the mixture of 80% CF_4 and 20% C_4H_{10} gas and the operational pressure is typically about 50 torr.

The projectile-like particle passes through the CRDCs and ionizes the gasous material described above. Produced electrons and ions are separated by a static electric field, E in Figure 3.4. This electric field is applied between the top edge of the frame and the Frisch grid, where typical high voltages of -950 and -10 V are applied, respectively. The electrons drift toward the Frisch grid without any avalanche effect. An anode wire is just behind the Frisch grid with a high voltage of 750 V, inducing avalanche effect and thus multiplying the number of drifting electrons. The anode wire is surrounded by 224 cathode pads with 2.54 mm pitch. The induced charges from the collection of electrons on the anode wire are read from cathode pads and the charge distribution corresponds to the position of the particle trajectory in x-direction. The position in y-direction is determined by the drift time of electrons to the anode wire with respect to the trigger signal produced by the E1 scintillator. The maximum drift time is up to 20 μs with regard to the particle trajectory. Resulting position resolution is better than 0.5 cm.

The resulting coordinates on the focal plane, x_{fp} and y_{fp} at the upstream CRDC, and angles, a_{fp} and b_{fp}, respectively, are used to deduce the non-dispersive position, y_{ta}, angles, a_{ta} and b_{ta}, and the energy parameter, d_{ta} at the secondary target position by an inverse map. The inverse map describes the trajectory of a charged particle passing through the magnetic field of the S800 spectrograph and calculated by the code COSY Infinity [97]. Note that $d_{ta} = \Delta E/E$ is defined as the difference in energy of the particle and of a particle on the central trajectory of the S800 spectrograph.

Combining with the magnetic rigidity $B\rho$ setting of the S800, the energy-momentum 4-vector of the reaction residue can be deduced.

As described above, d_{ta} is one of the parameters calculated from the particle trajectory at focal plane and the dispersive position at the target position, x_{ta} cannot be reconstructed using the inverse map. This procedure results in the resolution of d_{ta} convoluted by the finite beam spot size along the dispersive direction at the target position. To improve the resolution of d_{ta}, two tracking parallel plate avalanche counters (PPACs) are placed at the intermediate plane of the analysis line of the S800. Each PPAC has the active area of 10 cm × 10 cm and is filled with isobutane gas with a typical pressure of 5 torr. A PPAC consists of an anode plate between two cathode foils having 64 aluminum strips each with the pad pitch of 1.27 mm. One of the cathode foil is oriented in the non-dispersive direction and the other is in the dispersive direction. The secondary beam passing through the PPACs ionizes the gas and produces electrons and positive ions. The drift of electrons to the anode plate induces the image charge to the strips on the cathode plates and this charge distribution corresponds to the two dimensional position of the beam particle.

3.3.2 Time-of-flight

In order to identify both incoming and outgoing particles, three plastic scintillators were installed in the beam line and the time-of-flight (ToF) between them was measured. Two scintillators were placed at XFP of A1900 and at OBJ of S800, whose signals were used as the start signal of ToF. The other scintillator was placed at the very end of the S800 spectrograph, called E1, and used as the stop signal of ToF measurement and the trigger signal of the data acquisition of S800 detectors. These ToF measurements were for the separation of mass, m, of both incoming and outgoing particles. As described in §3.4, the momentum spread of the secondary beam was restricted to ±0.5%. Assuming a constant momentum of the secondary beam and the constant flight length along the beam line, the relationship of ToF $\propto 1/\beta \propto m$ can be used for the PID. The detectors are made of polyvinyltoluene (>97%) and organic fluors (<3%) with a density of 1.032 mg/cm^2 and a refractive index of 1.58. The detector thickness of the scintillators at OBJ and E1 are 127 μm and 1 mm, respectively. Two photomultipliers EMI 98807B are connected to both ends of the E1 scintillators and the average timing of the signals from both photomultipliers was used.

3.3.3 Ionization chamber

An ionization chamber is used for the identification of the proton number of the outgoing particle. This detector is placed between the downstream CRDC and the E1 plastic scintillator. The approximate active area is 30 cm × 60 cm, non-dispersive and dispersive direction, respectively, and the active depth is about 40.6 cm. This chamber is filled with a mixture of 90% Ar and 10% methane at a typical pressure of 300 torr. The whole detector consists of 16 stacked parallel plate ion chambers which are placed along the beam axis with narrow anode-cathode gaps. Charged particles passing through the chamber ionize the gas along their trajectories and the electrons produced drift to the closest anode-cathode pair. Owing to the anode-cathode configuration, the drift length of electrons and ions is quite short, about 1.5 cm, compared to the whole detector size, reducing pile-up events and position dependence of signals. The number of electrons corresponds to the energy deposited in the gas, which is described by the Bethe-Bloch formula (3.2).

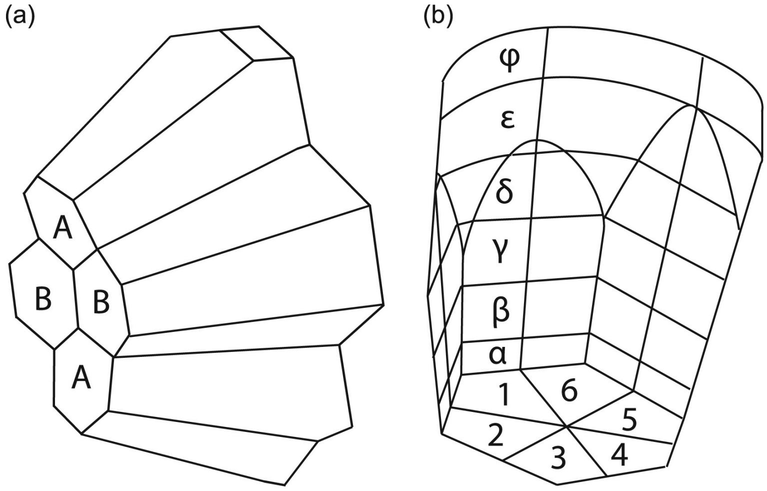

Figure 3.5: A schematic of the crystal of the GRETINA array. Taken from [90].

3.4 Gamma-ray detectors

In the present experiment, two kinds of gamma-ray detectors were installed to measure the de-excitation γ-rays emitted from the reaction residues. The excitation energies and the cross sections to populate excited or ground states of the reaction residues were determined by the energies and the detection yields of detected γ-rays. The level scheme was constructed by analyzing the γ-γ coincidences between prompt as well as delayed γ-rays.

3.4.1 The GRETINA array

The prompt de-excitation γ-rays were measured by the Gamma Ray Energy Tracking In-beam Nuclear Array (GRETINA) [90, 98] surrounding the secondary target. GRETINA consists of eight clusters of four segmented coaxial high purity Germanium (HPGe) detectors. The detectors are made of n-type HPGe with less than 1.8×10^{10} cm^{-3} net impurity concentration. Each crystal is tapered in two types of hexagonal shapes at the front face (A-type and B-type crystals as Figure 3.5), to be closely packed in a spherical shell. Original crystal size before tapering is about 90 mm in length and 80 mm in diameter. Each crystal has a central contact extending 15 mm from the front face of the crystal with a diameter of 10 mm. The outer contact is divided in 36 pads with six longitudinal and six transverse segmentation with less than 0.5 mm gaps. Transverse segmentation makes rings of outer contacts with width of 8, 14, 16, 18, 20, and 14 mm from the front end of the crystal, from α to φ. Figure 3.5 shows the geometry of the crystal and the segmentation of the outer contacts. Two A-type detectors and two B-type detectors are packed into a quad module with a common cryostat. Eight quads were used for the present experiment providing more than 1π solid angle coverage. Four quads were placed at 58° and the others were at 90° with respect to the beam axis at a distance of about 18 cm from the secondary target to the front face of the detectors.

One of the most important assets of the GRETINA array is its ability to reconstruct the positions of γ-ray interactions in detectors with a sub-segment position resolution. From the segment where the γ-ray interaction occurred the net charge is measured, while in neighboring segments an induced image charge is recorded. The rise time of the signals from the hit segment and the central contact is sensitive to the

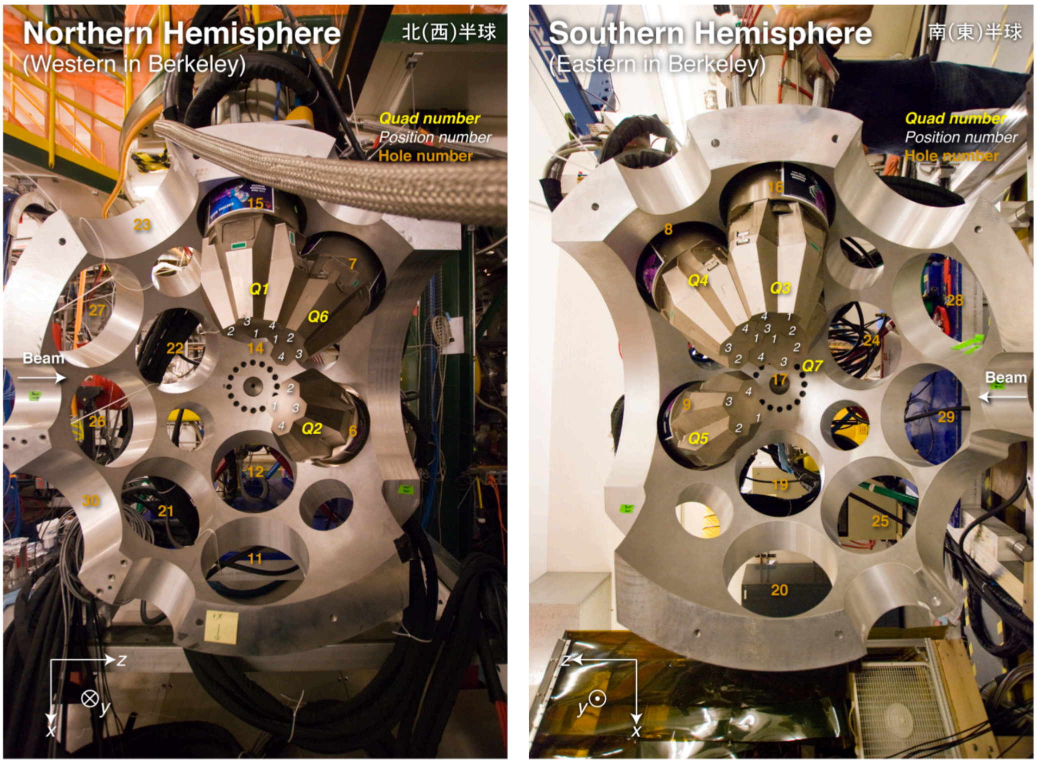
Northern Hemisphere
(Western in Berkeley)
北(西)半球
Quad number
Position number
Hole number
Beam
Q1
Q6
Q2
15
23
7
27
22
14
6
26
12
30
21
11
z
x
y
Southern Hemisphere
(Eastern in Berkeley)
南(東)半球
Quad number
Position number
Hole number
Q4
Q3
Q7
Q5
16
8
28
24
17
Beam
29
9
19
25
20
z
y
x

Figure 3.6: Picture of the GRETINA mount. In this picture, orange numbers represent the hole number, yellow numbers are the quad number, and the white numbers are the crystal number of each quad. Note that this picture was taken in the previous GRETINA campaign (2012). In the present experiment, 8th quad was additionally mounted in the hole 14. Taken from [67], picture courtesy of S. Noji.

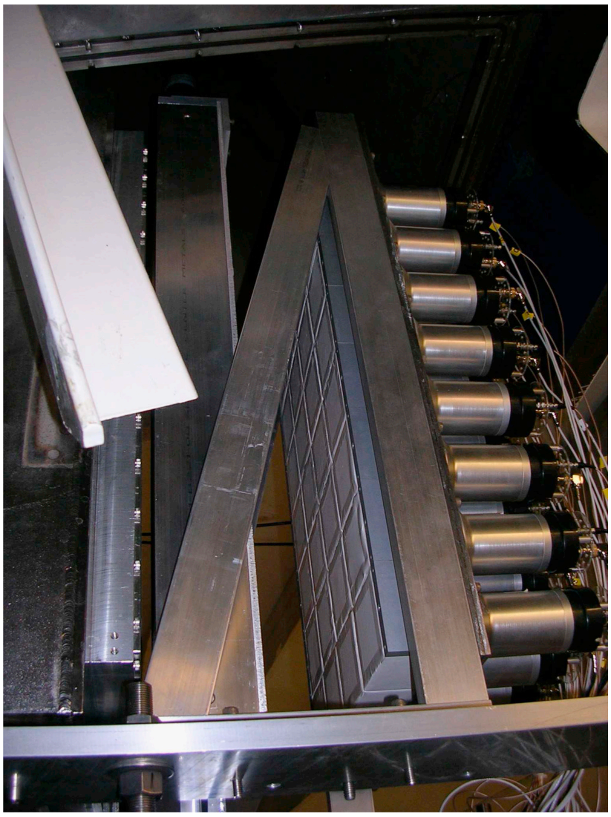

Figure 3.7: Picture of the IsoTagger array. The focal plane box was opened. Taken from [91].

drift time of the charge carriers, which reflects the distance of interaction point from the readout electrodes. The shape and the amplitude of the signal of image charges detected in neighboring segments contain the information of the depth and the polar angle of the interaction point as the other two cylindrical coordinates. The GRETINA readout electronics record signal pulses from the segments and the central contacts by digitizing them. Also, the GRETINA system has a dedicated the computer farm for signal decomposition. Typically a single γ-ray interacts multiple times with a single detector or even with a single segment until fully absorbed. This means that measured signals are the superposition of the signals of the single interaction point. Here, the measured signals are fit against a linear combination of simulated basis signals and γ-ray energy deposition and positions are reconstructed. These basis signals represent detector response to a unit charge deposited at a given point in the detector and are simulated with an average spacing of 1 mm.

3.4.2 The IsoTagger array

In some cases, the reaction residue has an excited state with the lifetime long enough to pass the acceptance of the γ-ray detectors surrounding the secondary target. It then becomes difficult to construct the level scheme of this nucleus and thus to deduce the production cross section of each final state. In this case the end point of γ-ray cascades could either be the ground state or an isomeric state. In order to solve this problem, the γ-ray detector array, IsoTagger [91], was placed at the very end of the S800 spectrograph. It is specifically designed to measure the γ decay of isomeric states in the nucleus of interest.

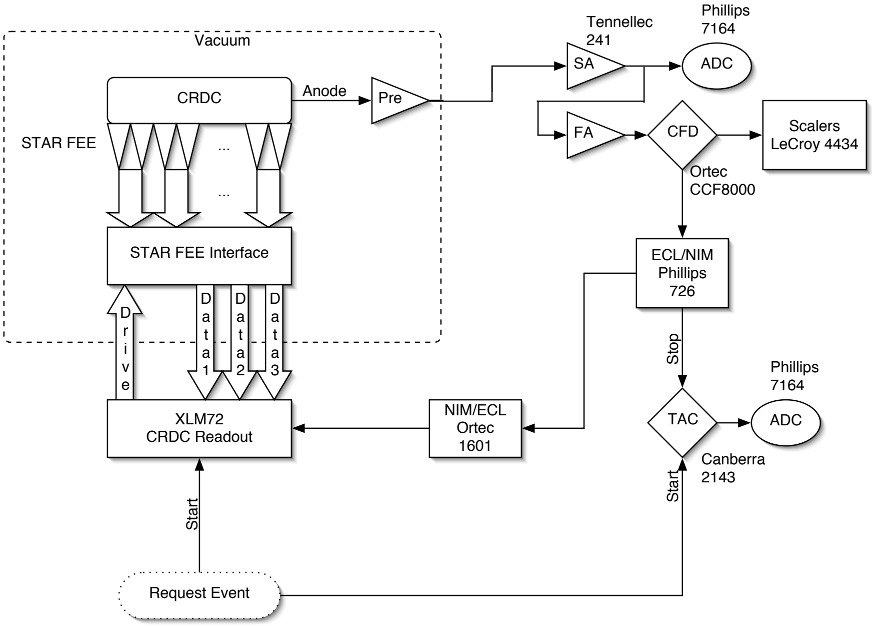
Vacuum
CRDC
Anode
Pre
STAR FEE
...
STAR FEE Interface
Drive
Data 1
Data 2
Data 3
XLM72
CRDC Readout
Start
Request Event
NIM/ECL
Ortec
1601
Tennellec
241
SA
Phillips
7164
ADC
FA
CFD
Scalers
LeCroy 4434
Ortec
CCF8000
ECL/NIM
Phillips
726
Stop
TAC
Phillips
7164
ADC
Canberra
2143
Start

Figure 3.8: Schematic diagram for the electric circuit of the CRDC detectors. Taken from [99].

The IsoTagger consists of 32 CsI(Na) crystals shown in Figure 3.7. These crystals are closely packed as 4 × 8 in non-dispersive and dispersive direction, respectively. The size of each crystal is 82.5 × 82.5 × 51 mm^3. This array is usually used for measuring the total kinetic energy of reaction residue. For γ-ray detection, the Al stopper plate is placed behind the E1 scintillator and the IsoTagger array is placed 10.5 cm downstream of the stopper to maximize the geometric efficiency. The thickness of the Al stopper is chosen to be 6.35 mm, which is thick enough to fully stop both the nuclei and lighter tertiary reaction product produced in the implantation process. Not only the energy and yield of the de-excitation γ-ray from the isomeric state are measured, but also the complete level scheme above and below the isomeric state is constructed by taking the delayed coincidence with prompt γ-rays measured by the GRETINA array at the target position. Additionally, from the detection timing of the delayed γ-ray the lifetime of the isomeric state can be deduced.

3.5 Readout and data acquisition system

The electric circuits for the signal processing of detectors are shown in figures from 3.8 to 3.12.

Both CRDCs are equipped with seven front-end electronic boards (FEE) as shown in 3.8. Each FEE consists of 32 channels of preamplifiers followed by a switch capacitor array (SCA) and an ADC. A SCA samples the wave form of the signal from CRDCs, typically 20 MHz and 8 to 12 samples, and send it to an analog-to-digital converter (ADC). The signal processing of this sampling needs about 16 μs which is the largest dead time in the typical setting of the experiment. The signal from PPAC detectors are also treated as the same manner as CRDCs shown in Figure 3.9. For the signal processing of PPACs, a SCA samples in more frequent rate, typically 200 ns.

The signals from the ionization chamber are first sent to a shaper amplifier and then sent to an ADC as shown in Figure 3.10. The gain of each shaper amplifier are

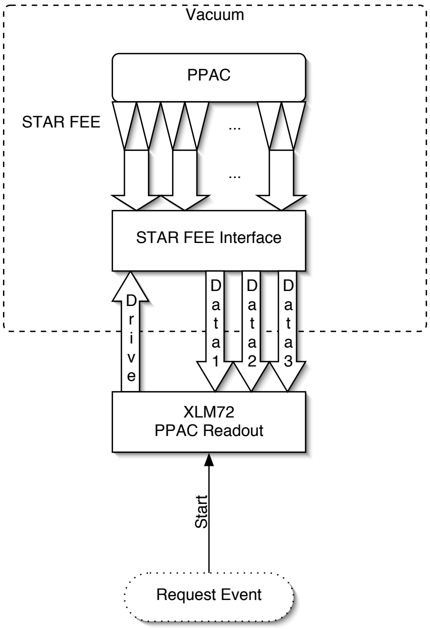
Vacuum
PPAC
STAR FEE
...
...
STAR FEE Interface
Drive
Data 1
Data 2
Data 3
XLM72
PPAC Readout
Start
Request Event

Figure 3.9: Schematic diagram for the electric circuit of the PPAC detectors. Taken from [99].

adjusted remotely.

The photomultiplier output (Hamamatsu R1307) of each scintillator of the IsoTagger array is divided for the energy and timing measurement as shown in Figure 3.11. The signal goes to a shaper amplifier followed by an ADC for the energy measurement. The other one is sent to a constant fraction discriminator (CFD) and then input to the stop signal for a time-to-amplitude converter (TAC).

The signal processing of the photomultipliers attached to the plastic scintillators for the timing measurement is shown in Figure 3.12. The signal goes to a fast amplifier and then is treated as the stop signal of a time-to-digital converter (TDC). The start of a TDC module is the signal from E1 scintillator. Also for counting the number of particles passing through the scintillators, the CFD output is sent to a scaler.

The signal processing described above, related to detectors equipped in the S800

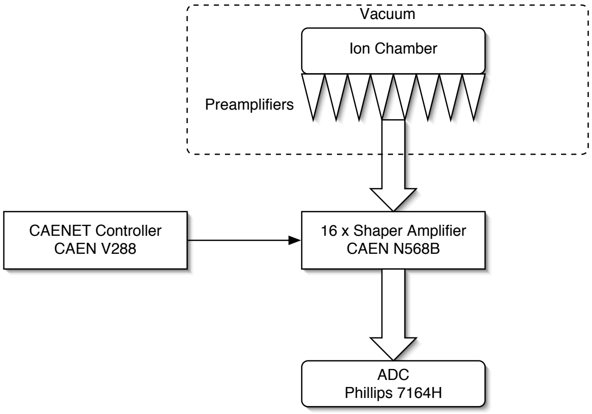
Vacuum
Ion Chamber
Preamplifiers
CAENET Controller
CAEN V288
16 x Shaper Amplifier
CAEN N568B
ADC
Phillips 7164H

Figure 3.10: Schematic diagram for the electric circuit of the ionization chamber. Taken from [99].

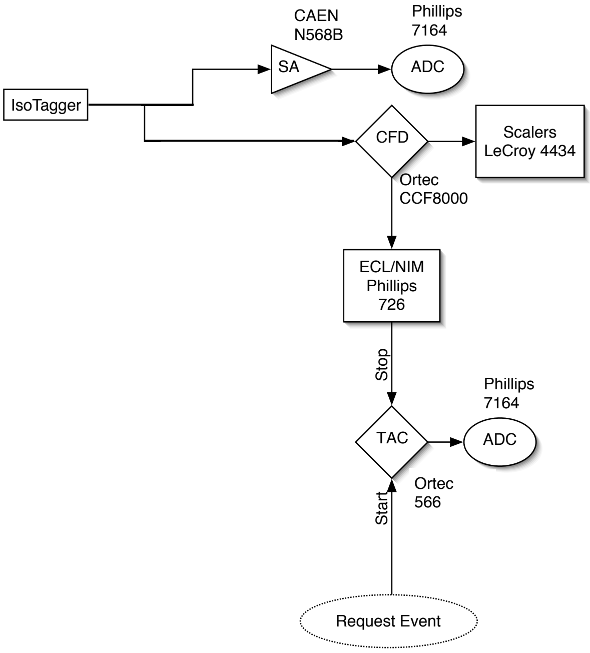
CAEN
N568B
Phillips
7164
SA
ADC
IsoTagger
CFD
Scalers
LeCroy 4434
Ortec
CCF8000
ECL/NIM
Phillips
726
Stop
Phillips
7164
TAC
ADC
Ortec
566
Start
Request Event

Figure 3.11: Schematic diagram for the electric circuit of the IsoTagger array. Taken from [99] and modified.

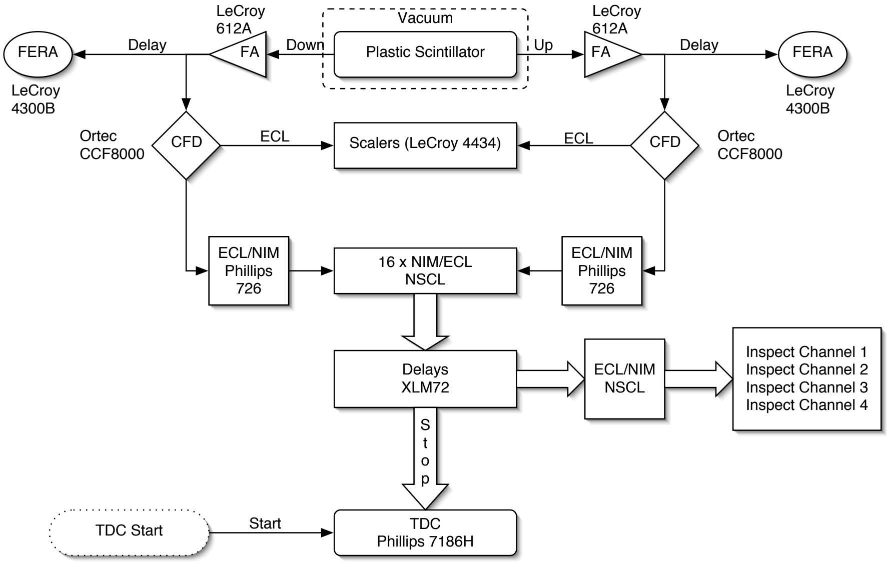
LeCroy
612A
Vacuum
LeCroy
612A
FERA
Delay
FA
Down
Plastic Scintillator
Up
FA
Delay
FERA
LeCroy
4300B
LeCroy
4300B
Ortec
CCF8000
CFD
ECL
Scalers (LeCroy 4434)
ECL
CFD
Ortec
CCF8000
ECL/NIM
Phillips
726
16 x NIM/ECL
NSCL
ECL/NIM
Phillips
726
Delays
XLM72
ECL/NIM
NSCL
Inspect Channel 1
Inspect Channel 2
Inspect Channel 3
Inspect Channel 4
Stop
TDC Start
Start
TDC
Phillips 7186H

Figure 3.12: Schematic diagram for the electric circuit of the plastic scintillators for timing measurement. Taken from [99].

spectrograph, are under the data taking system (DAQ) of the S800. Besides the DAQ for S800, the GRETINA array has its own DAQ and they ran in parallel in the present experiment. The time of the data taking in both DAQ system was recorded by the common timestamp. This timestamp information was used for the event building in the following analysis [100].

The S800 DAQ system were fired by two trigger conditions. One was the trigger made by the signal from the E1 scintillator. This trigger condition means that the projectile-like particle reached the very end of S800. The other one is the coincidence trigger of the E1 signal and the GRETINA. In all the knockout setting runs of ^{44}S→^{43}S, there was no down scale of the trigger made by the E1 scintillator, which means that the S800 DAQ was always fired by charged particles. In some runs in which the S800 magnet was set to unreacted ^{44}S particles, measurement of the isomer ratio of this nucleus for example, down scale for the E1 trigger was applied. In such condition, the coincidence trigger could fire the S800 DAQ system. Note that during some calibration measurements of the γ-ray detectors, GRETINA or IsoTagger fired the whole DAQ system.

Chapter 4

Analysis

This chapter describes the calibrations and treatment of the recorded data prior to deducing the physics observables. In §4.1, calibration of the beam line detectors will be described, followed by the particle identification. In §4.2 and §4.3, γ-ray analysis will be discussed for both the GRETINA and the IsoTagger arrays. The analysis regarding the parallel momentum distributions will then be presented in §4.4.

4.1 S800

This section describes the treatment of the data measured by the detectors in the focal plane box of the S800 and scintillators placed upstream of the secondary target. These detectors provide the particle identification and the momentum distribution of reaction residues.

4.1.1 Cathode readout drift chambers

The charge deposition in each of the two CRDCs was measured by 224 cathode pads individually and the centroid of this charge distribution was calculated to determine the x position of particles passing through. To properly deduce the charge distribution, the gain of each pad was matched and the response of the pads was unified across all 224 pads. Figure 4.1(a) and (b) show the charge value measured in each pad before and after the gain matching procedure, respectively. This is part of the whole beam experiment with the one-neutron knockout setting. The 111th channels in both CRDCs were arbitrarily chosen to be the matching channel. Rough particle identification cuts for outgoing particles were applied to ensure the selection of isotopes for a constant energy loss. In the present experiment, gates for outgoing particles of $Z = 12, 13,$ and 14 were applied and a linear function was used to match the measured charge values to the matching channel after subtracting the pedestal value in each pad. Note that charge values shown in these figures are defined as the maximum charge value among all pads fired in an event. Due to this definition, this calibration procedure is iterative because changes in calibration parameters could result in the maximum charge value in the different channel. Because of the beam blocker placed in front of the upstream CRDC in order to stop the unreacted projectile, there is no recorded charge in pads from 0 to around 50, but this part of the detector was not used in the experiment.

After the gain matching calibration, the central pad number of the charge distribution is used to calculate the x position as below,

$$x = C_{x1} \times \frac{\sum_i i \times Q_i}{\sum_i Q_i} + C_{x2}, \tag{4.1}$$

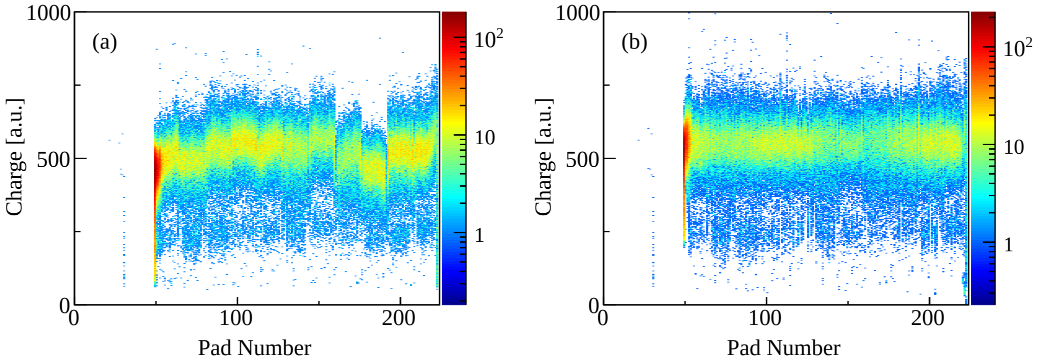

Figure 4.1: Result of the gain matching analysis for 224 channels of the downstream CRDC. (a) and (b) show the recorded charge values in each pad before and after the gain matching, respectively. Gates on incoming ^{44}S and outgoing S isotopes have been applied.

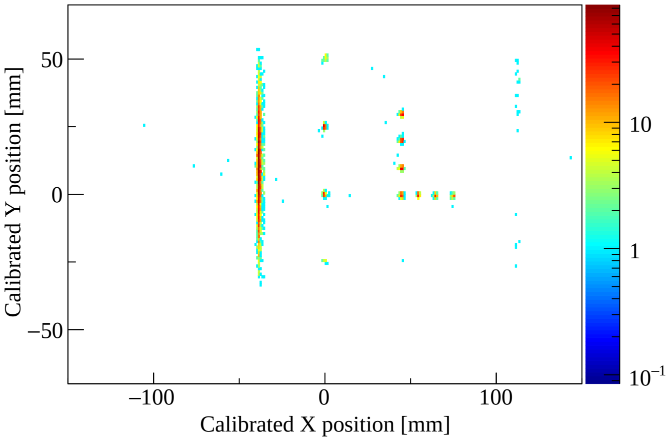

Figure 4.2: Result of the mask calibratoin of the downstream CRDC. The centroid of the charge distribution and the drift time of electrons were converted to the real position coordinates to reproduce the known positions of the holes or slits in the mask.

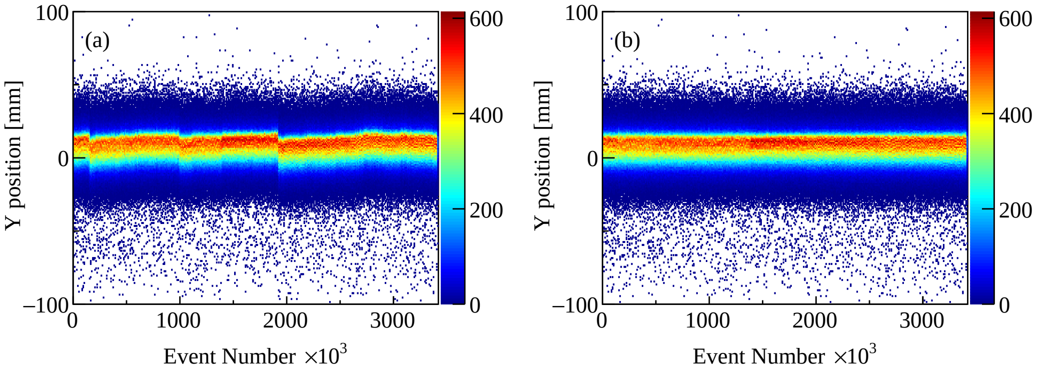

Figure 4.3: Correction for y position measured by the upstream CRDC against the experiment time. Drift of the measured position can be caused by the variation in temperature of pressure in the detector.

where Q_i is the charge value in arbitrary unit measured in i-th pad and C_{x1} and C_{x2} are calibration parameters to convert the pad number to the real coordinate. C_{x1} was chosen to be 2.54 mm which corresponds to the pad width in mm and the offset value C_{x2} was determined by analyzing separate mask runs. In mask runs a tungsten plate with holes and slits at known coordinates was inserted just in front of a CRDC. This mask is thick enough for charged particles to stop in the plate. Figure 4.2 shows the result of mask calibration for the downstream CRDC. C_{x2} was calculated to reproduce the coordinates of holes and slits in mask runs. To deduce y position, the drift time of electrons measured by the anode wire was used and converted to mm using the same mask runs.

To account for the change of the gas pressure and temperature during the beam time causing a shift of the measured charge distribution and drift time, mask runs were performed periodically over the whole experiment. Drifts in between the calibration runs were corrected for interpolating between the mask runs, as shown in Figure 4.3. The measured y position was aligned to the mean y position just after the mask runs. This correction was done separately for the different magnetic rigidity settings of the S800 spectrograph. Such kind of drift correction was also applied to the charge value measured by the ionization chamber and the ToF measured by using scintillators at OBJ and XFP (see below).

4.1.2 Time-of-flight

As mentioned in section §3.3.2, two time-of-flight measurements, XFP-E1 and OBJ-E1, were used for the particle identification. The time-of-flight between the XFP and the OBJ scintillators is proportional to the mass of the incoming particle, so the particle identification of incoming particles was performed by investigating two dimensional plot of XFP-E1 and OBJ-E1 time-of-flight measurements. Outgoing particles were identified by the combination of the energy loss measured in the ionization chamber which is described in §4.1.3 and the OBJ-E1 time-of-flight, which is sensitive to the mass of outgoing particle. The flight path through the S800 spectrograph depends on the angle and momentum of the particle, so the OBJ-E1 time-of-flight was corrected by assuming linear dependences of these parameters as

$$\mathrm{OBJC} = \mathrm{OBJ} + C_1 \times x_{fp} + C_2 \times a_{fp}. \tag{4.2}$$

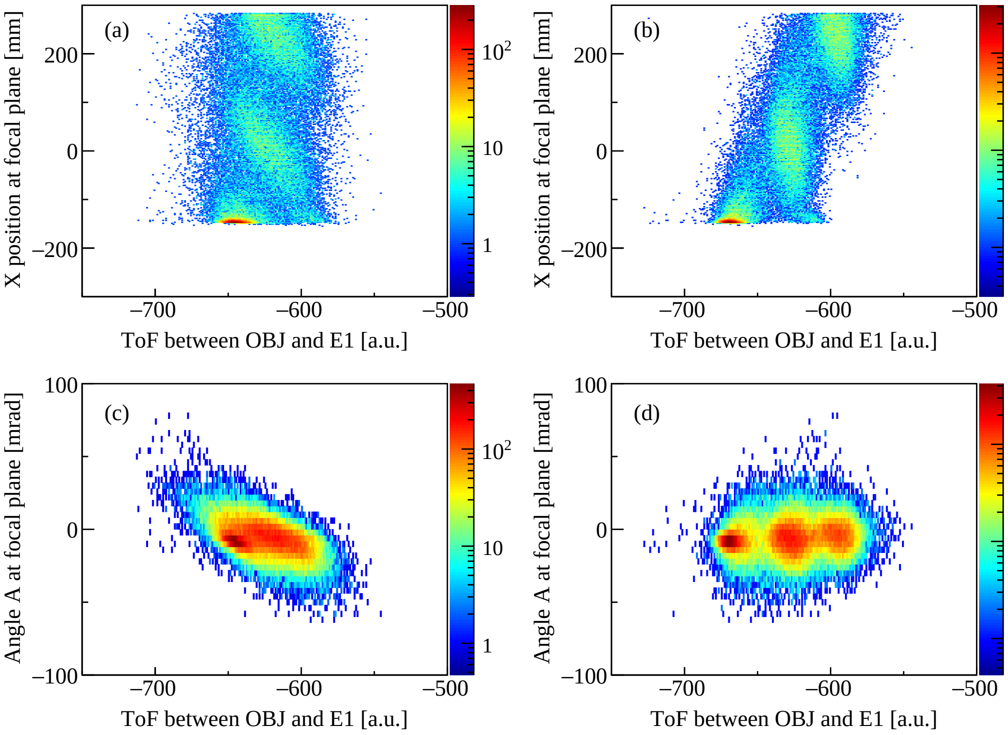

Figure 4.4: Correction to the ToF between OBJ and E1. (a) and (b) show the histograms before and after the correction using the dispersive position (x) at the focal plane. (c) is before the correction using the dispersive angle (a), and (d) is after the iterative correction with both x and a.

Two correction parameters C_1 and C_2 are deduced to obtain the best resolution of the OBJ-E1 time-of-flight. The result of this correction is shown in Figure 4.4. First, only C_1 is varied and fixed to the value for the best ToF resolution. Practically, this procedure is performed by checking the two dimensional correlation between the ToF and the x_{fp}, as shown in the panel (a) of Figure 4.4. By eliminating the x_{fp} dependence on the ToF, which means the correlation between the ToF and the x_{fp} is vertical against the ToF axis, X axis in the panel (a) of Figure 4.4, and the narrowest peak width of the one dimensional ToF histogram, the correction parameter C_1 is tentatively deduced, as shown in the panel (b) of Figure 4.4. Then C_1 is fixed and C_2 is searched for the better ToF resolution. These parameters can affect with each other, so this procedure is performed iteratively. Final result of this correction is shown in panel (d) of Figure 4.4.

4.1.3 Ionization chamber

Prior to the calculation of the energy deposition in the whole ionization chamber, the gains of 16 segments were matched. The second segment was arbitrarily chosen to be the matching channel. By applying rough particle identification gates for outgoing particles with $Z = 14$, 15, and 16, the calibration parameters of the linear function for the remaining 15 channels were obtained by matching to the charge values measured in the second channel. Figure 4.5 shows the recorded charge in each segment before and after this gain matching procedure.

The energy deposition by projectile-like particles were deduced by the mean of charges measured by all the fired segments in an event. The energy loss through the

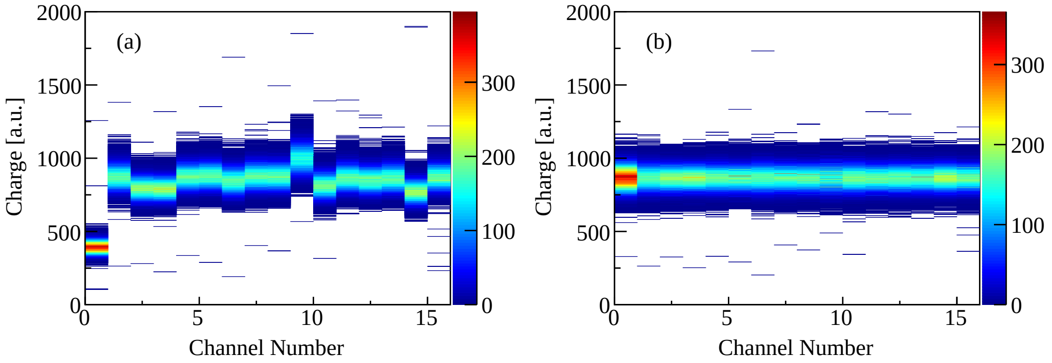

Figure 4.5: Result of the gain matching analysis for 16 channels of the ionization chamber. (a) and (b) show the recorded charge values in each channel before and after the gain matching, respectively. Gates on incoming ^{44}S and outgoing S isotopes were applied.

whole chamber, E, depends on the pass length in the chamber. The energy loss was corrected accounting for the x position in the focal plane of the S800 spectrograph as

$$E_{cor} = E \cdot \exp(p \cdot (x - x_0)) \quad \text{for} \quad x < x_0, \tag{4.3}$$

where p and x_0 are the fitting parameters to the two dimensional plot of x and E, as shown in Figure 4.6. Figure 4.6(a) is the spectrum before the correction and the red dashed line in this panel corresponds to Equation (4.3). The result of this correction is Figure 4.6(b).

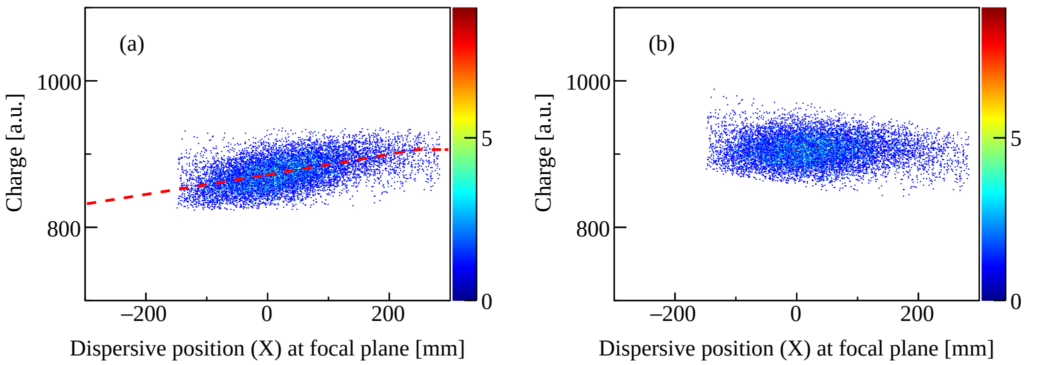

Figure 4.6: Result of the position correction analysis for the ionization chamber. (a) and (b) show the recorded charge values before and after the position correction, respectively. The red dashed line corresponds to the function used for the position correction described in Equation (4.3). Gates on incoming ^{44}S and outgoing ^{43}S were applied.

4.2 Analysis for GRETINA

In this section, the analysis for the GRETINA detector array to measure the prompt γ-rays are described. First, the energy recalibration of the GRETINA crystals are described. To enhance the peak count of the γ-ray energy histogram and make γ-γ coincidences within the GRETINA or between the GRETINA and the IsoTagger, an

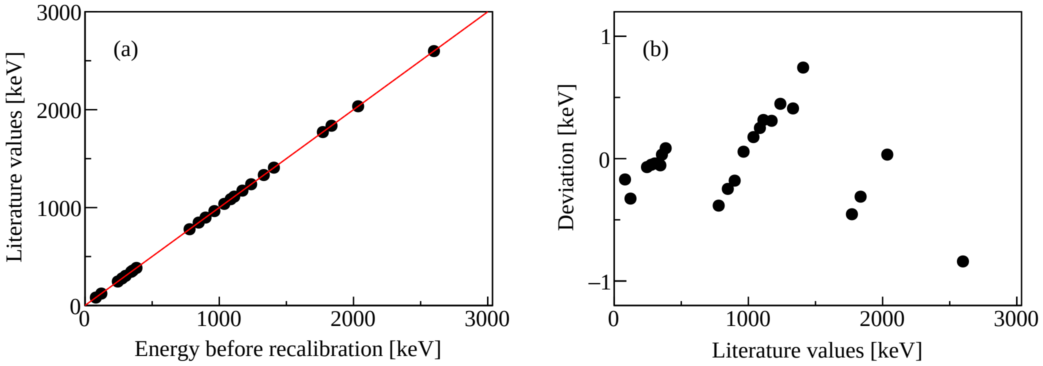

Figure 4.7: Result of energy recalibration of a single crystal of GRETINA. The energy outputs of GRETINA detector measured by using standard radiation sources before recalibration and corresponding peak energies are plotted in Figure (a). The red line shows the linear function used for recalibration. Figure (b) shows the deviation of recalibrated energies and literature values. Note that error bars of the energy recalibration are negligibly small.

addback procedure were used. The γ-ray yields emitted from excited states of ^{43}S are deduced by the fitting of the simulated response function to the experimental γ-ray energy histogram. To properly deduce the γ-ray yields, the treatment of the simulated data and a comparison of the efficiency measured with the standard radiation sources is described in §4.3.2. Prompt γ-rays measured by the GRETINIA were emitted from the particles moving with a velocity of about $\beta \sim 0.4$. The procedure performed to reconstruct the emitted γ-ray energy in the ejectile rest frame is described in §4.3.3. Non-negligible amount of γ-rays from the surrounding materials or the GRETINA detector itself were also observed, as shown in §4.2.5.

4.2.1 Energy recalibration

As described in §3.4.1, γ-ray energies are deduced by the signal decomposition algorithm online. This means that an energy calibration of the crystals is necessary prior to the measurement, and also that the output values written to the recorded data file are already in units of energy. An energy calibration for each segment and crystal had been performed at the beginning of the experiment. So, in principle, there is no need to perform an energy calibration offline for the recorded data. However, gain drifts can occur over the period of the experiment. In the present experiment, calibration data was taken both before and after the measurement with the radioactive beam. It was found that no significant gain drift did occurred, but the energy outputs of some crystals had already been shifted during the measurement. So energy recalibration was performed prior to the further analysis.

The calibration measurement was done with the standard radiation sources of ^{56}Co, ^{60}Co, ^{88}Y, ^{133}Ba, and ^{152}Eu. Peaks with more than 7% of the total intensity per decay, shown in Table 4.1, were chosen for the recalibration. The γ-ray energies were deduced by fitting gaussian functions with linear background functions to the experimental spectra. Figure 4.7 shows the result of the energy recalibration for a single crystal. A linear function was used for the recalibration and general linearity was confirmed in the whole array as is shown in Figure 4.7(a). Figure 4.7(b) shows energy differences between deduced γ-ray energies and the corresponding literature

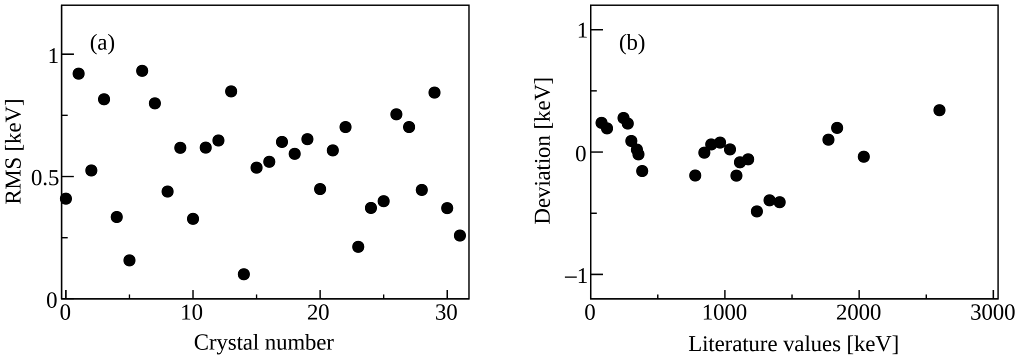

Figure 4.8: Result of energy recalibration of whole GRETINA array. Root-mean-square of the deviation of recalibrated energies and literature values calculated in each crystal is plotted in Figure (a). Figure (b) is the same kind of plot as Figure 4.7 but calculated for the whole array. Note that error bars of the energy recalibration are negligibly small.

Table 4.1: Standard radiation sources used for the calibration of the GRETINA. Values are taken from [101].

Nuclide	Half life	Activity	Energy [keV]	Intensity per decay [%]
^{56}Co	77.27d		846.7938(29)	99.933(7)
			1037.8333(24)	14.13(5)
			1238.2736(22)	66.07(19)
			1771.327(3)	15.49(5)
			2034.752(5)	7.771(27)
			2598.437(4)	16.96(6)
^{60}Co	5.2714y		1173.228(3)	99.857(22)
			1332.490(6)	99.983(6)
^{88}Y	106.65d		898.036(4)	94.0(3)
			1836.052(13)	99.36(3)
^{133}Ba	10.52y		80.9971(12)	34.11(28)
			276.3997(13)	7.147(30)
			302.8510(6)	18.30(6)
			356.0134(6)	61.94(14)
			383.8480(12)	8.905(29)
^{152}Eu	13.542y	46.0 kBq	121.7817(3)	28.37(13)
			244.6975(8)	7.53(4)
			344.2785(13)	26.57(11)
			778.9045(24)	12.97(6)
			964.1	14.63(6)
			1085.836(9)	10.13(5)
			1112.9488(11)	13.54(6)
			1408.011(4)	20.85(9)

values. The energies of the observed γ-rays were well reproduced by the recalibration procedure with a energy deviation of less than 1 keV in the energy range of 80 to 2600 keV. Figure 4.8(a) shows the root-mean-square values of the deviations between calibrated energies and the corresponding literature values calculated for individual crystals summed in all the peaks. The recalibration procedure is able to reproduce the energies with less than 1 keV difference for all the crystals. Finally, Figure 4.8(b) displays the same kind of analysis as Figure 4.7(b) but for the whole GRETINA array. From this result, less than 0.5 keV can be used as the the uncertainty of energy recalibration.

4.2.2 Treatment of γ-ray event and addback analysis

In the present experimental situation, a single γ-ray can interact with the Ge of the GRETINA detector multiple times. For the high energy γ-rays especially, γ-ray can undergo multiple Compton scattering:

$$E'_\gamma = \frac{E_\gamma}{1 + E_\gamma/m_e(1-\cos\theta)}, \tag{4.4}$$

where E'_γ is the energy of the scattered γ-ray and θ is the γ-ray scattering angle. If a single γ-ray interacts by multiple Compton scattering events, the deposited energy at each interaction point no longer reflects the γ-ray energy emitted from the reaction residue, but the sum of energy deposits equals to the γ transition. To solve this situation, it was simply assumed that all interaction points within a single segment originated from the same γ-ray. This is a reasonable procedure in case of low γ-ray multiplicities in the present experiment for one-neutron knockout reactions. In this analysis, the first γ-ray interaction point was taken from the interaction point with the maximum energy deposition in the segment. For the Doppler correction, described in §4.3.3, this is also an reasonable assumption because the error of the γ-ray emission angle is small due to the small γ-ray scattering angle by Equation 4.4 if the first interaction point is not the one with the maximum energy deposition.

For an improved peak-to-total ratio of the γ-ray energy histogram compared to the singles spectrum described above, an addback procedure was performed in the present work. In this analysis, possible combination of all the interaction points was examined and if the γ-ray emission angles with respect to the secondary target between two γ-rays were smaller than a specific angle α, these γ-rays were clustered and their energies were summed. The clustering angle was chosen to be $\alpha = 25^\circ$ in this work. For the Doppler correction, the γ-ray interaction was taken from the point with the largest energy in the cluster. Figure 4.9 is the example of the indication of the sub-segment position resolution of the GRETINA. These position information were used for both addback analysis and Doppler correction. Figure 4.10 shows part of the prompt Doppler corrected γ-ray energy histogram measured for the one-neutron knockout channel from ^{44}S to ^{43}S. The improvement of the peak-to-total ratio is apparent, especially in the higher energy region. In the present work, addback procedure was used for peak identification, γ-γ coincidence analysis within GRETINA or between GRETINA and the IsoTagger array, and analysis final state exclusive momentum distributions that need the clearer spectra. The singles spectrum, on the other hand, was used to deduce the absolute yields of γ-rays due to the more accurate efficiency determination and the lower possibility for accidental summing of unrelated γ-ray hits.

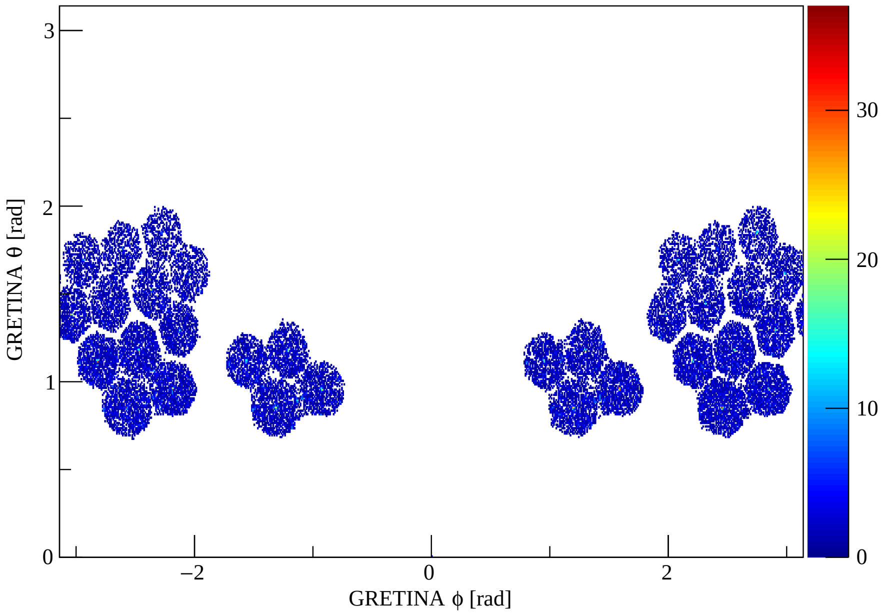

Figure 4.9: Example of the indication of the sub-segment position resolution of GRETINA showing the θ and ϕ angles of γ-ray interaction points.

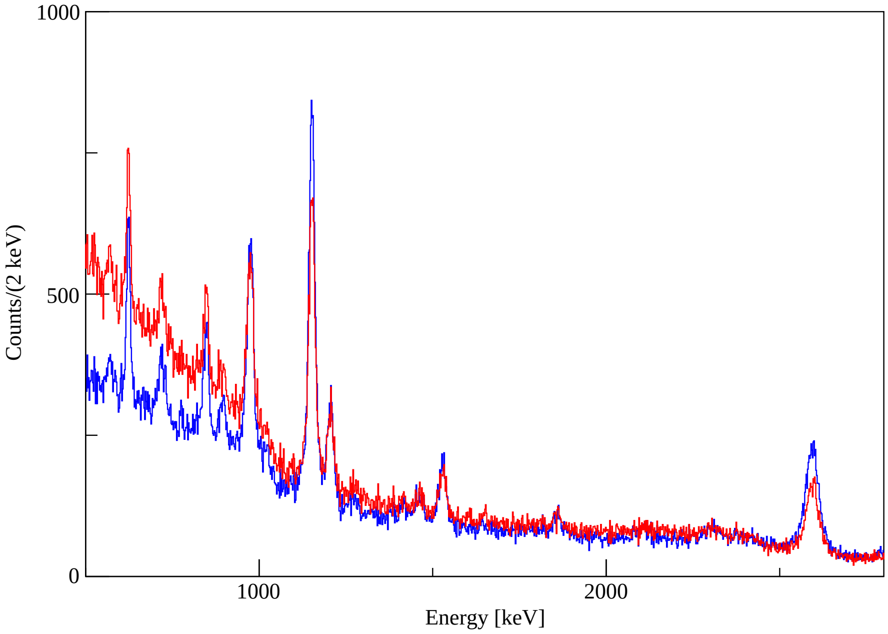

Figure 4.10: Improvement of the peak-to-total ratio of prompt γ-rays with addback procedure of GRETINA. Red and blue spectra correspond to the prompt γ-ray energy histogram of one-neutron knockout channel measured by the GRETINA array before and after the addback procedure adopted in the present work.

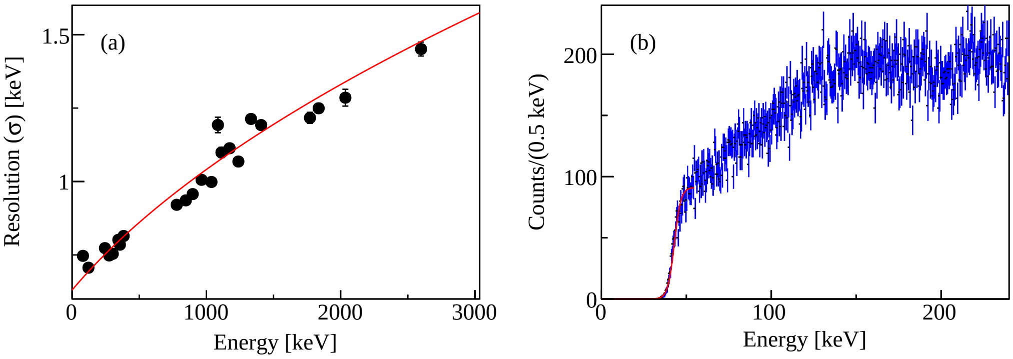

Figure 4.11: Resolution and threshold functions of a single crystal of GRETINA used as the input to the simulation. Peak width of each peak measured with standard radiation sources is plotted in Figure (a) as a function of peak energy. The red line shows the fitting function for the experimental values. Figure (b) shows the low energy region of the γ-ray energy histogram measured with the ^{60}Co source. Fitting function of the threshold is shown as the red line.

4.2.3 Simulation of response function and deduction of efficiency

The prompt γ-ray yields were deduced by fitting simulated response functions to the experimental spectra of ^{43}S. To model the detector response, the resolution of each detector was measured from the calibration runs and used as an input to the simulation. In the Figure 4.11(a) the resolution (peak width, σ) of each peak is plotted as black points against the peak energies of various calibration sources for a single crystal. These experimental points were fitted by a function of energy E individually:

$$\sigma = E_0\sqrt{(1 + E_1 \times E)}. \tag{4.5}$$

Both E_0 and E_1 were deduced for each crystal by fitting to the experimental data.

The lowest known transition in ^{43}S is 185 keV. It will be Dopplershifted down to around 145 keV for angles θ_γ^{LAB} ~120. Furthermore, low energy deposits of Compton scattered γ-rays of higher energy extend down to 0 keV. Therefore the shape of the energy threshold of each crystal is needed as an input to the simulation. Figure 4.11(b) shows the energy spectrum of a single crystal in the low energy region measured with the ^{60}Co source. Threshold of each crystal was modeled by the function below:

$$E_{thresh} = \frac{1}{2}\left\{1 + \tanh\left(\frac{E - E_2}{E_3}\right)\right\}. \tag{4.6}$$

Both E_2 and E_3 were deduced by fitting to the experimental spectrum of each crystal.

The nuclear reaction of interest was simulated simultaneously with the emission and interaction of γ-rays resulting in the identical data set of S800 and GRETINA with the experimental data. The output of the simulation contains the γ-ray interaction points, their coordinates and energy deposits, in addition to the ejectile information a_{ta}, b_{ta}, d_{ta} needed for the Doppler correction. The simulation was performed using the GEANT4 simulation package [102, 103]. HPGe detectors, cryostats, two mounting hemispheres, aluminum beam pipe, and the secondary target or calibration source with its holder were included in the simulation. As the interaction of photons

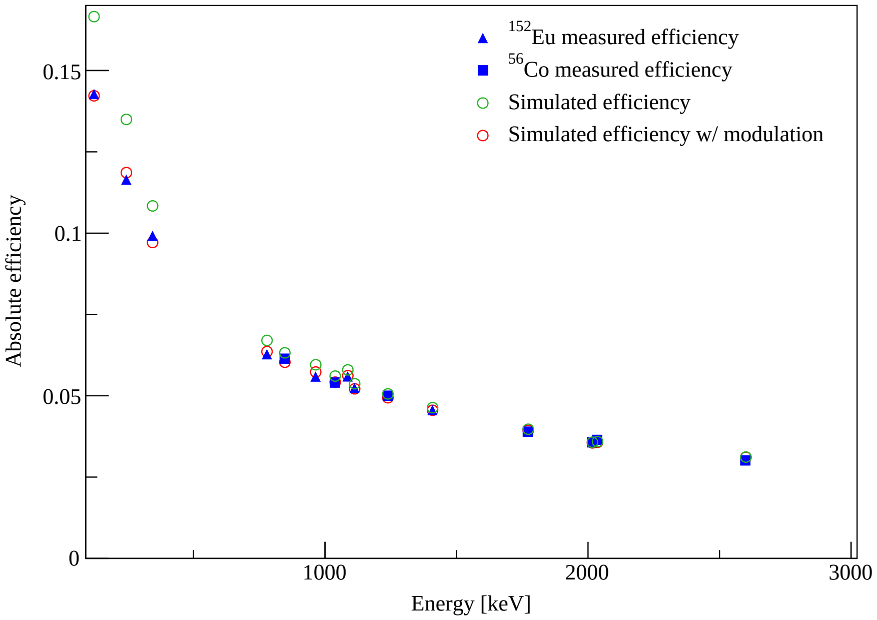

Figure 4.12: Efficiency of GRETINA without addback. Blue filled triangle and square correspond to the measured efficiencies with ^{152}Eu and ^{56}Co sources. Red and green open circles are simulated efficiencies with and without the empirical modulation of efficiencies.

with materials, Compton scattering, Rayleigh scattering, pair production, and photoabsorption were taken into account. Some parameters deduced from experimental measurements were used as the input of the simulation. For the simulation of calibration runs the γ-decay scheme of each source was implemented. For the simulation of the in-beam setting, the incoming beam parameters, its kinetic energy, momentum spread, and spatial distribution on the target were used. In order to model the reaction process, the angular and momentum distribution of the ejectile were matched to the experimentally measured ones. Besides them, stopped γ-rays from HPGe itself or surrounding materials were also simulated to treat the background properly, which will be shown in §4.2.5. The output format of the simulation code is identical to the GRETINA data format of the experimental data. Therefore identical analysis and postprocessing codes as well as settings are used fo avoid mistakes and biases.

One of the specific challenges in the simulation of the GRETINA array is the proper description of the uncertainty of the signal decomposition. Especially multiple interactions in a single segment are very difficult to decompose. It is challenging to distinguish wheather two or more interactions occur in the same segment close to each other or a single interaction occurs at an average point between them. To treat this in the simulation, all interactions in the same segment within the specific distance, called packing radius, were assumed to arise from a single interaction. The energy was set to the sum of individual energies and the interaction point was defined as the energy-weighted average position. In the simulation of the present work, 6 mm was chosen to be the packing radius.

The obtain the γ-ray yield of individual transition, the response function of the GRETINA array was treated as the fixed shape and the only fitting variable is its overall scaling parameter. This parameter of each γ-ray transition was obtained by fitting general response functions together with properly chosen background functions to

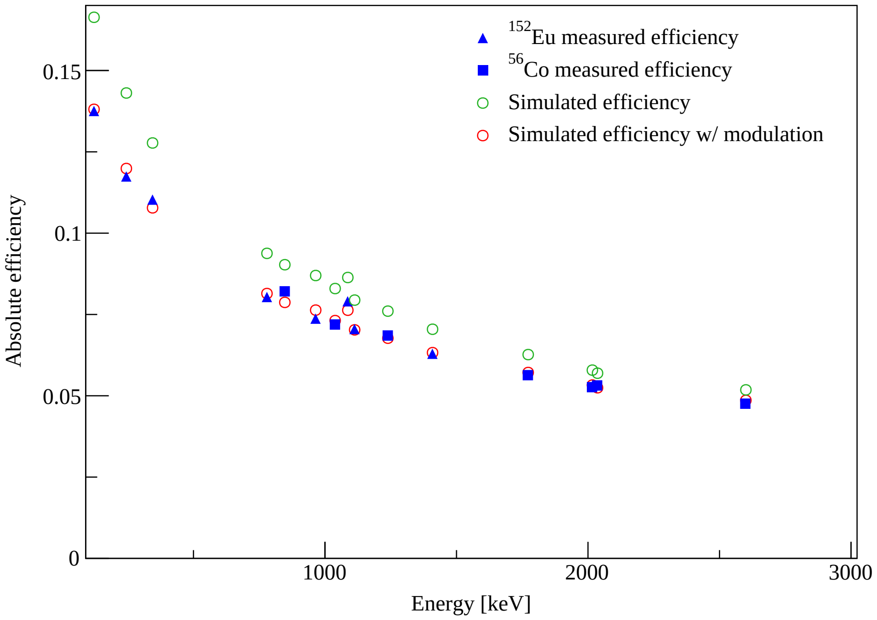

Figure 4.13: Efficiency of GRETINA with addback. The colors and styles of plots are the same as Figure 4.12.

the experimental spectrum after Doppler correction. In this procedure, χ^2 fitting was performed with the MINUIT fitting package [104] implemented in the ROOT analysis framework [105]. The intensities of the γ-rays were then obtained by multiplying the fitting parameters with the total emitted γ-ray in the simulation.

Because the absolute numbers of γ-rays emitted from the nuclei of interest are deduced from the fitting with the simulated response function, the accuracy of the simulation is directly related to the uncertainty for the γ-ray emission yield. To evaluate the accuracy of the simulation, the absolute efficiency of the GRETINA array was measured and compared to the simulated value. For this purpose, two calibration sources of ^{152}Eu and ^{56}Co were used to cover the energy range of expected γ-rays. The activity of the ^{152}Eu source was known as 46.0(7) kBq at the time of the experiment but that of the ^{56}Co source was not well known. To solve this situation, observed intensities of γ-rays from the ^{56}Co source were scaled to match those from ^{152}Eu in the range from 1.0 to 1.5 MeV. Figure 4.12 and 4.13 show the absolute efficiencies without and with addback procedure. Note that in these figures the efficiency of GRETINA is defined as the ratio of the number of counts in the full energy peak deduced by the gaussian fitting to the spectrum and that of the total emission of the specific transition during the measurement or in the simulation.

In Figure 4.12, it can be seen that the simulation overestimates the efficiency, especially below 500 keV. By the previous works [67], it was found that this discrepancy could not be due to inaccuracies in the treatment of the γ-ray absorption at low energy in the simulation. Another potential source of this discrepancy is an inefficiency of the decomposition procedure in this energy region. Low-energy γ-rays produce only weak signals in the segments of GRETINA, which may not be over the segment thresholds. This causes an event without any segment information but central contact, which will fail in the decomposition procedure. Even if the segment was triggered, the weak pulse will be relatively noisy and difficult for the decomposition algorithm to handle, leading to the poor energy and position information by fitting. In both cases, and possibly others, these events may not make it through the data stream to be recorded.

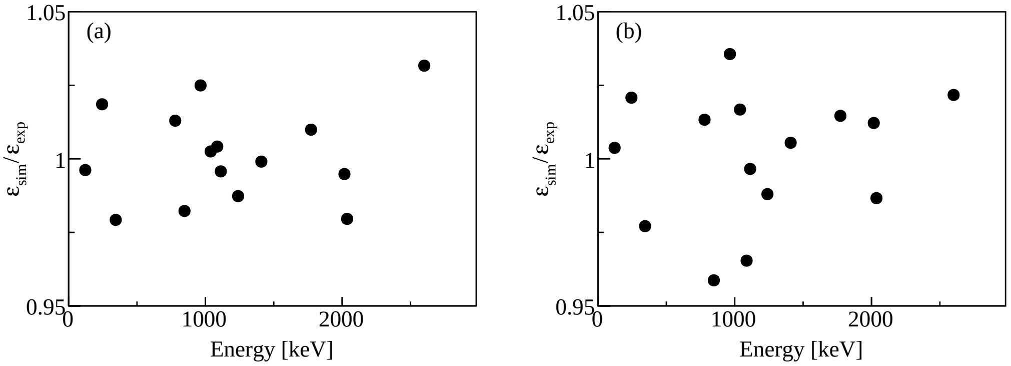

Figure 4.14: Ratio of simulated and measured efficiencies of GRETINA. Figure (a) and (b) are the plots without and with addback.

This additional inefficiency was accounted for by adding a modulating function into the simulation. The ratio of the efficiency measured with the standard sources and that of the simulation was modeled as below:

$$\frac{\varepsilon_{exp}}{\varepsilon_{sim}} = \frac{1}{1 + \exp(A + B \times E_\gamma)}. \tag{4.7}$$

A fraction of low energy events were then removed according to this function to reproduce the experimental efficiency. The result of this procedure is also present in Figure 4.12 and 4.13 and the simulation shows good agreement with the experimentally measured efficiency. Figure 4.14 shows the ratio of the simulated efficiency with this empirical modulation and the experimentally measured efficiency. From this, uncertainties of 2.5% and 5% for the efficiencies without and with addback analysis, respectively, are used as an estimate of the uncertainty of the γ-ray emission yield.

4.2.4 Doppler correction

In a typical in-beam experiment, prompt γ-rays were emitted in flight from excited states of reaction residues moving at the velocity around $\beta \sim 0.4$. In this situation, γ-ray energies measured by detectors in the laboratory frame are shifted from those in the rest frame of the reaction residues by the Doppler effect:

$$E_\gamma = \frac{1 - \beta \cos \theta_\gamma^{LAB}}{\sqrt{1-\beta^2}} E_\gamma^{LAB}. \tag{4.8}$$

To compensate this effect, Doppler correction was performed through measuring E_γ^{LAB}, β, and θ_γ^{LAB} event-by-event. The velocity of the reaction residue at the moment of the γ-ray emission was deduced by using the d_{ta} value and Equation (4.12). In Equation (4.12), γ_0 was defined as the relativistic value for the particle on the central trajectory of the S800 spectrograph. For the Doppler correction, however, γ_0, and the corresponding β_0 were chosen to align a chosen peak at forward and backward emission angles and minimize its width. In deducing β_0, the 2600 keV γ-ray from ^{43}S in the one-neutron knockout setting was used, because the partial life time, τ, of this transition should be the shortest compared to other γ transitions due to the relation of $\tau \propto 1/(E_\gamma)^{2l+1}$ for a transition multipolarity of l. The resulting β_0 was 0.418. In the one-neutron knockout setting, the magnetic rigidity of the S800 spectrograph was set to 3.645 Tm. By taking into account the energy loss in the half thickness of the

^{9}Be secondary target, the mean velocity of ^{43}S can be estimated as 0.415, which is a good agreement with β_0 deduced above.

The γ-ray emission angle with respect to the particle trajectory, θ_γ^{LAB}, can be deduced if the origin of γ-ray emission and the first interaction point in the detector were known. The γ-ray emission was assumed to be at the target center, especially the z position of the target was just on the designed value of the optical transfer matrix. As described in §3.4.1, γ-ray interaction points were obtained with the subsegment position resolution. Because this position resolution was the same amount as the offset of detector mounting, the whole GRETINA array was rotated around the target position in dispersive and non-dispersive direction. The rotation angles where the width of the 2600 keV transition was minimized were deduced in the same manner as β_0 and resulting values of $\Delta a = 15.9$ and $\Delta b = 7.3$ mrad were used in the further analysis.

Finally the error of E_γ was estimated by corresponding uncertainties on E_γ^{LAB}, β, and θ_γ^{LAB}. As was shown in Figure 4.8, the uncertainty of the energy recalibration was estimated smaller than 0.5 keV. The central β for Doppler correction was also estimated above. This β_0 can be attributed as the mean of the velocity at the moment of the reaction, reasonably assumed at the target center. By taking into account the energy loss in the target, the value of β at the time of emission can range from 0.430 to 0.403, at the upstream and downstream edge of the target, respectively. The reaction can occur at any position along the target, so the distribution of β can be assumed as the uniform distribution. Thus, the uncertainty of the β can be calculated as $(0.430 - 0.403)/\sqrt{12} = 0.0076$ as 1σ. This results in an uncertainty of 3 keV for 2600 keV transition after Doppler correction.

The largest component of the uncertainty of θ_γ^{LAB} can be attributed as the offset of the target position with respect to the center of GRETINA. In the present analysis, the secondary target was assumed to be just on the designed position of the optics, but the real position can be estimated by the same manner deducing β_0. By changing the z position of the secondary target for the Doppler correction, the peak width of the 2600 keV peak was evaluated and it was minimized when the target was moved 2.5 mm upstream. If this target position and previously deduced β_0 were used for the Doppler correction, the peak center of the 2600 keV shifted to 2606 keV. This energy difference was taken as the uncertainty due to the z position offset.

As the result, the uncertainty of the γ-ray energy deduction for 2600 keV transition was estimated as 2600(7) keV. These procedures were applied to all the prompt γ-rays. The γ-ray energy uncertainty shown in the final result will be the quadratic sum of these systematic uncertainty and errors due to fitting procedure.

4.2.5 Treatment of background

The HPGe detector is sensitive not only to γ-rays from reaction residues but also to those from the detector itself or surrounding materials. Figure 4.15 shows the two dimensional histogram of the γ-ray energy in the laboratory frame and γ-ray timing for the one-neutron knockout setting. γ-ray timing was defined as the timing difference from the signal of the E1 scintillator. In Figure 4.15, the structure around -50 corresponds to the arrival of the secondary beam, i. e. prompt γ-rays. A significant delayed component around 700 keV is visible, but other stopped γ-rays with narrow widths are also present in the prompt region. Therefore a prompt timing gate is not sufficient to reject this background. In order to account for the background in the analysis, monoenergetic γ-rays in the laboratory frame were simulated and Doppler

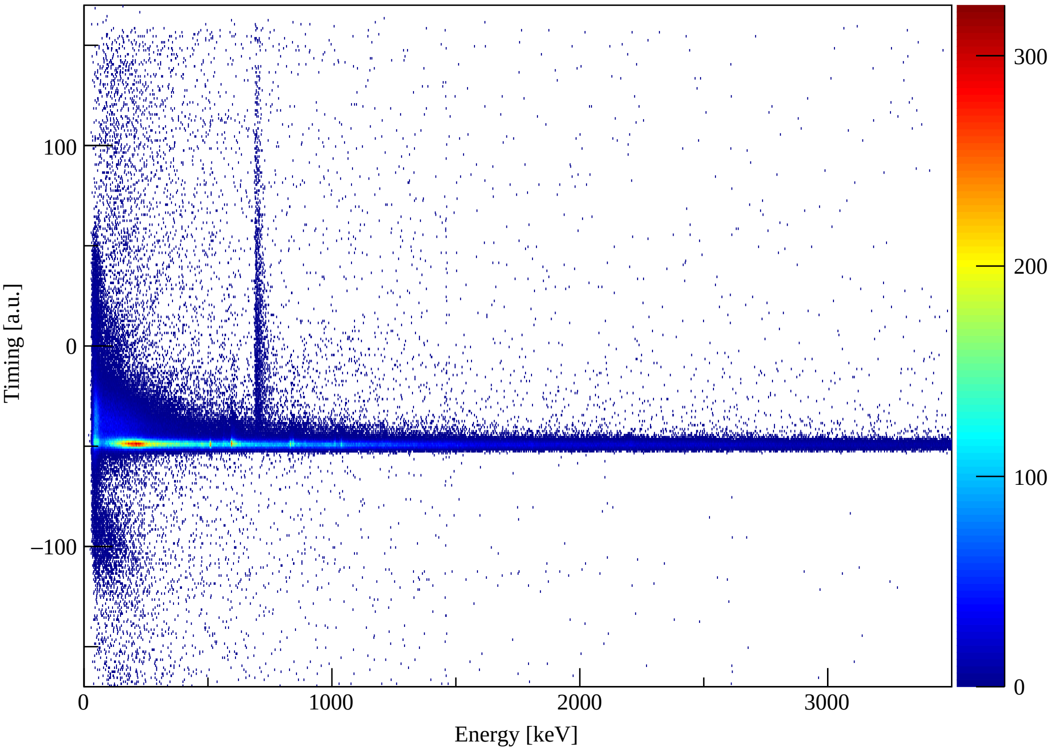

Figure 4.15: Two dimensional plot of γ-ray energies and measured timings in GRETINA for the one-neutron knockout setting. γ-ray energies are plotted in 2 keV bin.

correction was applied to these stopped γ-rays with randomly simulated particle trajectory in the S800 spectrograph. Figure 4.16 shows the γ-ray energy histogram in the laboratory frame for the one-neutron knockout setting, which is the same as the projection of Figure 4.15 onto the X axis. Visible peaks are attributed to reactions induced by neutrons in the Ge detector material or the Al beam pipe listed in Table 4.2. Simulated γ-ray counts were scaled by the peak counts in Figure 4.16. Some peaks have high-energy tail which comes from the recoil energy of the excited germanium nucleus. In the present analysis, this tail was not simulated, but rather treated as part of the monoenergetic peak and the simulated peak counts were scaled by the total counts including the high-energy tail (shown by the hatched in Figure 4.16). Other peaks were scaled assuming the gaussian shape. All the scaled peaks after Doppler correction were just treated as the fixed background and there was no additional fitting parameter related to this analysis.

4.3 Analysis for IsoTagger

In the same manner as for the GRETINA array, the energy calibration was performed for the IsoTagger array. To deduce the decay curve of the isomeric state of ^{43}S, the timing calibration of the whole array was also done (§4.3.2). Finally the simulation of the response function of the array and estimation of the uncertainty on the efficiency is described in §4.3.3 with the specific treatment for γ decays with relatively long life time.

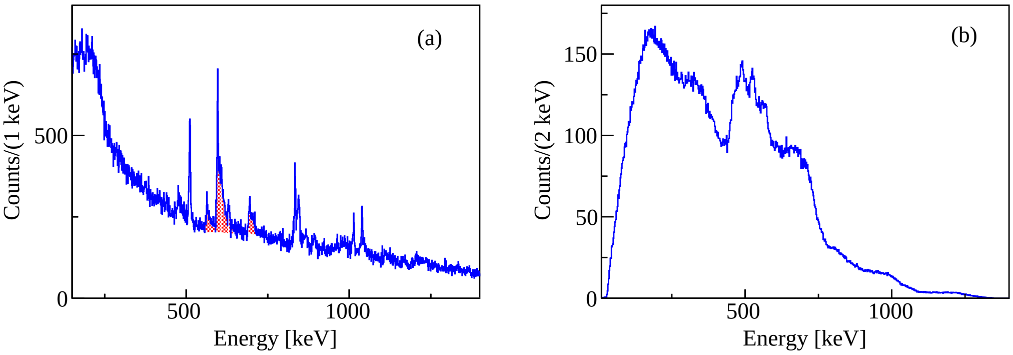

Figure 4.16: (a) γ-ray energy histogram of GRETINA before Doppler correction for the one-neutron knockout settings. Note that this histogram corresponds to the projection of Figure 4.15 onto the X axis. Some peaks have asymmetric peak shapes but treated as symmetrically shaped and scaled to the counts in hatched area in estimating background. See text for details. (b) Simulated background γ-rays related to the reaction with neutrons after Doppler correction.

Table 4.2: Observed background γ-rays related to the reaction with neutrons.

Energy [keV]	Origin	Half life
567	^{76}Ge$(n,n'\gamma)$	
600	^{74}Ge$(n,n'\gamma)$, ^{73}Ge(n,γ)	
691	^{72}Ge$(n,n'\gamma)$	420 ns
835	^{72}Ge$(n,n'\gamma)$	
842	^{27}Al$(n,n'\gamma)$	
1013	^{27}Al$(n,n'\gamma)$	
1040	^{70}Ge$(n,n'\gamma)$	

4.3.1 Energy calibration

The energy calibration of the IsoTagger array was performed in a very similar way as that of the GRETINA array. The standard sources of ^{22}Na, ^{57}Co, ^{88}Y, and ^{133}Ba were used and the linear function was fitted as the calibration function for each crystal. In this experiment, however, the precise measurement of the γ-ray energies is a secondary objective, because the energy of the decay from the isomeric state has been previously reported [22, 29]. However, a precise analysis of the coincidence between the IsoTagger and GRETINA and the accuracy of extracting the γ-ray yield from the isomeric state are of importance. For this purpose, after the energy calibration with sources of each crystal has been done, the offset value of the linear calibration function was adjusted to align the γ-ray from the isomeric state of ^{43}S to 320 keV. This is done to account for shifts in the gain occurring during the measurement time, for example due to the magnetic fields and temperature changes. The result of this calibration procedure for each crystal is shown in Figure 4.17.

---

[1] β^+ branching ratio is 90.326(15)% [106].

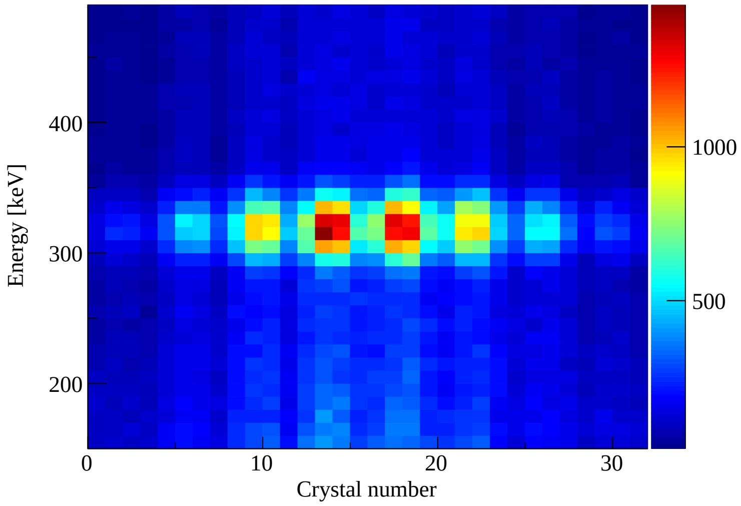

Figure 4.17: Result of energy calibration of IsoTagger in the one-neutron knockout setting. After calibration using standard radiation sources, offset of each crystal was adjusted to align 320 keV isomeric transition in ^{43}S. γ-ray energy is plotted in 10 keV bin

Table 4.3: Standard radiation sources used for the calibration of the IsoTagger. Values are taken from [101, 106].

Nuclide	Half life	Activity	Energy [keV]	Intensity per decay [%]
^{22}Na	2.6019y	187 kBq	510.999	180.76(4)[1]
			1274.537(7)	99.935(15)
^{57}Co	271.79d		122.06065(12)	85.60(17)
^{88}Y	106.65d	17.3 kBq	898.036(4)	94.0(3)
			1836.052(13)	99.36(3)
^{133}Ba	10.52y		356.0134(6)	61.94(14)

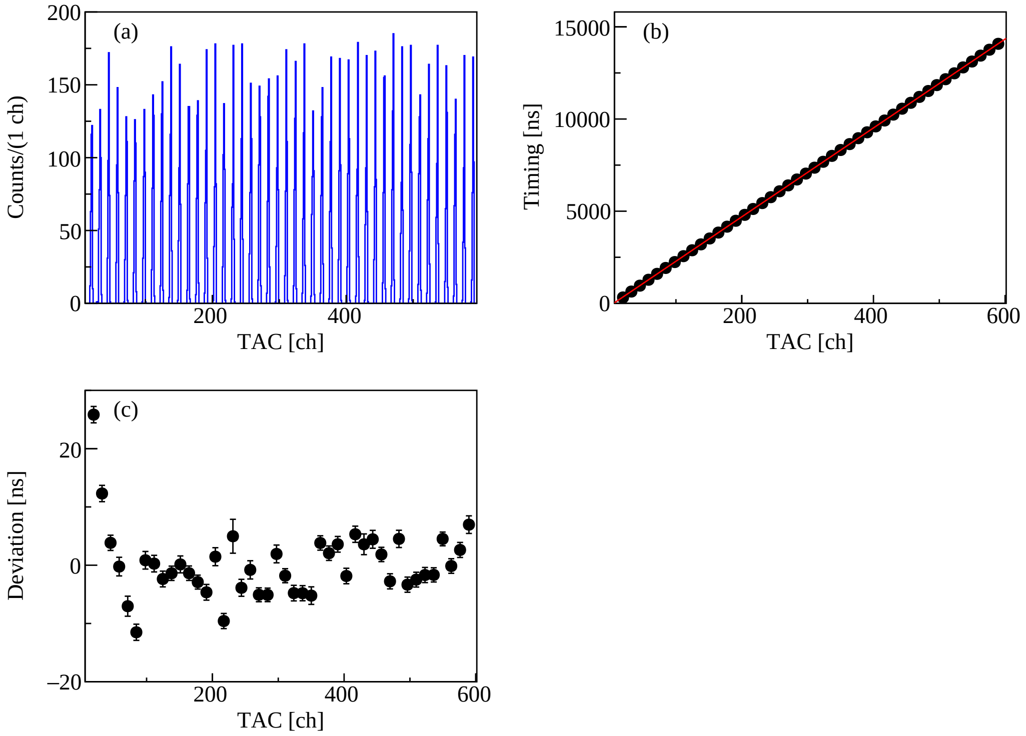

Figure 4.18: Result of timing calibration of IsoTagger. Figure (a) shows the spectrum of time calibrator measured by TAC. The linear relation of measured TAC ch and real time of each peak is shown in (b). The red line is the fitted linear function and used for the timing calibration. Figure (c) shows the deviation of measured timing after calibration and the real timing of the calibrator.

4.3.2 Timing calibration

Besides the energy of the γ-ray from the isomeric state of ^{43}S, its lifetime has also been reported previously. But the reported values from a few groups are scattered [22, 29, 30]. Therefore an independent measurement of the lifetime from the present experiment is desired. For this purpose, a timing calibration of the TAC module output was performed prior to the in-beam measurement. Figure 4.18 (a) shows the histogram of the time calibrator giving pulses with fixed, known time difference measured by the TAC module. Each peak was fitted by a Gaussian function to determine the mean. The relationship of the deduced peak channels and the real timing was fitted using a linear function as shown in Figure 4.18 (b). From Figure 4.18 (c), the uncertainty of the IsoTagger timing due to the calibration was deduced as 6 ns as the root-mean-square value of the deviation of the calibrated timing from the real timing of the calibrator.

4.3.3 Simulation of response function and deduction of efficiency

The energy and yield of the isomer decay was deduced by fitting the simulated response function of the whole array to the measured γ-ray energy histogram. The simulation of the response of the IsoTagger was performed by using the GEANT4 software [91, 102]. Not only the 32 CsI(Na) crystals and the Al stopper plate, but also the surrounding stainless steel vacuum chamber were implemented. The thickness of the Al stopper

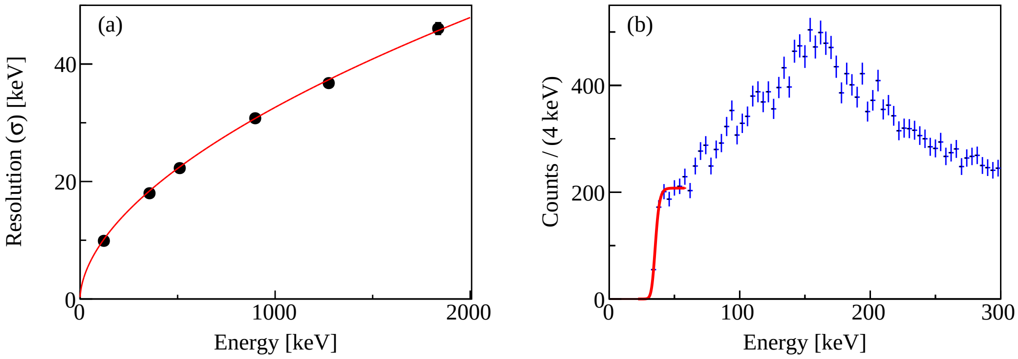

Figure 4.19: Resolution and threshold functions of each crystal of IsoTagger used as the input of the simulation of whole array like Figure 4.11. Peak width of each peak measured with standard radiation sources is plotted in Figure (a) as the resolution of each crystal against the corresponding peak energy. Red line shows the fitting function of experimental values. Figure (b) shows the low energy region of the γ-ray energy histogram of a single crystal measured with the ^{22}Na source. Fitting function of the threshold is shown as the red line.

and the distance between the stopper and the CsI crystals were measured during the experiment and used as the input parameters of the simulation. Combining the geometry and the placement of each crystals, the efficiency of the whole detector is simulated properly. To reproduce the response of each crystal precisely, resolution function against γ-ray energy and threshold of each detector measured with standard sources were used as the input of the simulation, which are shown in Figure 4.19.

The procedure is very similar to the one for GRETINA as described in §4.3.2, but there are some differences due to the different detection methods. To reconstruct the experimental situation, the xy position distribution of ^{43}S on the Al stopper produced in the one-neutron knockout reaction was extrapolated from the trajectory measured by the two CRDCs. In the simulation then event-by-event a random position from the xy distribution is chosen as the γ-ray emission point. The z coordinate of the isomeric decay, implantation depth of ^{43}S in the Al plate, was estimated by the ATIMA code [107] build in the LISE++ software [108] using the experimentally measured average energy of the ^{43}S ions.

There is also a difference in how the γ-ray yield is determined experimentally. The number of the γ-rays emitted after the implantation to the stopper was deduced by the fitting of the simulated response function to the γ-ray energy spectrum, the same manner as the GRETINA, but because the lifetime of the isomeric state is on the same order as the flight time from the secondary target to the Al stopper, a significant amount of nuclei produced in an isomeric state by the one-neutron knockout reaction decayed in-flight. The half life of the isomeric state at 320 keV of ^{43}S was previously measured as 415(5) ns [29] and also deduced from the present experiment as 377(4) ns, which will be described in §5.2. Considering the flight length in the S800 was 15.339 m and the velocity of ^{43}S just after the secondary target was deduced as $\beta = 0.400$ from the magnetic rigidity of the S800, 79.4% of the isomers survived and arrived at the stopper prior to the decaying. This value should be considered to correct the number of counts determined from the simulation fit to obtain the primary population of the isomer. To estimate the systematic error of this ratio, the same value using the

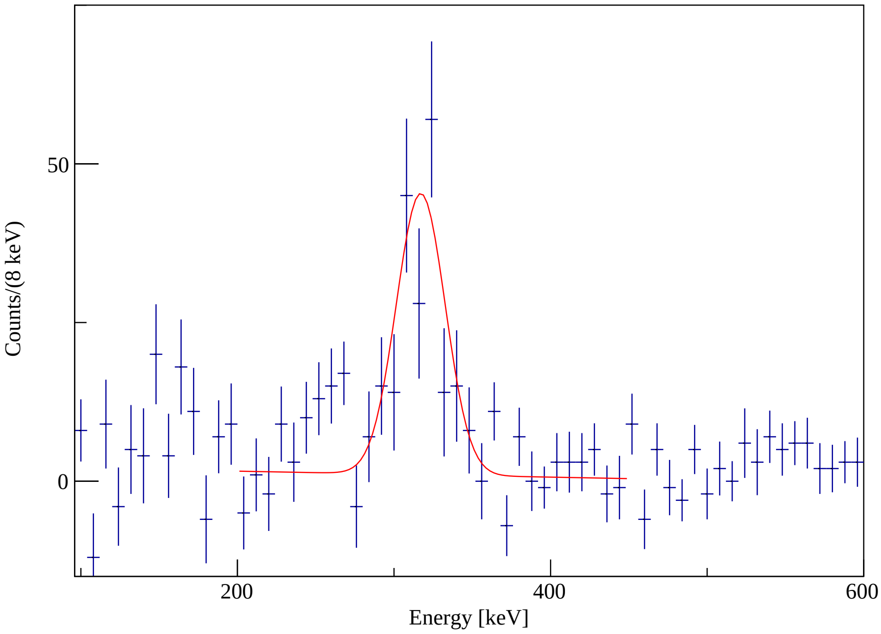

Figure 4.20: Efficiency deduction for the 320 keV isomeric transition. Blue points are the γ-ray energy histogram of one-neutron knockout channel measured by the IsoTagger array with the gate on the 1532 keV prompt transition measured by the GRETINA array. The red line is the gaussian fitting to the experimental spectrum.

previously measured half life of ^{43}S isomer was calculated as 0.812(2). Also the ToF distribution between the secondary target and the Al stopper can affect on this ratio. The ToF distribution was estimated by LISE++ [108] considering the momentum width upstream of the secondary target resulting in a width of 4 ns with the central ToF of 125 ns. This ToF spread corresponds to about 1% uncertainty on the survival ratio. By taking quadratic sum of the error of survival ratio due to the difference from the previous life time measurement and ToF spread in this experiment, the ratio was estimated as 0.794(23).

To confirm the accuracy of the simulated response function and estimate the uncertainty on the γ-ray detection efficiency, source runs with ^{88}Y and ^{22}Na sources were measured. Note that ^{22}Na source emits 1275 and 511 keV γ-rays with intensities per decay of 99.9 and 180%, respectively. Due to the different setting of DAQ system for the source measurement and the high activity of the sources, which caused a large DAQ dead time [2], the absolute efficiency value cannot be determined from the singles γ-ray energy spectrum. Because of this problem, the efficiency was determined using the γ-γ coincidence analysis within the IsoTagger array. By subtracting the self-coincidence, that should not appear in the decays of ^{88}Y and ^{22}Na, using the intensity ratio of two γ-ray peaks deduced from the singles spectrum, the efficiencies at four γ-ray energies are deduced as shown in Figure 4.21.

As will be shown in §5.2, a prompt γ-ray at 1532 keV was found to be coincident with the 320 keV delayed γ-ray for the first time in this work. Once this coincidence was confirmed, the efficiency for the 320 keV delayed γ-ray can be directly estimated by using this 1532→320 keV cascade. Figure 4.20 shows the delayed γ-ray energy histogram with a gate on the 1532 keV prompt γ-ray in the GRETINA. By taking

---

[2] this is also evidenced by the large number of self coincidences observed

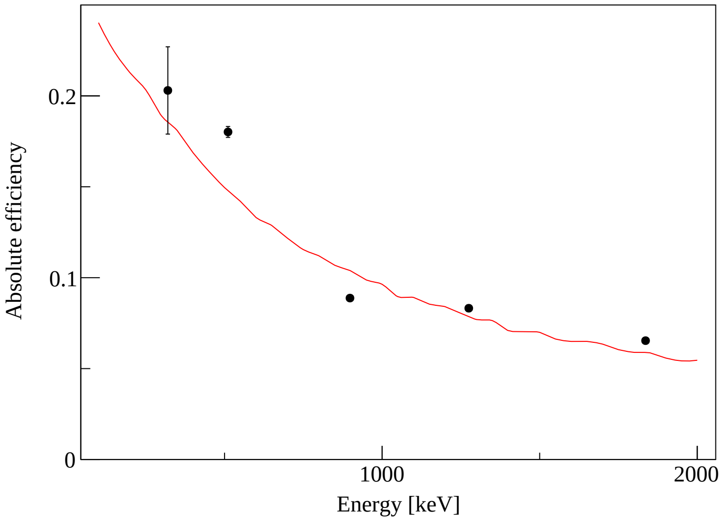

Figure 4.21: Efficiency of whole IsoTagger array. Red line shows the simulated values and black points are measured values. Points are measured efficiency with ^{43}S reaction residue of one-neutron knockout, ^{88}Y, and ^{22}Na standard radiation sources.

the peak count of this coincident 320 keV γ-ray and 1532 keV prompt peak in the GRETINA by assuming the Gaussian shape for both of them, and the survival ratio of this isomeric state estimated above, the efficiency of this isomer decay was deduced as 20.3(24)%, which is also plotted in Figure 4.21.

For the estimation of the uncertainty of the simulated efficiency, the effect of the implantation depth was evaluated. The mean implantation depth distribution was estimated by using the measured energy distribution of ^{43}S. By calculating the stopping range with LISE++ [107, 108] and taking 1σ width of the energy distribution, the implantation depth amounts to 2.96 mm with a σ of 0.21 mm. This range result in a 2% uncertainty on the efficiency at 320 keV. By taking the quadratic sum of this value and the difference of the simulation and the experimentally deduced efficiency at 320 keV using the cascade decay, the uncertainty was estimated to be 20.3(27)%.

4.4 Analysis on momentum distribution

As was described in §3.3.1, the kinetic energy of the reaction residue was deduced as the difference from the energy of the central trajectory of the spectrometer, $d_{ta} = \Delta E/E$. To deduce the parallel component along the beam axis of the momentum of the outgoing particle in the lab frame and compare the theoretical parallel momentum distribution with the experimental one, following calculation procedure was performed.

Prior to the further calculation, the product of the velocity and the relativistic parameter of the reaction residue was calculated from the magnetic rigidity of the S800 spectrometer:

$$\gamma\beta = \frac{P}{M} = \frac{B\rho Ze}{M} \approx \frac{Z}{A} \cdot \frac{B\rho}{3.10715 \text{ Tm}}, \tag{4.9}$$

where the approximation of $M \approx A \times 931.502$ MeV is applied. The relativistic factor of the central trajectory of the S800 spectrometer is then deduced as

$$\gamma_0 = \sqrt{1 + (\gamma_0\beta_0)^2} = \sqrt{1 + \left(\frac{B\rho_0 Ze}{M}\right)^2}. \tag{4.10}$$

As the kinetic energy is denoted as $E - M$, the definition of d_{ta} leads to

$$d_{ta} = \frac{(E - M) - (E_0 - M)}{E_0 - M} = \frac{\gamma - \gamma_0}{\gamma_0 - 1}. \tag{4.11}$$

Therefore,

$$\gamma = \gamma_0 + (\gamma_0 - 1)d_{ta}, \tag{4.12}$$

and

$$E - M = \{\gamma_0 + (\gamma_0 - 1)d_{ta} - 1\}\, M \tag{4.13}$$

can be obtained. Considering the magnitude of the total momentum is $P = \gamma\beta M = \sqrt{\gamma^2 - 1}M$ and using the approximation of $\gamma^2 \approx \gamma_0^2 + 2\gamma_0(\gamma_0 - 1)d_{ta}$, because $\gamma \approx 1$ and $d_{ta} \lesssim 0.05$,

$$\frac{P}{P_0} = \sqrt{\frac{\gamma^2 - 1}{\gamma_0^2 - 1}} \approx 1 + \frac{\gamma_0}{\gamma_0 + 1} d_{ta} \tag{4.14}$$

is calculated event by event. Finally, the direction of the momentum vector is deduced by

$$\hat{P} = (\sin\theta\cos\phi,\ \sin\theta\sin\phi,\ \cos\theta), \tag{4.15}$$

where

$$\sin\theta = \sqrt{\sin^2 a_{ta} + \sin^2 b_{ta}} \tag{4.16}$$

and

$$\tan\phi = \frac{\sin b_{ta}}{\sin a_{ta}}. \tag{4.17}$$

As mentioned in §3.3.1, the coordinates of the reaction residue trajectory and its energy difference at the secondary target position $(d_{ta}, y_{ta}, a_{ta}, b_{ta})$ are deduced by the coordinates measured at the focal plane $(x_{fp}, y_{fp}, a_{fp}, b_{fp})$ and the transfer matrix between them. During the beam time, the currents in the magnets of the S800 were measured. By using these currents values, the magnetic fields and the resulting transfer matrix of up to the sixth order of the whole spectrograph are simulated [97].

The experimental parallel momentum distribution, $P_{//}$, deduced as above is then compared with a theoretically calculated one using the eikonal reaction theory, see §2.3.6. The distribution was calculated in the rest frame of the projectile. To directly compare the experimental data and the theoretical calculation, two treatments were applied to the calculated distribution: transformation from the center of mass frame to the lab frame and convolution with experimental momentum resolution.

For the convolution with the experimental resolution, the momentum of the unreacted ^{44}S was measured by centering the S800 rigidity to the outgoing ^{44}S. The $P_{//}$ after the correction with PPAC x position at II, described in §3.3.1, was modeled as the gaussian distribution and its width was used for the convolution. The experimental result will be shown in §4.4.

After the convolution, the calculated distribution was scaled by the γ factor to account for the broadening due to the Lorentz boost. Note that value of γ was corresponding to the S800 magnetic rigidity setting in this calculation. This treatment is valid because the change of calculated distribution due to the depth of the reaction point within the secondary target, or the beam energy at the moment of one-neutron knockout, is negligibly small. Thus the direct comparison with the momentum measured in the S800 is possible. This treatment also relies on the fact that the difference of the energy loss per nucleon in the secondary target with the change of neutron number is quite small. Then the calculated distribution was shifted using the peak position of the gaussian of unreacted ^{44}S distribution, which corresponds to the Lorentz boost between the two reference frames. Note that the momentum shift was not performed by directly using the momentum center of unreacted ^{44}S, $P_{//}^{44\text{S}}$, but by using scaled $A/(A-1) \times P_{//}^{44\text{S}}$ distribution assuming the momentum per nucleon was approximately conserved in the one-neutron knockout reaction.

The amplitude of the resulting theoretical distribution was then scaled to the integral of the experimental counts for each state, leaving no free parameters for fitting. Because of a tail on the lower momentum side, which is not reproduced in the calculation, the integral of the experimental counts was restricted to just after the center of the distribution to cut the lower momentum region.

The theoretical distribution reflects the direct population to the specific state of ^{43}S. From the experimental setup of this thesis work, however, distributions coincident with prompt or delayed γ-rays or one of inclusive channel without any gate on γ-rays were only achieved. To extract the distribution of an excited state, the distribution coincident with γ-rays decaying from this state was subtracted with those coincident with γ-rays feeding to this state. Note that the efficiencies of γ-ray detectors were taken into account for this procedure. For deducing the distribution of directly populating the ground state, all the feeding transition were subtracted from that of inclusive channel.

In the momentum reconstruction analysis described above, the profile of incoming beam is not used at all. The incoming beam had the finite spot size, however, making the resolution of d_{ta} as the convolution of the finite x_{ta} distribution. To improve this situation, two PPACs were placed upstream of the secondary target.

In the ideal situation, two dimensional positions and angles in both dispersive and non-dispersive directions can be deduced and correlations with d_{ta} were investigated to achieve the best d_{ta} resolution. In the present experiment, the x layer of one PPAC did not work properly. So only one x position was used for the correction of d_{ta}, which had a dominant effect on the d_{ta} resolution, and the other position and angles were not used for the correction. Figure 4.22 shows the measured maximum charge value of each strip in the x layer of the PPAC used in the analysis. Note that some pads did not worked properly or were removed in the analysis due to noise. Because the secondary beam setting of the present experiment was almost 100% pure ^{44}S, as will be shown in §5.1, the gain matching calibration using a few isotopes with different Z numbers like the calibration for CRDC detectors was not possible. This figure confirms that the gain of each pad has been sufficiently matched even without further calibration and that the PPAC x position could be deduced from the geometrical center of the charge distribution, see Equation (4.1).

Figure 4.23 shows the two dimensional of d_{ta} and PPAC x position measured with the spectrograph set to ^{44}S. The correction for d_{ta} was performed by the equation below:

$$d_{ta}' = d_{ta} - C \times x_{PPAC}. \tag{4.18}$$

The correction parameter C was chosen to achieve the best resolution of d_{ta}'. The deduction of this correction parameter is the same manner as the correction on the ToF value, described in §4.1.2. Figure 4.23 (a) and (b) show the plots before and after this correction, respectively, in the unreacted setting. The deduced correction

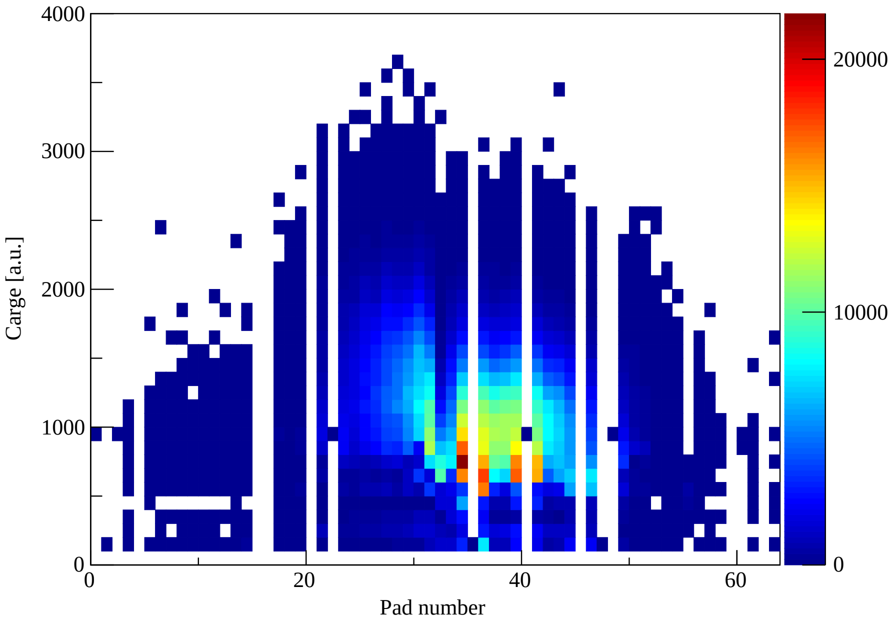

Figure 4.22: Measured charge value in PPAC. This spectrum is measured in the layer stripped in x direction and taken from a single run in unreacted setting. X axis is the pad number of PPAC and Y axis is the maximum charge value in a single event.

parameter was $C = 0.0670$ and this value was used in the following analysis of the one-neutron knockout setting. Figure 4.24 shows the result of this correction for the unreacted setting data, (a) and (b), and the one-neutron knockout setting data, (c) and (d). Figure (a) and (c) are the corrections of the d_{ta} values and (b) and (d) are the corresponding parallel momentum distributions, $P_{//}$, deduced from d_{ta} or $d_{ta}{}'$, as described in this section. In all the figures, red and blue histograms are before and after the correction, respectively. Note that red and blue curves of Figure 4.24 (a) correspond to the projection of Figure 4.23 (a) and (b) to the Y axis. By assuming the gaussian shape for the $P_{//}$ spectrum of the unreacted setting data, the resolution after the correction was deduced to be 0.052 GeV/c, which was used as the width for the convolution of the theoretical distributions.

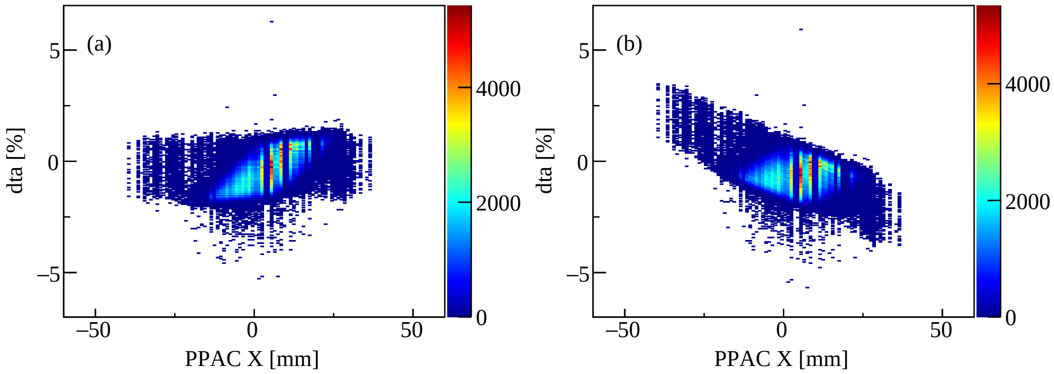

Figure 4.23: Correction on d_{ta} with regard to the PPAC x position. Figure (a) and (b) shows before and after the correction, respectively. This correction was done by using unreacted setting data.

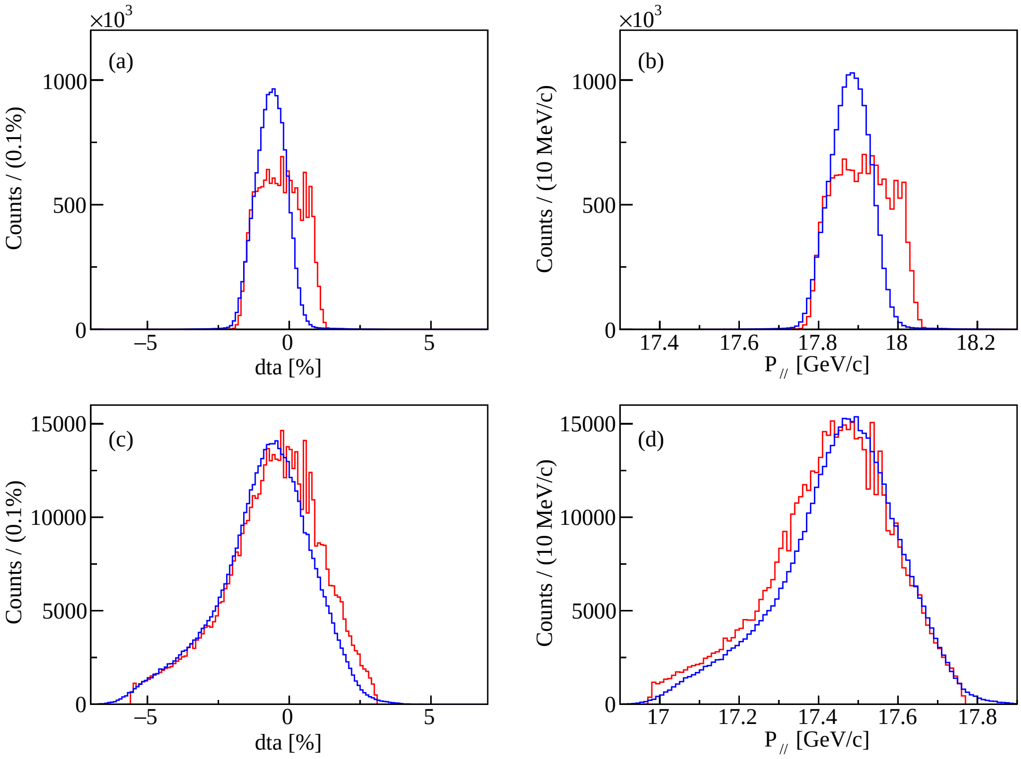

Figure 4.24: Correction of d_{ta} and $P_{//}$ by the PPAC x position for unreacted and one-neutron knockout settings. Figure (a) and (b) are data for unreacted, and (c) and (d) are for one-neutron knockout setting. Figure (a) and (c) are correction on d_{ta}, and (b) and (d) are on $P_{//}$. In all the panels, the red and blue histograms correspond to before and after correction. Note that Figure (a) corresponds to the projection of Figure 4.23 onto the y axis

Chapter 5

Results

In this chapter, the main results of this thesis work and the related analysis are described. Prior to the further analysis, the particle identification for both upstream and downstream of the secondary target will be shown in §5.1. By using gates on them, the energy spectra of prompt and delayed γ-rays and their coincidence histograms are investigated in §5.2. Considering the decay scheme of the excited states of ^{43}S, the parallel momentum distributions coincident with γ-rays and the one for the ground state will be analyzed in §5.3. In §5.4, the production cross section of each state populated in the on one-neutron knockout reaction from ^{44}S to ^{43}S will be shown.

5.1 Particle identification

Figure 5.1 shows (a) incoming and (b) outgoing PID plots for the one-neutron knockout setting, respectively. In the panel (b), a gate was applied to select incoming ^{44}S. Black short-dashed lines in these panels are the gates on incoming ^{44}S and outgoing ^{43}S, respectively. By using these plots, one-neutron knockout channel was unambiguously selected for the further analysis of γ-rays and parallel momentum distributions.

In the present experiment, the number of incoming ^{44}S particles was counted by the scaler value of the OBJ scintillator multiplied by the purity of ^{44}S in the secondary beam. To measure the purity of ^{44}S, the data was accumulated with unreacted setting where the magnetic rigidity was centered on ^{44}S. Figure 5.2 (a) shows the incoming PID plot for the unreacted setting. Note that an additional gate that the data acquisition was triggered by the E1 scintillator was also required in this figure. The black short-dashed line is the gate on the incoming ^{44}S used for the unreacted setting data. The purity of ^{44}S in the secondary beam was deduced as the ratio of the count in this gate and the total count of the incoming PID plot. For the error estimation of the purity, two components were considered. The first component was the statistical uncertainty of ^{44}S, which was only a small contribution because of the large number of counts for ^{44}S. The other one was the uncertainty due to the placement of the ^{44}S gate. For this purpose, counts of the adjacent isotopes contributing the PID gate of ^{44}S were evaluated. This second component gave 0.8% as uncertainty for the purity value. The resulting purity with the error was 98(1)%.

For the deduction of the cross section of the one-neutron knockout channel, it is necessary to know the transmission rate of the reaction residue downstream of the secondary target. To estimate the transmission of ^{43}S from OBJ to E1, the ratio of the incoming ^{44}S and the unreacted ^{44}S reaching the very end of the S800 was measured in unreacted setting. Figure 5.2 (b) is the PID plot of outgoing particles gated on the incoming ^{44}S for events triggered by the E1 scintillator. The black short-dashed line

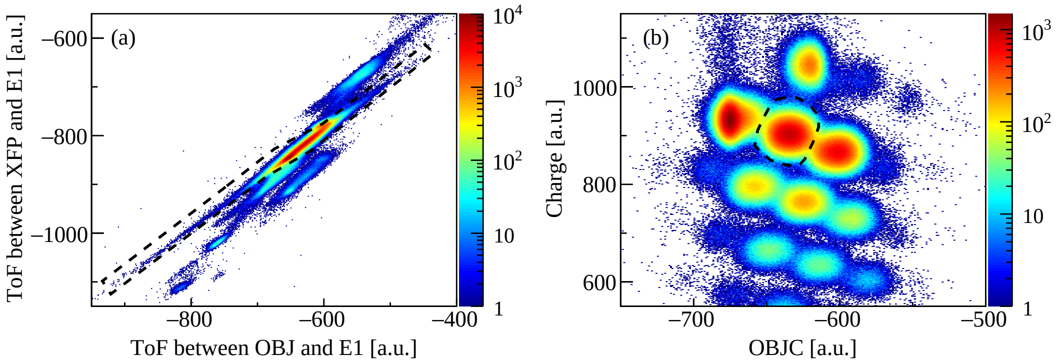

Figure 5.1: Particle identification plots for (a) incoming and (b) outgoing particles, respectively. Regions surrounded by short-dashed lines in (a) and (b) correspond to the gates for ^{44}S and ^{43}S, respectively. Note that incoming ^{44}S was selected in (b).

is the gate on the outgoing ^{44}S. The transmission was deduce by the equation of

$$\varepsilon_{trans} = \frac{N_r}{N_b LT}, \tag{5.1}$$

where N_r is the number of the unreacted ^{44}S in the focal plane when ^{44}S is gated upstream of the secondary target and data acquisition was triggered by the E1 scintillator, N_b is the number of incident ^{44}S beam particles, and LT is the live time of the measurement. For the deduction of N_b, the scaler count of the OBJ scintillator was scaled by the purity of ^{44}S in the secondary beam as described above. The average DAQ live time during the measurement of the transmission was 71%. The uncertainty of the transmission was also estimated by the same procedure described above for the purity. Besides the statistical error of outgoing ^{44}S particles and the uncertainty of the purity, the systematic uncertainty due to the placement of the PID gate was estimated. In this procedure, the uncertainty was defined as the count outside of the PID gate in Figure 5.2 (b). This is a rough estimation, but the resulting uncertainty was only 0.4% for the transmission value. Finally, the uncertainty due to the fluctuation of the secondary beam intensity was evaluated. This contribution was estimated by deducing the transmission value for each run for about one hour and taking the root-mean-square value of the deviation from the transmission deduced by accumulating all the runs. This was the largest contribution to the whole systematic uncertainty resulting in 2.8%. As the result, taking the quadratic sum of all the uncertainty discussed here, the transmission value was estimated as 81(3)%.

As for the deduction of the transmission, the placement of the PID gate on the outgoing ^{43}S is directly related to the absolute cross section of the inclusive channel and its uncertainty. The systematic uncertainty of the count of outgoing ^{43}S in the knockout setting due to the placement of the PID gate was evaluated as shown in Figure 5.3. First, the outgoing S isotopes, ranging from ^{44}S to ^{42}S, were selected with a single broad PID gate as Figure 5.3 (a). Then this histogram was projected onto the X axis, OBJC, shown in Figure 5.3 (b). In this figure, the yellow histogram corresponds to the particles inside the ^{43}S gate, and red lines are the fitted gaussian functions to the experimental data points of ^{44}S and ^{42}S shown as blue points. The overlapping region of the yellow and red spectra was defined as the contamination from the adjacent isotopes. As seen in this figure, the ^{44}S region has a tail expanding

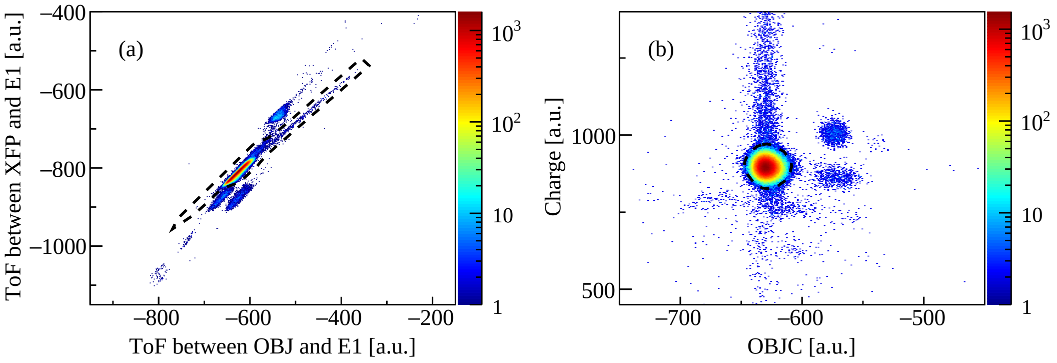

Figure 5.2: Particle identification plots for (a) incoming and (b) outgoing particles, respectively, with the rigidity setting of the S800 centered on ^{44}S. Regions surrounded by short-dashed lines in (a) and (b) correspond to the gates for incoming and outgoing ^{44}S. Note that incoming nucleus was selected on ^{44}S in (b).

into the ^{43}S region. To evaluate the contamination due to this structure, the linear function was used to fit the tail structure shown as the green line in Figure 5.3 (b). The resulting uncertainty was estimated as 3% to the total count of outgoing ^{43}S.

5.2 Gamma-ray energy histograms

By gating in the PID plots discussed in the previous chapter, the reaction channel of interest can be selected. In this chapter, prompt or delayed γ-ray energy histograms gated on the one-neutron knockout or the unreacted reaction channel will be discussed.

5.2.1 Prompt gamma-rays

Figure 5.4 shows the prompt γ-ray energy histogram measured by the GRETINA array gated on the one-neutron knockout reaction. Most of the previously observed γ-rays [33, 34] were confirmed and their energies are shown in the figure together with the uncertainty estimated in §4.3.3. A peak at 571(2) keV was newly observed in the present experiment. Note that a peak around 900 keV was from the 2_1^+ state of ^{42}S contaminants.

To deduce the yield of each prompt γ-ray, χ^2 fitting of the response function of the GRETINA to the experimental histogram was performed as mentioned in §4.3.2. The result is shown in Figure 5.5. In this fitting procedure, background γ-rays of the reaction of neutrons with Ge detectors or surrounding materials, treated in §4.2.5, were considered. Besides that, the background γ-rays were modeled as

$$N_\gamma^{BG}(E_\gamma) = \begin{cases} p_0 + p_1 \cdot E_\gamma & E_\gamma \leq E_0, \\ p_2 \exp(-p_3 \cdot E_\gamma) + p_4 \exp(-p_5 \cdot E_\gamma) & E_\gamma > E_0. \end{cases} \tag{5.2}$$

Parameters from p_0 to p_5 and E_0 were chosen to best fit the experimental data. Note that these parameters of background function were constrained by $p_0 + p_1 \cdot E_0 = p_2 \exp(-p_3 \cdot E_0) + p_4 \exp(-p_5 \cdot E_0)$. In Figure 5.5, the green short dashed line shows the result of this background function summed with the γ-rays of the reaction with neutrons and a γ-ray from ^{42}S. Deduced prompt γ-ray energies and yields are summarized in Table 5.1.

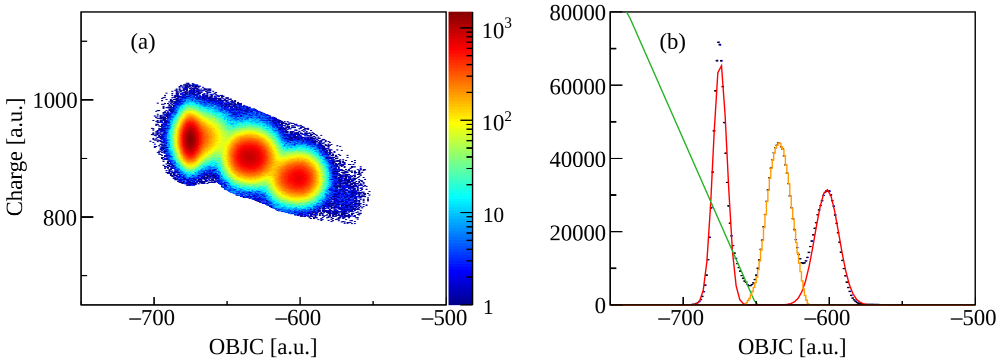

Figure 5.3: Estimation of the uncertainty due to the placement of the outgoing PID gate. (a) shows the outgoing S isotopes when ^{44}S is gated as the incoming particle. Blue points in (b) are the projection of (a) onto the X axis. Red and green lines are the results of gaussian fitting to ^{44}S and ^{42}S peaks and linear function fitting to the tail of the ^{44}S peak for the estimation of the contaminant from the adjacent isotope. Yellow line is the peak in the PID gate of ^{43}S.

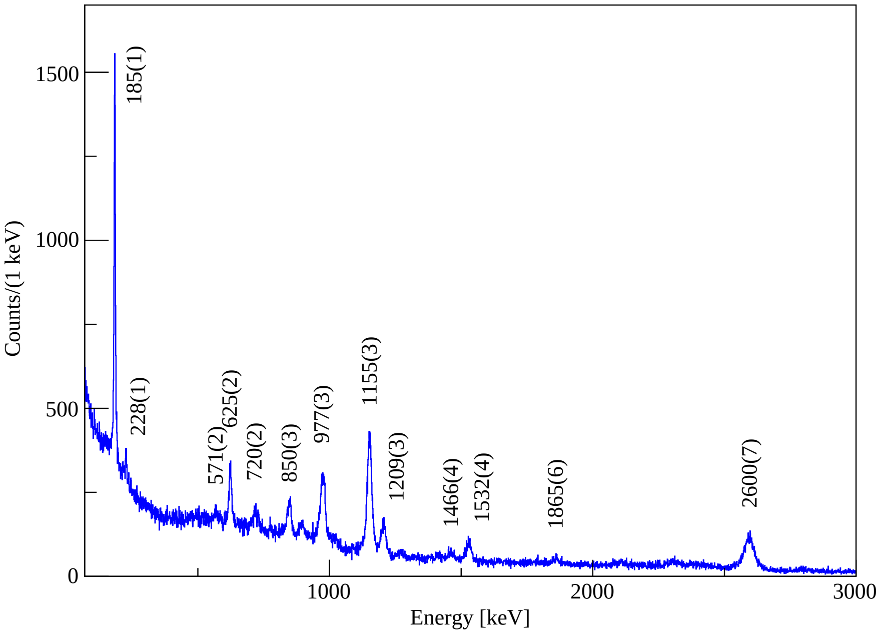

Figure 5.4: Prompt γ-ray energy histogram after Doppler correction on one-neutron knockout reaction channel from ^{44}S to ^{43}S measured by GRETINA. This histogram was obtained by applying the add-back analysis.

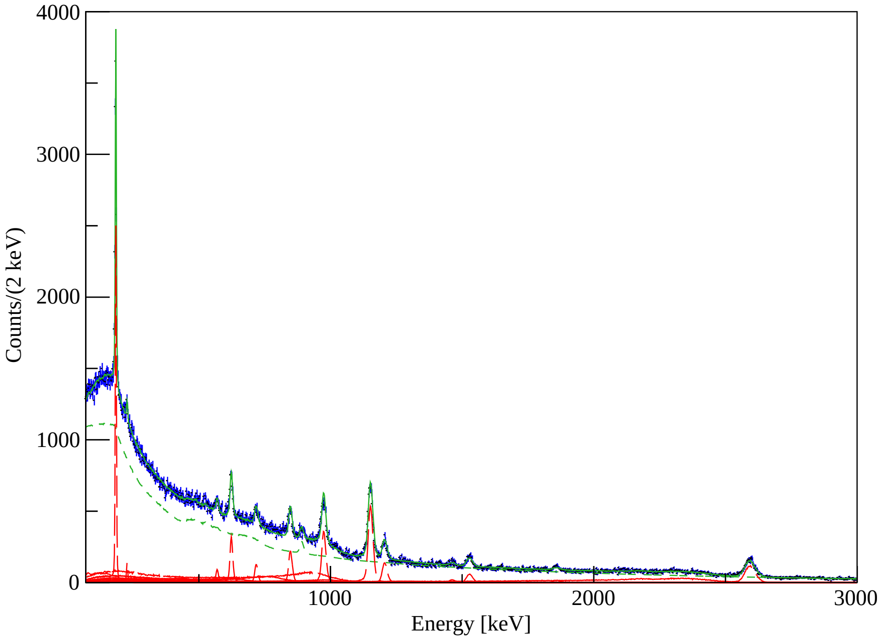

Figure 5.5: Fitting of response functions to the prompt gamma-ray energy histogram without addback. The blue points are experimental data. The red long dahsed lines represent the simulated response functions at the respective observed γ-ray energies. The green short dashed line corresponds to the fitted background, and the green solid line shows the sum of these simulated lines as the result of the statistical fits.

Then γ-γ coincidence analysis between prompt γ-rays measured by GRETINA was performed. Figure 5.6 shows the resulting coincidence matrix of one-neutron knockout channel after applying the addback procedure. Each γ-ray peak in Figure 5.4 was fitted by using a gaussian peak and linear background function. The $\pm 3\sigma$ region defined by this fitted gaussian was used as the peak region to construct the gated spectra. Higher and lower energy regions next to the peak (each 3σ width) were defined as the background. By subtracting the adjacent background regions from the peak region, background subtracted coincidence histograms were deduced as shown in Figure 5.7. Note that a few peaks are close to each other forming doublet peaks and the peak region could overlap with the neighboring background region. In this case, the background region for both peaks were defined to be the 3σ region of the higher energy side of higher peak. This background histogram was then scaled by the estimated background counts under the peak using the linear function for the fitting. In Figure 5.7 background subtracted histograms gated on 1155, 625, 850, and 977 keV peaks are shown. The coincident peaks with γ-ray energies in each panel are shown with its γ-ray energies. Also the partial level scheme proposed from this analysis is shown as Figure 5.8. Because of the treatment that the 185 keV and 1155 keV γ-rays are the de-excitation from a single excited state or they are from the two different states, there is the possibility to construct the two kinds of level schemes.

In a previous experiment the lifetime measurement of the excited states of ^{43}S was performed [34] and the same kind of γ-γ coincidence analysis was performed. From that experiment, two different states were proposed with almost the same excitation energies, at 1159 and 1161 keV. These states are supposed to have the different decay schemes from the higher states, as shown in Figure 5.8 in the case of the present work. The 1159 keV state was assumed to decay to the ground state directly and the 628 keV γ-ray was thought to feed this state from above. Other coincidences with the 1161 keV state, on the other hand, were not prominent and the proposed decay scheme of this state was a 977 → 184 keV cascade. To examine these decay scheme, especially to investigate if 625 keV γ-ray is coincident with other γ-rays, the background subtracted γ-γ coincidence histogram was compared with the simulated spectra.

Figure 5.9 shows the background subtracted coincidence histogram gated on (a) 625 keV or (b) 850 keV γ-rays and (c) is the sum of (a) and (b). In these panels, red and green histograms are results of simulations assuming different decay schemes. In the present work, 185 keV γ-ray was coincident with 977 keV γ-ray as shown in Figure 5.7 (d). By the γ-ray intensity deduced from Figure 5.5, the intensity of the 185 keV γ-ray was smaller than that of 977 keV as shown in Table 5.1. So the 1162 keV excited state was thought to decay by a 185 → 977 keV cascade. In the red histogram of Figure 5.9, the 1162 keV state was assumed to be identical to the 1155 keV state decaying to the ground state directly. This means the 1162 keV state was fed by the 850 → 625 keV cascade and decayed to the ground state by two path, a 185 → 977 keV cascade or a direct 1155 keV transition. The branching ratio of the 185 and 1155 keV transitions was deduced from the γ-ray intensity deduced from Figure 5.5. In the green histogram, on the other hand, the 1162 keV state was assumed to be different from the 1155 keV state. This means that the 850 → 625 keV cascade only fed the 1155 keV state and no transition from higher states were placed above the 185 → 977 keV cascade. By comparing these histograms with experimental data, there is a large discrepancy around the 185 keV region. The experimental data show the possible coincidence of 185 keV transition with both 625 and 850 keV but its intensity was significantly smaller than simulated one (red). On the other hand, the green histogram significantly underestimates the structure in the low energy region. Although the experimental points around 185 keV are just between the red and green

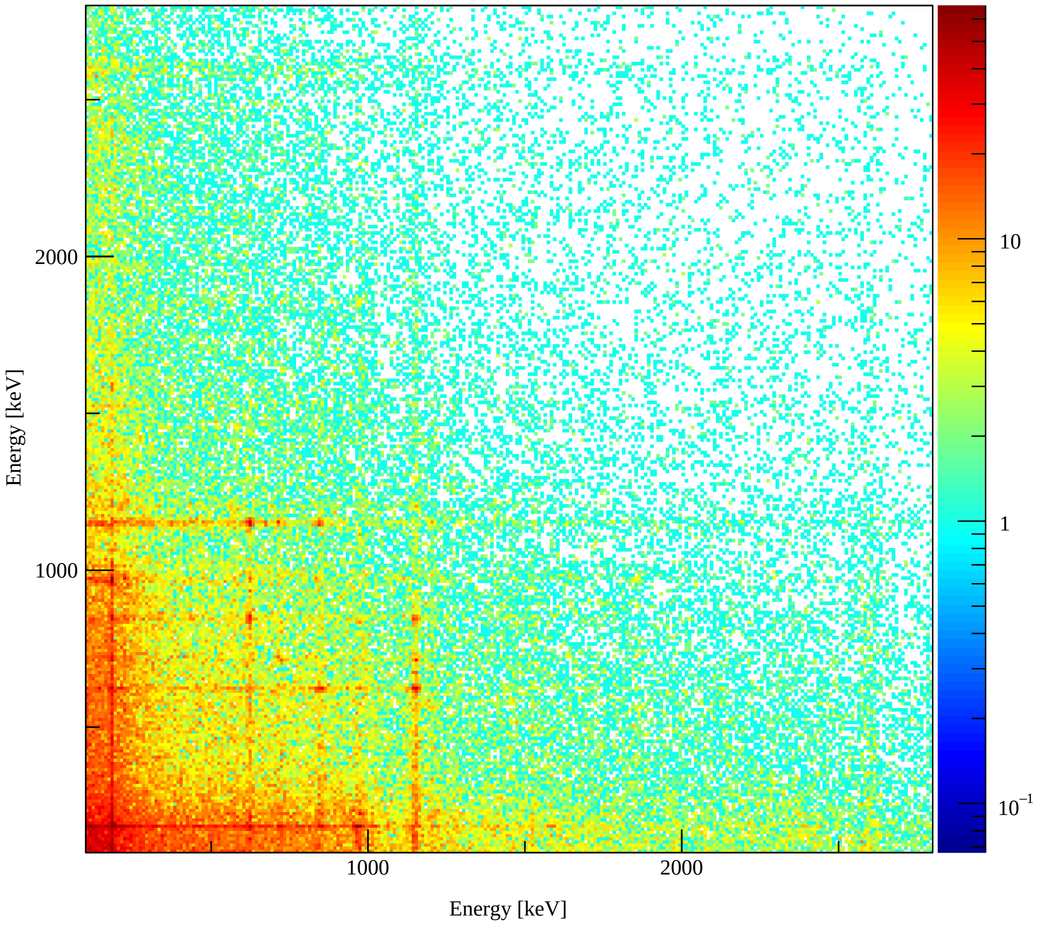

Figure 5.6: Two dimensional γ-γ coincidence matrix of prompt gamma-rays from the one-neutron knockout reaction channel from ^{44}S to ^{43}S measured by GRETINA. This histogram was obtained by applying the add-back analysis. Both X and Y axis are 10 keV/bin.

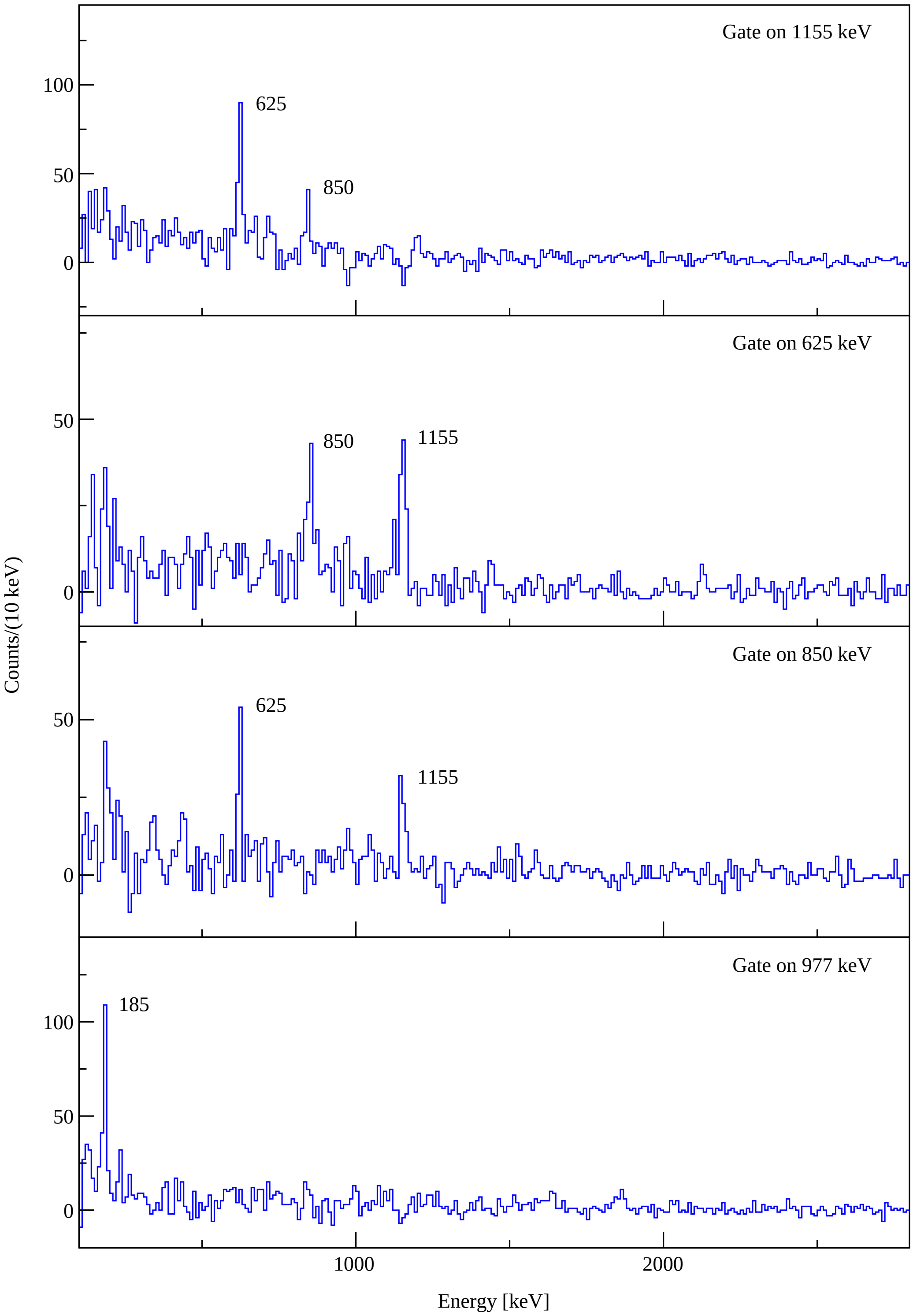

Figure 5.7: Background subtracted γ-γ coincidence spectra in GRETINA. Figure (a), (b), (c), and (d) are the spectra gated on the 1155, 625, 850, and 977 keV prompt transitions.

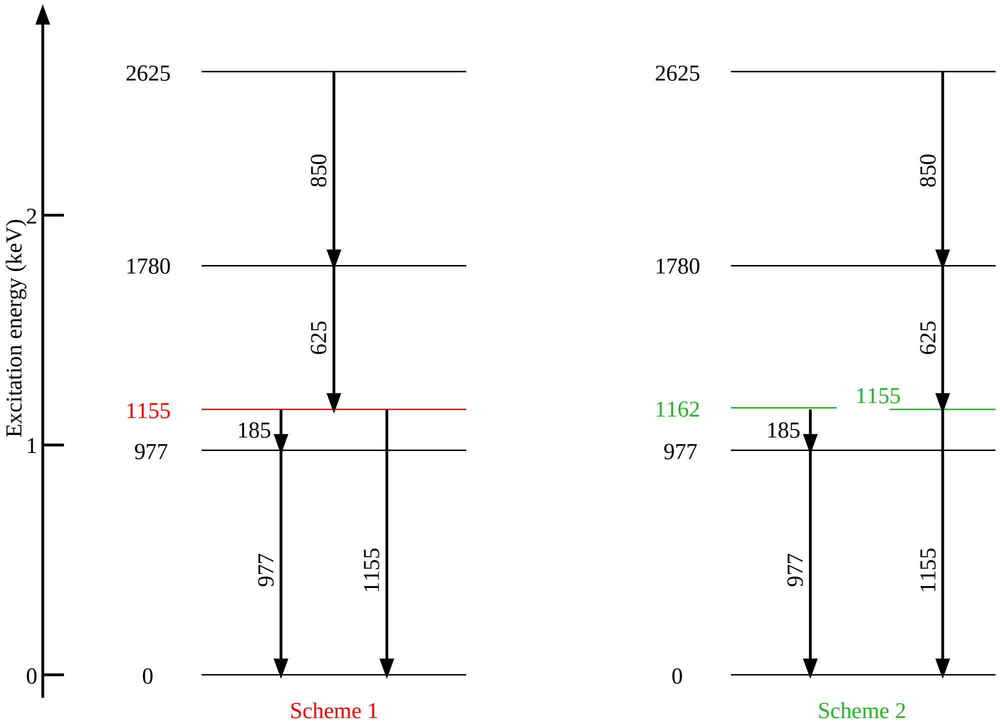

Figure 5.8: Two possible partial level schemes constructed from prompt γ-γ coincidence in GRETINA. In the scheme 1, only one excited state is placed at 1155 keV and it decays by the 1155 keV and the 185 → 977 keV γ-decays. In the scheme 2, two different excited states are placed at 1155 and 1162 keV. Former decays to the ground state directly and is fed by 185 → 977 keV cascade. Later is not fed from any higher states and decays by 185 → 977 keV cascade. The scheme 1 and 2 correspond the red and green histograms in Figure 5.9, respectively.

histograms, considering that the red histogram cannot reproduce the experimental data points and that 185 keV possible coincidence peak is only one σ above background level, especially in the histogram gated on 625 keV peak, the 850 → 625 keV cascade is assumed to be feeding only the 1155 keV state and this does not decay via a 185 → 977 keV cascade. The coincidence information of prompt γ-rays including this discussion is also summarized in Table 5.1.

5.2.2 Delayed gamma-rays

Not only the prompt γ-rays measured by GRETINA, but also the delayed γ-rays measured by the IsoTagger were analyzed as shown in Figure 5.10. In panel (a), the experimental histogram with the result of a χ^2 fitting of the response function of the IsoTagger array is shown. The previously observed γ-ray from the isomeric state at 320 keV was observed with significant counts. The fitting procedure was almost the same as that for prompt γ-rays, besides the definition of the background function. For the fitting to the delayed γ-ray histogram, the background function was chosen to be the sum of two exponential functions like the $E_\gamma > E_0$ case in Equation 5.2 in the whole energy range. The panel (b) shows the decay curve of this isomer decay. This spectrum was obtained by gating on the peak region in panel (a). The peak region

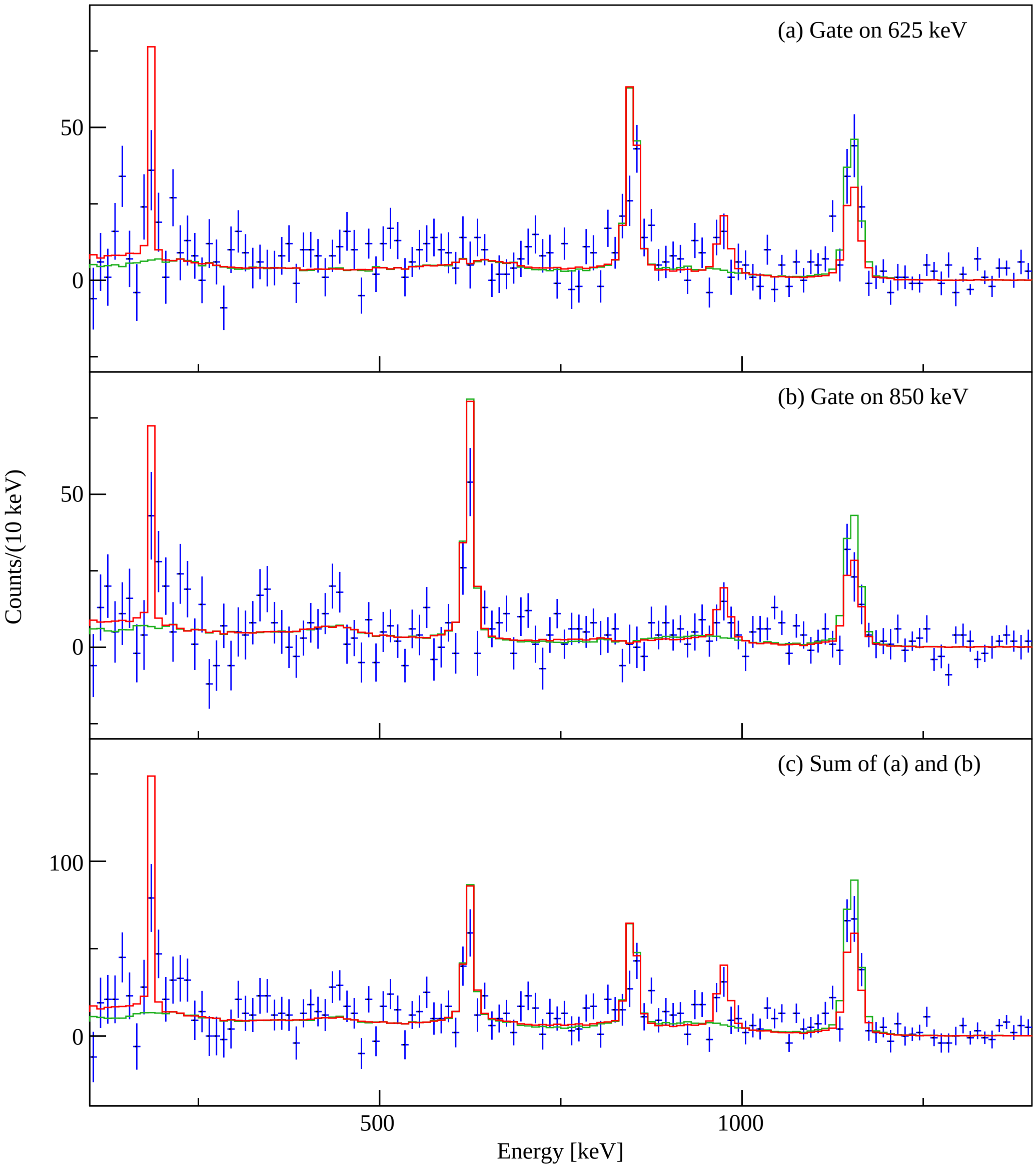

Figure 5.9: Comparison of γ-γ coincidence spectra with the simulation. (a) and (b) are the spectra gated on 625 and 850 keV transitions, respectively and (c) is the sum of (a) and (b). Blue points are the experimental data with addback. Red lines are simulated spectra assuming both 185 and 1155 keV transitions are coincident with the 850 → 625 keV cascade. The branching ratio of the 185 and 1155 keV transitions was estimated from the singles spectrum. Green lines are also simulated spectra, this time assuming 100% branching ratio for 1155 keV and no coincidence with 185 keV transition. These red and green histograms correspond to the scheme 1 and 2 in Figure 5.8, respectively.

Table 5.1: Observed γ-ray energies, efficiency-corrected intensities, and coincidence information for ^{43}S. The errors of γ-ray energies and yields include only the statistical errors.

	Energy [keV]	Yield/ions [%]	Coincident γ-rays	Level [keV]
prompt	185(1)	5.8(3)	977	1162(4)
	228(1)	0.44(7)		228(1)
	571(1)	0.93(11)		
	625(2)	3.6(2)	850, 1155	1780(5)
	720(2)	1.8(2)		
	850(3)	3.6(2)	625, 1155	2625(8)
	977(3)	7.1(4)	185	977(3)
	1155(3)	13.2(6)	625, 850	1155(3)
	1209(3)	3.6(2)		1209(3)
	1466(4)	0.67(13)		2625(8)
	1532(4)	2.2(2)	320	1856(6)
	1865(6)	0.37(13)		1856(6)
	2600(7)	9.7(5)		2600(7)
delayed	320	49(3)	1532	320

was also defined as the same manner of γ-γ coincidence analysis of the GRETINA, the $\pm 3\sigma$ region around the centroid of gaussian function with linear background function. The red line in panel (b) is the fitting result to this histogram with the exponential function and the half life of this isomeric state was deduced to be 377(4) ns in the present work. This value was used for the correction of the count of the isomeric state decaying in-flight, as discussed in §4.3.3, and the delayed γ-ray intensity after the correction is also shown in Table 5.1.

Then a delayed coincidence analysis between the IsoTagger and GRETINA was performed. Figure 5.11 shows the prompt γ-ray energy histogram of the GRETINA coincident with the 320 keV isomeric decay measured by the IsoTagger. In this coincidence analysis, the definition of the peak and the background regions were the same as for γ-γ coincidence analysis of the GRETINA and background spectra were subtracted in this figure. As clearly shown, the 1532 keV prompt γ-ray transition is coincident with the 320 keV transition from the isomeric state.

Not only for the measurement of the isomer of ^{43}S, but also for the estimation of the isomeric ratio of ^{44}S in the beam the IsoTagger was used. ^{44}S has a 0_2^+ state at 1357 keV with a half-life of 2.619(29) μs [27, 28]. This state decays both to the ground state by a $E0$ transition and to the 2_1^+ state at 1319 keV by a $E2$ transition. The $E0$ transition has two process; the emission of the internal conversion electron (IC) and the internal pair formation (IPF). Because the setup of the present experiment was not dedicated to the measurement of electrons or positrons, the direct observation of the $E0$ transition was difficult. The branching ratio of $E0$ and $E2$ transition was measured as $R = \lambda(E2)/\lambda(E0) = 0.163(13)$, where λ denotes the intensity of the corresponding transition [28]. If the 0_2^+ state was produced in the fragmentation reaction and present in the secondary beam, the isomer ratio can be measured by using the delayed transition from 2_1^+ to the ground state.

Figure 5.12 is the γ-ray energy histogram coincident with the unreacted ^{44}S with the S800 setting centered to ^{44}S. As shown in this figure, there is no prominent peak at 1319 keV, which indicates that the amount of produced 0_2^+ states was negligibly small.

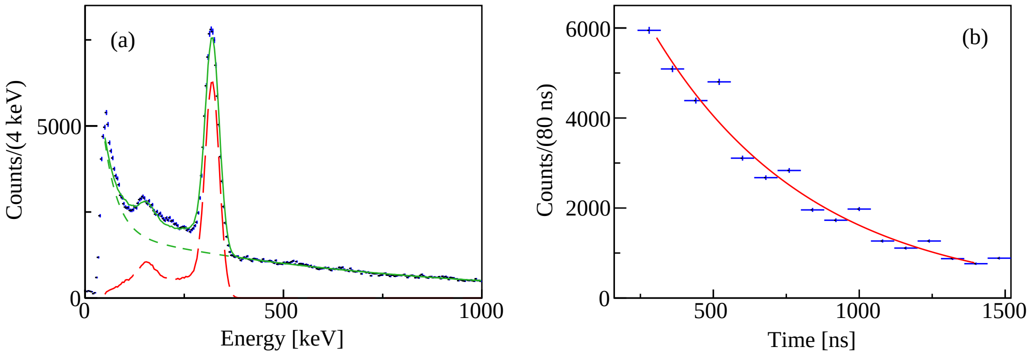

Figure 5.10: Delayed γ-ray energy spectrum and decay time histogram for the one-neutron knockout reaction. In Figure (a), blue points are experimental data. Red long dahsed line represents the simulated response function at the observed γ-ray energy. Green short dashed line corresponds to the fitted background, and green solid line shows the sum of these lines as the result of the statistical fits. Figure (b) shows the timing spectrum of the isomeric transition in IsoTagger with the fitting result with an exponential function shown as the red line.

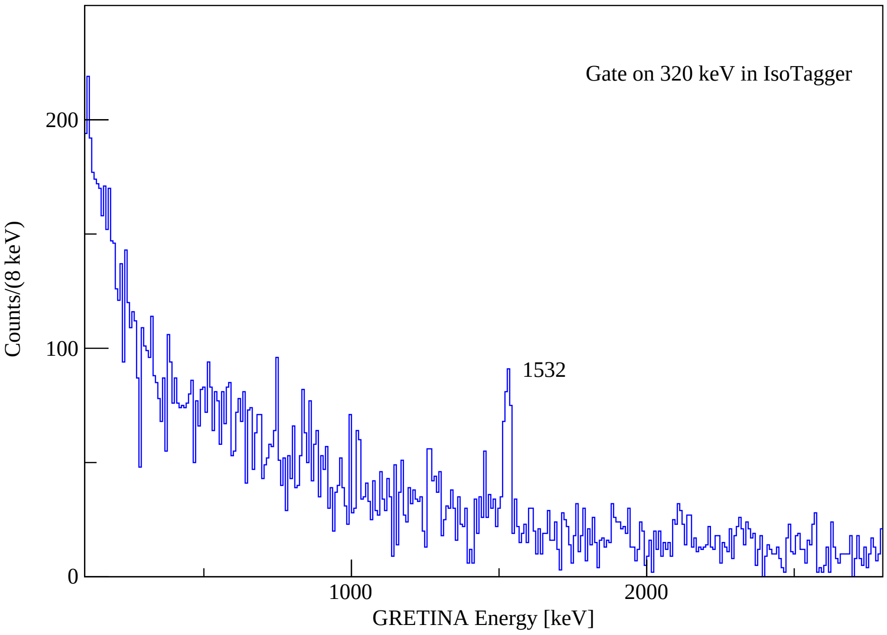

Figure 5.11: Background subtracted delayed coincidence spectrum between GRETINA and IsoTagger. This figure is the energy spectrum measured in GRETINA when 320 keV isomeric transition was measured in IsoTagger.

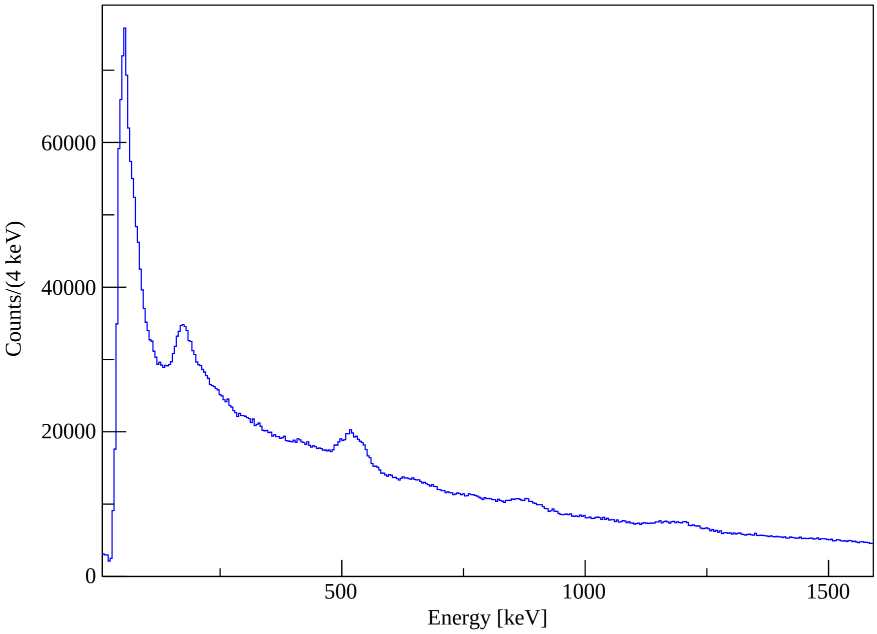

Figure 5.12: γ-ray energy histogram of ^{44}S → ^{44}S channel measured by the IsoTagger array for the estimation of the isomer ratio of the 0_2^+ state of ^{44}S.

On the other hand, there is a significant peak at 511 keV, which could be due to the annihilation of positrons produced by IPF. The $E0$ transition rate is described as [28]

$$T_{E0} = \rho^2(E0)(1+R)(\Omega_{\mathrm{IPF}} + \Omega_{\mathrm{IC}}), \tag{5.3}$$

where $\rho^2(E0)$ is the monopole strength of the transition from 0_2^+ to the ground state, and two parameters of Ω_{IPF} and Ω_{IC} are the electronic factors of IPF and IC. By the gaussian fitting to this 511 keV peak and considering the photo peak efficiency of the IsoTagger at this energy is 15.0%, this peak count corresponds to 4.01×10^5 $E0$ decay by IPF. Taking previously used values of R, $\Omega_{\mathrm{IPF}} = 1.495 \times 10^7$ sec^{-1} and $\Omega_{\mathrm{IC}} = 1.1125 \times 10^7$ sec^{-1} [28], the total production of 0_2^+ state can be estimated as 8.13×10^5. Because the counts of ^{44}S→^{44}S events in this setup was 3.60×10^7, an upper limit for the isomer ratio is 2.26%. Note that this value is under the strong assumption that all of the 511 keV peak was due to the $E0$ transition. If this assumption is correct, the counts of observed 1319 keV γ-ray should be 1.00×10^4 considering the branching ratio. This peak content must be clearly visible, for example the count rate of the peak at 1200 keV in Figure 5.12 amounts to 1.87×10^4. Because there is no visible peak at 1319 keV with the same order of counts with the peak at 1200 keV, it is reasonably assumed that the isomeric ratio is much smaller than 2.26%, which is the maximum value estimated from this setup. In the following discussion about the cross section, the error due to the isomer ratio is thus neglected.

5.3 Parallel momentum distribution

Now coincidence information and yields of observed γ-rays were properly obtained. Considering these observables, analysis on $P_{//}$ of each state of ^{43}S was performed. Figure 5.13 shows the comparison of the experimental $P_{//}$ of each excited state with the theoretical distribution calculated at the corresponding excitation energy [70, 76].

Table 5.2: Reduced χ^2 values for the theoretical momentum distribution compared to the experimental data.

E_{level} [keV]	$l = 1$	$l = 2$	$l = 3$
320	80.9		5.2
1155	1.2		15.6
1162	1.1		7.9
1209	1.2		4.0
2600	2.9	0.69	4.7
2630	8.7		1.3
ground state	1.5		1.2

Only in the panel (a), theoretical distribution of neutron knockout from $l = 2$ orbit is also present because this excited state at 2600 keV is just under the neutron threshold of ^{43}S and there can be a possibility of neutron knockout under $N = 20$ shell gap. To examine which distribution is the best to reproduce the experimental one, χ^2 value between the experimental points and each theoretical curve was calculated. Because of the tail structure in the lower momentum region, which is not reproduced by the eikonal reaction calculation, this χ^2 calculation is restricted to the region ranging from 17.3 to 17.8 GeV/c. This region is shown as solid lines in Figure 5.13 and the lower region which is not used for the χ^2 calculation is drawn as dashed lines. This is the same momentum region used for the scaling of the theoretical curve to match the count of experimental data. By this evaluation, the best theoretical distribution reproducing the experimental data was deduced as neutron knockout from $l = 2$ orbit for the panel (a), that from $l = 1$ orbit for panels (b)-(d), and that from $l = 3$ orbit for panels (e) and (f). The reduced χ^2 values for this analysis are described in Table 5.2.

By subtracting all the distributions of all the excited states from that of the inclusive channel, the distribution directly producing the ground state of ^{43}S via one-neutron knockout was extracted. Figure 5.14 shows the result of this analysis. The reduced χ^2 values mentioned above between the experimental distribution and the theoretical calculation of neutron knockout from $l = 1$ and 3 orbit were 15.1 and 10.3, respectively (number of degree of freedom = 10). Mainly because of ambiguities in the level scheme due to the unplaced prompt γ-rays, a clear distinction between the neutron knockout from $l = 1$ or 3 orbit was not possible. In the following discussion, the spin and parity of the ground state of ^{43}S is assumed to be $3/2^-$, which was suggested from the transition rate from the $7/2^-$ isomeric state at 320 keV and to the ground state [29].

One of the points worth checking related to the analysis of $P_{//}$ is investigating if the acceptance for the reaction residue was cut by the spectrometer setting. Figure 5.15 shows the acceptance plots, d_{ta} versus a_{ta}, for the one-neutron knockout setting from ^{44}S to ^{43}S. The panel (a) is the inclusive channel and the others are the examples coincident with γ-rays. The panel (b) is coincident with the 1155 keV prompt γ-ray and (c) is coincident with the 320 keV delayed γ-ray. As clearly shown here, significant acceptance cuts are not present in all cases. This means that there is no need for further acceptance correction, which is also indicated by the good agreement betweem the experimental distribution and the theoretical one in the Figure 5.13 especially at the high momentum region.

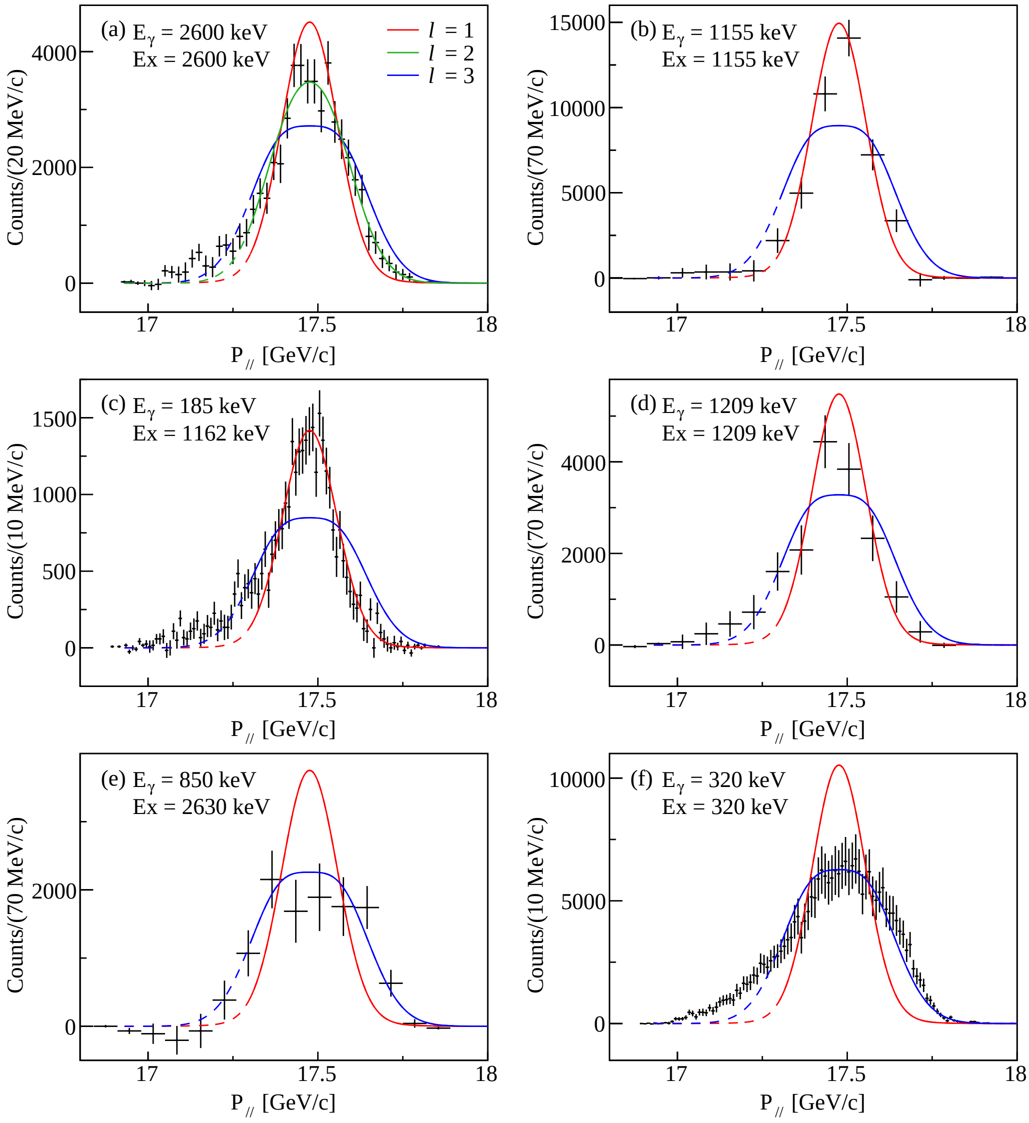

Figure 5.13: Parallel momentum distributions of the one-neutron knockout reaction coincident with γ-rays. In all panels, black points are experimental data, red, green, and blue lines correspond to the theoretical distributions of neutron knockout from $l = 1$, 2, and 3 orbits, respectively. Solid lines corresponds to the momentum region used for the normalization and the χ^2 calculation to the experimental data, from 17.3 to 17.8 GeV/c, and dashed lines are out of this range. Coincident γ-ray energies and excited energies of corresponding states are also shown. Note that Figure (f) is the spectrum coincident with the isomeric transition measured in IsoTagger, while others are obtained by gating prompt transitions measured in GRETINA.

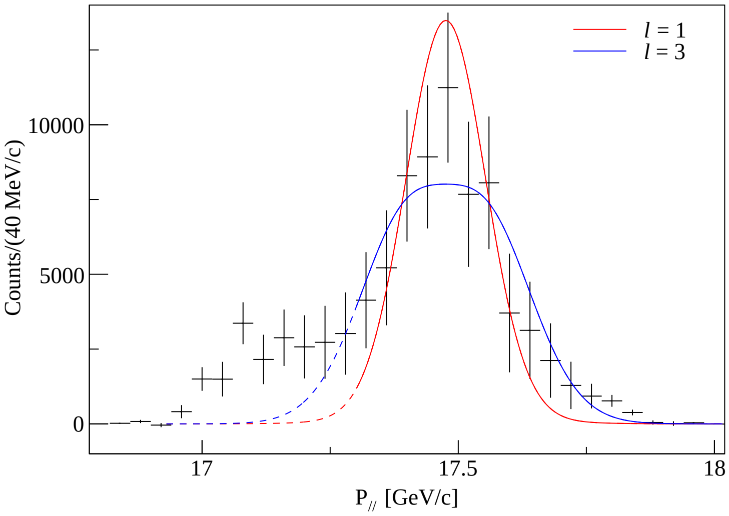

Figure 5.14: $P_{//}$ of the ground state of ^{43}S populated in the one-neutron knockout reaction. This is the same type of figure as 5.13.

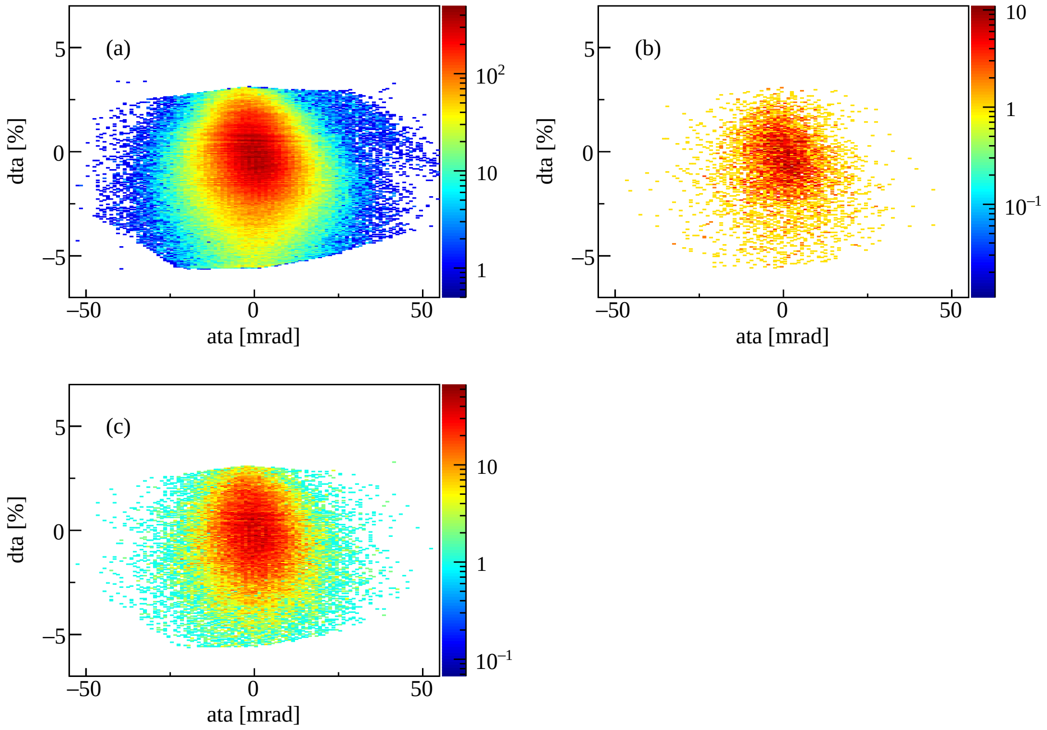

Figure 5.15: Acceptance plots of d_{ta} and a_{ta} for the one-neutron knockout reaction. (a), (b), and (c) correspond to the plots of the inclusive channel, coincident with the 1155 keV prompt transition, and coincident with the 320 keV isomeric transition, respectively.

5.4 Cross section

The inclusive cross section of the one-neutron knockout from ^{44}S to ^{43}S is obtained by

$$\sigma_{ko} = \frac{N_r}{N_b n_t LT \varepsilon_{trans}}, \tag{5.4}$$

where N_r is the number of knockout residue ^{43}S, N_b is the number of incident beam particle ^{44}S, n_t is the areal target number density, LT is the DAQ livetime of the measurement, and ε_{trans} is the transmission of the reaction residue through the S800.

N_r was obtained by integrating the total counts in the PID gate shown in Figure 5.1. Note that there was an additional condition in this integration that the data acquisition was triggered by the E1 scintillator, which guaranteed that ^{43}S had reached the very end of the S800. The uncertainty of this value consists of the statistical uncertainty, $\sqrt{N_r}$, and the systematic error of the placement of the PID gate for the outgoing particle as discussed in §5.1. N_b was deduced by scaling the count of OBJ scintillator recorded by the scaler module by the purity of ^{44}S in the secondary beam. Besides the statistical uncertainty, the error of purity, evaluated also in §5.1, was also considered for the uncertainty of N_b. The transmission was already evaluated as 81(3)% in §5.1 and the average DAQ livetime of the measurement was 0.997. The thickness of the secondary target and its uncertainty was 376(4) mg/cm^2. Other than the components contributing to the uncertainty of the inclusive cross section, the systematic uncertainty due to the fluctuation of the incoming beam intensity was evaluated as shown in Figure 5.16. As the result, the inclusive cross section of one-neutron knockout reaction was deduced as 91(2) mb. In the previous experiment using the same reaction [33], the inclusive cross section was deduced as 79(7) mb, consistent but a larger value in this experiment.

The exclusive cross section populating the specific final state i of ^{43}S was deduced from the inclusive cross section multiplied by the probability P_i of population of the state,

$$\sigma_i = \sigma_{ko} P_i. \tag{5.5}$$

The probability was calculated from the γ-ray yield per outgoing ^{43}S, Y_i, for all the γ-rays D_i that de-excite the state i and those for all the γ-rays F_i that feed the state i from above,

$$P_i = \sum_{j \in D_i} Y_j - \sum_{j \in F_i} Y_j, \tag{5.6}$$

and the probability for populating the ground state was calculated by subtracting the probabilities for all excited states,

$$P_{GS} = 1 - \sum_i P_i. \tag{5.7}$$

The uncertainty, Δ, of these values was estimated as

$$(\Delta_{P_i})^2 = \sum_{j \in D_i + F_i} (Y_j)^2 . \tag{5.8}$$

The summary of the cross sections for all the observed states with the spins and the parities deduced in §5.3 are summarized in Table 5.3.

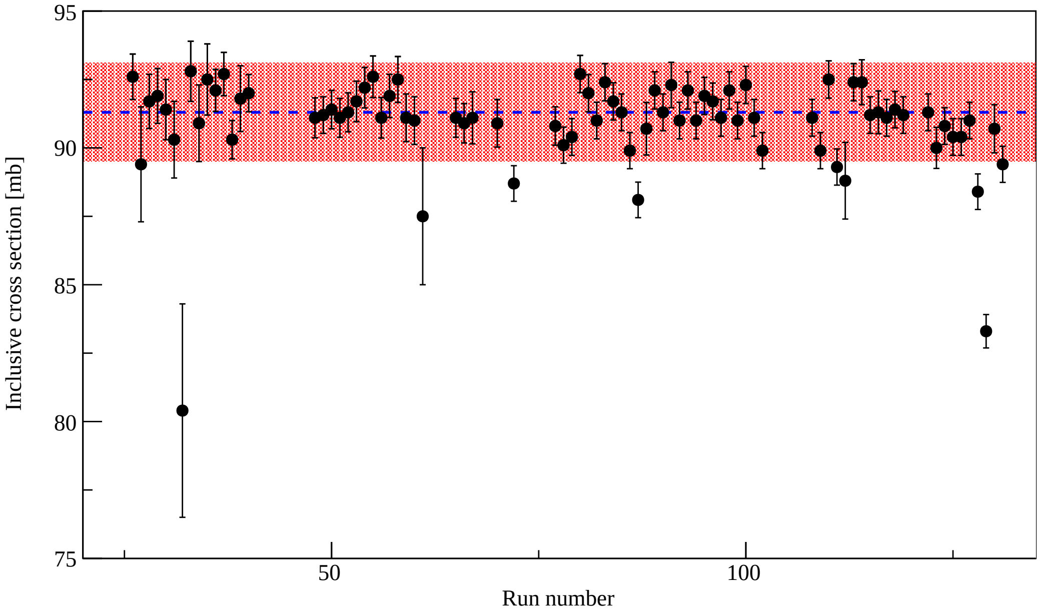

Figure 5.16: Inclusive cross section deduced for each run. Blue dashed line is the cross section deduced by accumulating all runs. Red hatched area shows the root-mean-square value of the deviations from the blue dashed line.

Table 5.3: Inclusive and exclusive cross sections to bound final states.

E_{level} [keV]	J^{π}_{level}	σ_{level} [mb]	J^{π}_{eik}	σ_{sp} [mb]	C^2S_{exp}
0	$3/2^-$	12(4)	$3/2^-$	22.1	0.63(16)
228	$(1/2^-)$	0.4(1)	$1/2^-$	21.1	0.021(4)
320	$7/2^-$	43(3)	$7/2^-$	14.4	3.37(26)
977		1.2(6)			
1155	$3/2^-$, $1/2^-$	8.2(9)	$3/2^-$	18.9	0.49(5)
1162	$3/2^-$, $1/2^-$	5.3(3)	$3/2^-$	18.9	0.32(3)
1209	$3/2^-$, $1/2^-$	3.3(2)	$3/2^-$	18.8	0.20(2)
1780		0.0(4)			
1856		2.3(3)			
2600	$5/2^+$, $3/2^+$	8.8(4)	$3/2^+$	10.7	0.95(6)
2625	$7/2^-$, $5/2^-$	3.9(3)	$7/2^-$	12.2	0.36(3)
inclusive		91(2)			

Chapter 6

Discussion

In this chapter, the experimental observables are compared with those of shell model calculations and the physics discussion is performed.

6.1 Level and decay scheme

The level scheme of ^{43}S is shown in Figure 6.1 and compared with the results of shell model calculations using the SDPF-MU and the SDPF-U effective interactions with the NushellX code [109]. For each case, the spin-parity and the knockout cross section for each state are shown. The theoretical knockout cross sections were calculated from the single-particle cross section using the eikonal approach (see §2.3) and the shell model spectroscopic factors. Additionally an empirical reduction factor R_S was used to take into account that not the full strength is experimentally observed [76, 81]. R_S depends on the binding energy asymmetry $\Delta S = S_n - S_p$ and for ^{44}S $R_S = 0.83(4)$ was estimated from experimental data [76]. The experimental level scheme was constructed by considering the coincidence information summarized in Table 5.1 and the order of transitions in a γ-ray cascade was determined by the observed γ-ray yields. Note that the 1466 and 1865 keV γ-rays were put in the level scheme just because their energies equal to the sum of other transition energies, 1466 $\sim$ 850+625 keV and 1865 $\sim$ 1532 + 320 keV. Also the 1209 keV transition was placed feeding the ground state. If the 1209 keV transition would be another state, coincidences should be observed in Figure 5.6 and 5.7 since its intensity is similar to the 850 and 625 keV transitions that show clear coincidences. Actually, part of the level scheme was suggested by a lifetime measurement of excited states of ^{43}S [34]. In that work, a γ-ray cascade of 977 $\rightarrow$ 184 keV was suggested inverted compared to the original proposal by Riley. In this work, however, the opposite order 185 $\rightarrow$ 977 keV is proposed due to their γ-ray yields, see Table 5.1.

In addition to the experimental result, Figure 6.1 shows calculated level schemes using two different interactions. Excited states with negative parity and spin up to 7/2 are shown up to the neutron threshold of ^{43}S, $S_n = 2629(6)$ keV [86]. Shell model calculations predict three band structures in the lower excitation energy in ^{43}S: a rotational band on the ground state, excited states on the isomeric state, and a band with possible different shape [43]. The ground state is thought to be prolate deformed, which results in a $K = 1/2$ rotational band with band members in the specific order of $3/2^-$, $1/2^-$, $7/2^-$, and $5/2^-$ states from lower excitation energy. This order of excited states is characterized in the prolate deformed state and does not appear in spherical or oblate deformed nuclei. In the calculations, the $1/2^-$ state at 135 keV (299 keV), the $7/2^-$ state at 874 keV (1010 keV), and the $5/2^-$ state at 1035 keV (1400 keV) using the SDPF-MU (SDPF-U) interaction are characterized as the rotational band members on the ground state due to large $B(E2)$ values of the transitions between these states. The spin and parity of the ground state of ^{43}S was indirectly measured

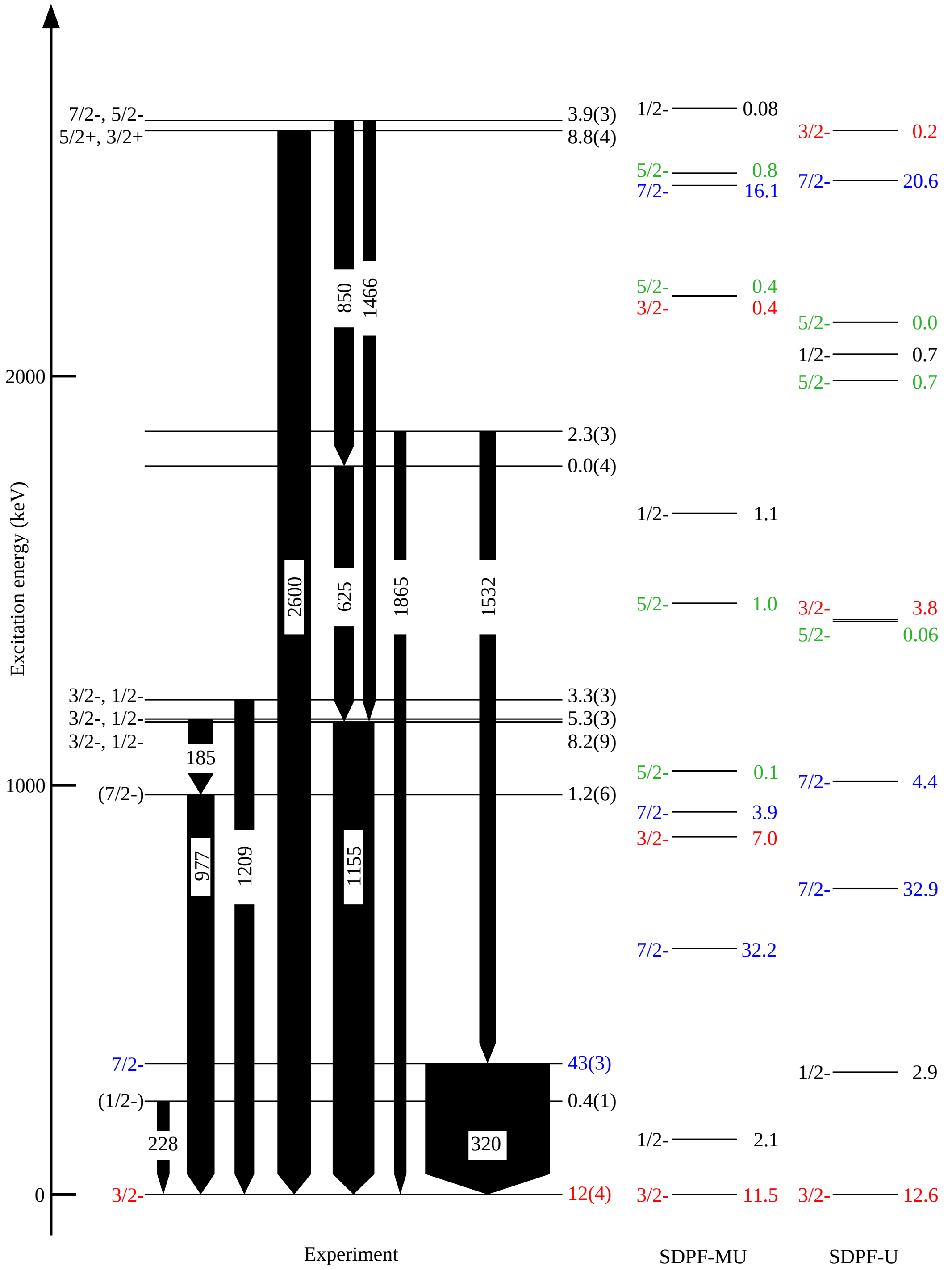
Excitation energy (keV)
0
1000
2000
7/2-, 5/2-
5/2+, 3/2+
3.9(3)
8.8(4)
2.3(3)
0.0(4)
3/2-, 1/2-
3/2-, 1/2-
3/2-, 1/2-
3.3(3)
5.3(3)
8.2(9)
(7/2-)
1.2(6)
7/2-
43(3)
(1/2-)
0.4(1)
3/2-
12(4)
185
228
977
1209
2600
850
1466
625
1155
1865
1532
320
Experiment
1/2- 0.08
5/2- 0.8
7/2- 16.1
5/2- 0.4
3/2- 0.4
1/2- 1.1
5/2- 1.0
5/2- 0.1
7/2- 3.9
3/2- 7.0
7/2- 32.2
1/2- 2.1
3/2- 11.5
SDPF-MU
3/2- 0.2
7/2- 20.6
5/2- 0.0
1/2- 0.7
5/2- 0.7
3/2- 3.8
5/2- 0.06
7/2- 4.4
7/2- 32.9
1/2- 2.9
3/2- 12.6
SDPF-U

Figure 6.1: Level schemes of ^{43}S deduced from the present experiment and predicted by shell model calculations. In the experimental level scheme, observed γ-ray transitions are shown as arrows and their width reflect the γ-ray emission yield. In the experimental results and the shell model calculations, spin-parity and production cross section [mb] using Equation 2.47 of each state are presented. Spins and parities of $1/2^-$, $3/2^-$, $5/2^-$, and $7/2^-$ are indicated in black, red, green, and blue, respectively.

to be $3/2^-$ [29]. Shell model calculations predict the same situation for the ground state and a characteristic $1/2^-$ state in lower energy region [26, 43]. In the present experiment, the 228 keV γ transition is a candidate for the decay of the $1/2^-$ state to the $3/2^-$ ground state. The 977 keV transition was first observed in the Coulomb excitation experiment [32] and confirmed in other reaction channels, which implies this transition can be attributed to the de-excitation from an excited state with collective nature. Comparing the excitation energies and considering that the production cross section of $5/2^-$ state predicted in shell model calculations is quite small, the 977 keV γ-ray is placed as the transition from the $7/2^-$ state to the ground state. In the shell model calculations, $7/2^-$ rotational member decays to the ground state with almost 100% branching ratio. Combining all results, 228 and 977 keV γ-rays can be reasonably attributed as the transitions between the rotational band members. See Figure 6.2 in the following discussion to distinguish the different band structure of both experimentally and theoretically predicted ones.

By investigating the ratio of the neutron and proton configurations in the calculated wave function, the nature of the corresponding state can be discussed qualitatively [43]. The ground state of ^{44}S is calculated to be dominant $2p2h$ neutron configuration, mostly excitations from the $f_{7/2}$ to the $p_{3/2}$ orbital, $(f_{7/2})^{-2}(p_{3/2})^{+2}$, or higher orbits in the fp shell. The one-neutron knockout reaction from this neutron configuration is naively thought to result in $1p1h$ configurations, like $(f_{7/2})^{-2}(p_{3/2})^{+1}$, or $2p2h$ configuration, $(f_{7/2})^{-3}(p_{3/2})^{+2}$ in ^{43}S. In the present calculations, the main component of the neutron configuration of the ground state band of ^{43}S is $(f_{7/2})^{-2}(p_{3/2})^{+1}$ and the deduced deformation parameters are consistent with the picture of prolate deformation. This result is also supported by a calculation of the antisymmetrized molecular dynamics (AMD) model [16]. The mechanism of this deformation is explained by the tensor-force in the shell model framework [15]. In moving from ^{48}Ca to ^{44}S on the $N = 28$ isotone line, the neutron $f_{7/2}$-$p_{3/2}$ spacing decreases due to the increasing vacancy of the protons in the $d_{3/2}$ orbit. The quenching of the $N = 28$ shell gap by this mechanism triggers a energy gain due to quadrupole correlations by mixing of protons in the $s_{1/2}$ and $d_{3/2}$ orbits, resulting in prolate deformation. It is worth noting, however, that the potential energy surface of this deformed ground state does not have a deep minimum and is γ-soft-like in nature.

Thanks to the setup of the present experiment which enabled the observation of delayed γ-rays, the excited state decaying to the isomeric state at 320 keV was identified for the first time. In the interpretation within the shell model framework, this state was originally interpreted as the neutron single-hole state with a $(f_{7/2})^{-1}$ configuration. After the spectroscopic quadrupole moment of this state was measured and found to be larger than that of a pure single-hole state, the interpretation of this state changed. In the AMD calculation, this state is predicted as the band head of the $K = 7/2$ band with triaxial deformation resulting from the contribution of neutron orbits originating from the spherical $f_{7/2}$ and $p_{3/2}$ orbits [16]. This interpretation was supported by the re-examined shell model calculation [43] which suggests that the neutron configuration of this state is $0p0h$, $(f_{7_2})^{-1}$, and not spherical but triaxial with $\gamma \sim 30°$. From the experimental point of view, since this state has $J^\pi = 7/2^-$, the possible spin-parity of the 1856 keV state above this isomer ranges from $3/2^-$ to $11/2^-$, assuming $M1$ and $E2$ transitions. Almost all excited states below 3 MeV predicted in shell model calculations have only small γ-ray branching ratio to this isomeric state. One of the candidates corresponding to the 1865 keV excited state is a $7/2^-$ state at 3167 keV in the SDPF-MU result or a $5/2^-$ state at 3079 keV in the SDPF-U result. These states decay to the isomeric state with about 45% branching ratio. The theoretical production cross section of the $5/2^-$ state at 3079 keV in the

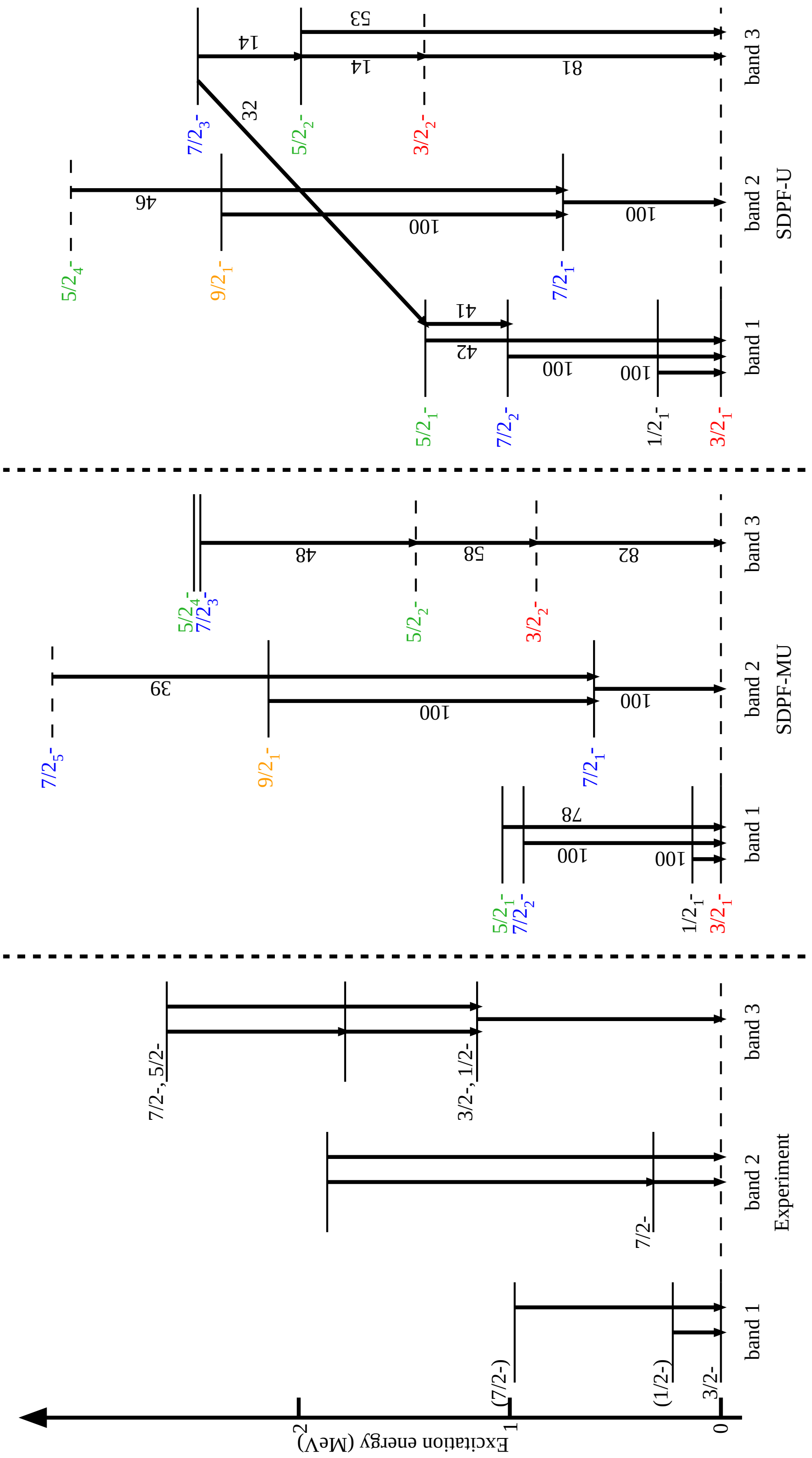
Excitation energy (MeV)
0
1
2
Experiment
band 1
band 2
band 3
3/2-
(1/2-)
(7/2-)
7/2-
3/2-, 1/2-
7/2-, 5/2-
SDPF-MU
band 1
band 2
band 3
3/2-1
1/2-1
7/2-2
5/2-1
100
100
78
7/2-1
9/2-1
7/2-5
100
100
39
3/2-2
5/2-2
7/2-3
5/2-4
82
58
48
SDPF-U
band 1
band 2
band 3
3/2-1
1/2-1
7/2-2
5/2-1
100
100
42
41
7/2-1
9/2-1
5/2-4
100
100
46
3/2-2
5/2-2
7/2-3
81
14
14
53
32

Figure 6.2: Decay schemes of ^{43}S drawn separately for each band. Band 1, 2, and 3 represent the rotational band on the ground state, band on the isomeric state, and the third band. Dashed lines show the states which are not attributed in the band but on the decay pass of higher states. Arrows are the γ transitions shown with the branching ratio (%). See text more detail.

SDPF-U result is less than 0.01 mb, but that of the $7/2^-$ state at 3167 keV in the SDPF-MU result is about 2.63 mb, which is in good agreement with the observed production cross section of 1865 keV. Additionally, the electric quadrupole moment of the $5/2^-$ state at 3079 keV in SDPF-U result is predicted as -21.0 efm^2, though that of the isomeric state predicted at 748 keV is calculated as 30.0 efm^2, which may imply that different states in higher excitation energy are in the same band as this isomeric state.

Other candidates for the 1865 keV state in shell model calculations are the $9/2^-$ states predicted at 2143 keV and 2366 keV in the SDPF-MU and SDPF-U calculations, respectively [43]. These states have strong $B(E2)$ values for the transitions to the $7/2^-$ isomeric state and decay to this state with almost 100% branching ratio, which implies these states are in the same band. The production cross sections of these $9/2^-$ states, however, are quite small because the direct production of these states should be involved with the neutron with 9/2 total spin, which is very high energy compared to the Fermi surface. As mentioned before, $11/2^-$ states can also be in the same band built on this isomeric state, but the $11/2^-_1$ state in both calculations, predicted around 3 MeV, has a strong $B(E2)$ value to the predicted $7/2^-_2$ state which can be attributed as the member of the rotational band and decays to this state.

Other than the rotational band built on the ground state and excited states above the isomeric state, a possible band structure above 1 MeV is proposed in the present work. In the lifetime measurement experiment, a γ-γ coincidence analysis was performed and only the 628 keV γ-ray was observed in coincidence with 1159 keV γ-ray. In the present experiment, both 625 and 850 keV γ-rays are found to be coincident with the 1155 keV γ-ray. Considering that the 850 keV γ-ray was observed but not coincident with 1159 keV γ-ray in the lifetime measurement experiment, and the yields of the 625 and 850 keV γ-rays are almost the same in the present experiment, the cascading transitions $850 \to 625 \to 1155$ keV are proposed leading to a state at 2625 keV. The parallel momentum distribution for the population of 2625 keV state can be well explained by the neutron knockout from a $l = 3$ orbit. Comparing the level schemes and production cross sections with the shell model calculations, the $7/2^-_3$ states at 2466 keV in the result with the SDPF-MU and one at 2478 keV in the result with the SDPF-U interaction are candidates for the observed 2625 keV state. The possible band head of the third band has spin-parity of $3/2^-$ or $1/2^-$ and may correspond to the $3/2^-_2$ state at 874 keV in the SDPF-MU result and $3/2^-_2$ state at 1405 keV in the SDPF-U result comparing the production cross sections. The experimental 1780 keV intermediate state then can be attributed to the calculated $5/2^-_2$ state. In the calculation with the SDPF-MU interaction, the $7/2^-_3$ state decays to the $5/2^-_2$ state with about 50% branching ratio and the $5/2^-_2$ state decays to the $3/2^-_2$ state with 55% branching ratio. Then the $3/2^-_2$ state decays directly to the ground state with more than 80% branch, which is in good agreement with experimentally proposed decay scheme. In the SDPF-U scheme, however, the $7/2^-_3$ state decays to a member of the rotational band, the $5/2^-_1$ state, with a 32% branch, which is the most intense de-excitation from this state. The decay branch to the $5/2^-_2$ state ammounts to only about 14%. The strongest decay branch from the $5/2^-_2$ state is the transition to the ground state with 53% and the branching ratio to the $3/2^-_2$ state amounts to 13%. Though the $3/2^-_2$ state decays to the ground state with a 87% branch, which agrees with the calculation with the SDPF-MU interaction, the whole decay pattern differs from the other calculation.

Though this discussion is from the experimental side, the structure of this band can be qualified by the comparison with the theoretical calculations. In the SDPF-U calculation, the third band is predicted as a $K = 5/2^-$ band with the $5/2^-_2$ state band head [43]. This is established by the investigation of the neutron configuration of the wave function and band members of this state are found to have dominant $2p2h$, $(f_{7/2})^{-3}(p_{3/2})^{+2}$, neutron configuration. This configuration results in the prolate deformation with a small γ value. Because the neutron configuration of the $3/2^-_2$ state is dominated by a $1p1h$ configuration, this state cannot be attributed as the band head of this third band. In the SDPF-MU calculation, the corresponding level is the $5/2^-_3$ state. The main component of this state is a neutron $1p1h$ configuration, but $5/2^-_2$ state is found to be dominated by $2p2h$ components. This situation implies that the ratio of many neutron configurations in the fp shell can easily affect the level structure and the production cross section of each state. This can be also the explanation of the difference of the production cross sections of the $7/2^-$ states in the present experiment and the shell model calculations, which will be discussed in the next section.

Additionally, a $K = 3/2$ band with the oblate deformation is predicted by the AMD calculation [16]. The neutron configuration of this band is dominated by the $(f_{7/2})^{-1}$ configuration but the shape of this band is not spherical, resulting in the shape coexistence with three different shapes. One of the key points to distinguish the band head and band members of the third band is to obtain further information about the neutron configuration of these states and to investigate if the $3/2^-$ or $1/2^-$ state at 1155 keV is a member of this oblate band.

One of the results worth noting is that several $3/2^-$ or $1/2^-$ states are located around 1200 keV. This situation is not reproduced by the shell model calculations and $3/2^-$ or $1/2^-$ states are scattered over a wider energy range. The 1155 keV state is a candidate of the band head of third band, as mentioned above, but the nature or the shape of other two states with spin-parity of $3/2^-$ or $1/2^-$ at 1162 and 1209 keV still remains unknown. Especially the γ transition from the 1162 keV state is of interest. By the analysis of parallel momentum distribution, this state was found to be produced by neutron knockout from the $l = 1$ orbit and the 185 keV γ-ray was put on the top of the 977 keV state, one of the rotational band members. By the comparison with the shell model level scheme, the 977 keV state is thought to be a $7/2^-$ state. If the 1162 keV state is a member of the band built on the ground state, its spin should equal to or be larger than 5/2. This implies the 1162 keV state belongs to another band and the 185 keV transition, which had one of the strongest yields of all observed γ-rays, can be a strong interband transition. This is a major difference between the experimental results and shell model calculations.

6.2 Spectroscopic factors

In Table 5.3, the C^2S value deduced from the production cross section of each final states are shown. For the deduction of experimental C^2S values, the production cross sections were divided by single-particle knockout cross section σ_{sp} calculated in the eikonal reaction theory, the center-of-mass factor, and the empirical reduction factor R_S. Note that neutron knockout from specific orbit, shown as J^{π}_{eik}, was assumed in the calculation of σ_{sp}. This means that these experimental C^2S values are normalized and naively related to the occupation number of each single-particle orbit.

By the g-factor measurement, the spectroscopic factor of the $7/2^-$ isomeric state was estimated as $C^2S \simeq 0.4 \times 8 = 3.2$ [29]. As shown in Table 5.3, the spectroscopic factor of this state measured by the one-neutron knockout reaction in the present work is 3.37(26) and has good agreement with the previous result. This ensures the validity of the analysis procedure of the eikonal reaction theory and deduction of the spectroscopic factor including the parameters used in the calculations, described in §2.3.3.

In the present work, not only the ground state, but also the three excited states around 1200 keV are found to be produced by the neutron knockout from a $l = 1$ neutron single-particle orbit. Though the production cross section of the ground state can only be treated as the upper limit, the sum of the C^2S values for these states amounts to 1.64(26). This result can be interpreted as about 1.6 neutrons occupy the $p_{3/2}$ or $p_{1/2}$ orbits beyond the $N = 28$ shell gap in the ground state of ^{44}S. This is a direct observation of the quenching of $N = 28$ gap in this neutron-rich region.

Both experimental result and shell model calculations show the large production cross section of the $7/2^-_1$ isomeric state resulting from the knockout of a $f_{7/2}$ neutron. This is due to the large C^2S value $C^2S_{exp} = 3.37(26)$ compared to 2.57 (2.67) as calculated with the SDPF-MU (SDPF-U) interaction. In addition to this state, relatively large population of the $7/2^-$ state just below the neutron threshold is present both in experiment and calculation. Though the shell model calculations with the SDPF-MU (SDPF-U) interaction predict a C^2S value as 1.46 (1.87) for the $7/2^-_3$ state, experimental value is found to be much smaller, resulting in $C^2S_{exp} = 0.36(3)$ for the 2625 keV state. As discussed in the previous section, this $7/2^-$ state can be attributed as a member of the band constructed on the $5/2^-$ state which is characterized by the neutron $2p2h$ configuration predicted in the shell model calculations [43], or one of those on the $3/2^-$ state with oblate deformation characterized by the $(f_{7/2})^{-1}$ configuration suggested in the AMD calculation [16]. By comparing the wave function components of each state, it is found that the $1p1h$ and $2p2h$ neutron configuration are competing with each other in a few $7/2^-$ states around the neutron threshold of ^{43}S. This situation could result in a distribution of the spectroscopic strength over a few states around the neutron threshold of ^{43}S. Though states in the third band of ^{43}S are predicted to be the axialy deformed, the ground state of ^{44}S is predicted to be prolate deformed but γ-soft state due to configuration mixing rather than shape coexistence in beyond-mean-field calculation [39], or prolately deformed state with possible triaxial or γ-soft nature in the shell model calculation [15, 43]. These calculations imply the competition of a few deformed states or neutron configurations in the ground state of ^{44}S. The C^2S values can be calculated as the overlap of the wave function of the ground state of ^{44}S and a neutron plus specific state of ^{43}S, naively. This qualitatively means that the wave functions of the excited states with higher excitation energies in ^{43}S can have more complex configurations, which can also be the applied to the ground state of ^{44}S.

As shown in Figure 5.13, the 2600 keV state was found to be best explained by neutron knockout from $l = 2$ orbit. In the present work, the model space of the shell model calculations was restricted to the fp shell and the sd shell below $N = 20$ shell gap was assumed to be fully occupied. With this truncation, the calculation of positive parity states is impossible. Although a direct comparison of the experimental excitation energy or the production cross section of this state with the theoretical calculations can not be achieved, the appearance of a positive parity state may suggest the decrease of the neutron occupation under $N = 20$ shell gap , which was already pointed out in the neutron rich Si isotopes.

Finally, the shell gap between neutron $f_{7/2}$ and $p_{3/2}$ orbits can be estimated from the excitation energies of the $7/2^-$ and $3/2^-$ states and the C^2S values of the one-neutron knockout reaction:

$$\varepsilon = \frac{\sum_i C^2S_i \times E_i}{\sum_i C^2S_i}. \tag{6.1}$$

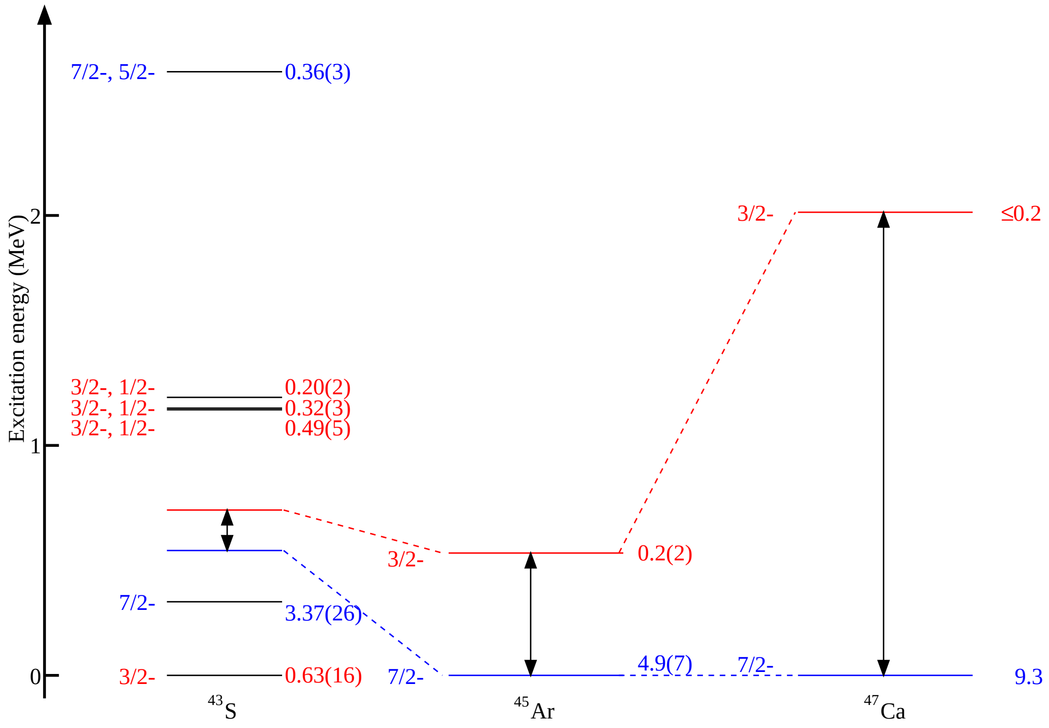
Excitation energy (MeV)
2
1
0
7/2-, 5/2-
0.36(3)
3/2-, 1/2-
0.20(2)
3/2-, 1/2-
0.32(3)
3/2-, 1/2-
0.49(5)
7/2-
3.37(26)
3/2-
0.63(16)
3/2-
0.2(2)
7/2-
4.9(7)
3/2-
≤0.2
7/2-
9.3
43S
45Ar
47Ca

Figure 6.3: Systematics of the C^2S weighted energy centroids of the $f_{7/2}$ and $p_{3/2}$ orbits. $7/2^-$ and $3/2^-$ states with experimental C^2S values available for one-neutron knockout reaction are plotted for ^{47}Ca [110], ^{45}Ar [111], and ^{43}S (this stady). The spin-parity and the experimental C^2S value are shown in the lefthand side and righthand side of each state. Blue and red lines are the centroids for $f_{7/2}$ and $p_{3/2}$ orbits, respectively.

By using the values in Table 5.3, the C^2S weighted energy centroids of the $f_{7/2}$ and $p_{3/2}$ orbits are calculated as 543 and 719 keV, respectively. Note that only the angular momentum value can be extracted for each state by the analysis on momentum distribution, and the spin of each state was not firmly assigned. In this calculation, states at 320 and 2625 keV are assumed to be $7/2^-$ and those at 0, 1155, 1162, and 1209 keV are assigned as $3/2^-$. In looking at neighboring nuclei, the experimental result of one-neutron knockout reaction from ^{48}Ca and ^{46}Ar were reported. In ^{47}Ca [110], the ground state is assigned as $7/2^-$ and has almost full strength, $C^2S \sim 8$, of neutron knockout from $f_{7/2}$ orbit. Several excited states are observed in this nucleus but only one state, at 2014 keV, has a firm spin-parity assignment of $3/2^-$. Though other possible $7/2^-$ or $3/2^-$ states in ^{47}Ca can affect the calculation of above mentioned ε, the energy centroid of the $7/2^-$ and $3/2^-$ orbitals can be estimated as 0 and 2014 keV, which results in a energy difference of the $f_{7/2}$ and $p_{3/2}$ orbits as 2014 keV. In ^{45}Ar [111], only the experimental production cross sections of the $7/2^-$ ground state and a $3/2^-$ excited state at 532 keV are available so far, which again results in a 532 keV energy difference of two neutron orbits around the $N = 28$ gap. Note that for this nucleus, the observed spectroscopic factor of the $7/2^-$ and $3/2^-$ states are 4.9(7) and 0.2(2), respectively, and the spectroscopic factor is defined as σ_{exp}/σ_{th}. This systematics, shown in Figure 6.3, can qualitatively reveal that a rapid decrease of the $N = 28$ gap occurs along the $N = 28$ isotone line just below ^{48}Ca and this gap is still narrowing going down to ^{44}S region. Again note that this estimation can be affected by other unobserved $7/2^-$ or $3/2^-$ states and ideally all the states with full C^2S strength of neutron knockout from $f_{7/2}$ and $p_{3/2}$ orbit should be included. The strict definition of the energy centroid was described as [112]

$$\epsilon = \frac{\sum_f (E_0 - E_f^{(-)}) C^2 S_f^{(-)} + (2J_f + 1)(E_f^{(+)} - E_0) C^2 S_f^{(+)}}{\sum_f C^2 S_f^{(-)} + (2J_f + 1) C^2 S_f^{(+)}}, \tag{6.2}$$

where E_0 is the nucleus of interest with mass A and $E_f^{(\pm)}$ and $C^2S_f^{(\pm)}$ are the energy and the spectroscopic factor of the final state of mass $A \pm 1$ nucleus. This formalization includes the strength both below and above the Fermi surface, which means it is more strict but two reaction should be observed, a neutron adding reaction as ^{44}S→^{45}S in this work for instance.

For the better understanding of the mechanism of the quenching of $N = 28$ shell gap observed in the present work, some additional shell model calculations have been performed. First, calculations with the SDPF-MU interaction for Ca and Ar isotopes have been performed. In these calculations, C^2S values of ^{48}Ca→^{47,49}Ca, ^{46}Ar→^{45,47}Ar, and ^{44}S→^{43,45}S channels are deduced. By the excitation energies and the C^2S values of $3/2^-$ and $7/2^-$ states, effective single particle energies (ESPE) of $p_{3/2}$ and $f_{7/2}$ orbits can be calculated as the energy centroids of $3/2^-$ and $7/2^-$ states, written as Equation (6.2). The result is shown as Table 6.1, telling that the SDPF-MU interaction can predict the quenching of $N = 28$ shell gap.

Then shell model calculations for ^{43}S with three different interactions made from the SDPF-MU interactions have been additionally performed. One of the interactions used is the original SDPF-MU interaction, same as the calculation presented before. Here this result is called as "tensor". Second one, denoted as "no tensor", is based on the SDPF-MU interaction but all the tensor terms are removed. In the third one, mentioned as "no X tensor", not all the tensor terms but those of only cross-shell tensor terms, interactions between a nucleon in sd-shell and one in fp-shell, are removed. In looking into the resultant level scheme of ^{43}S by using these three

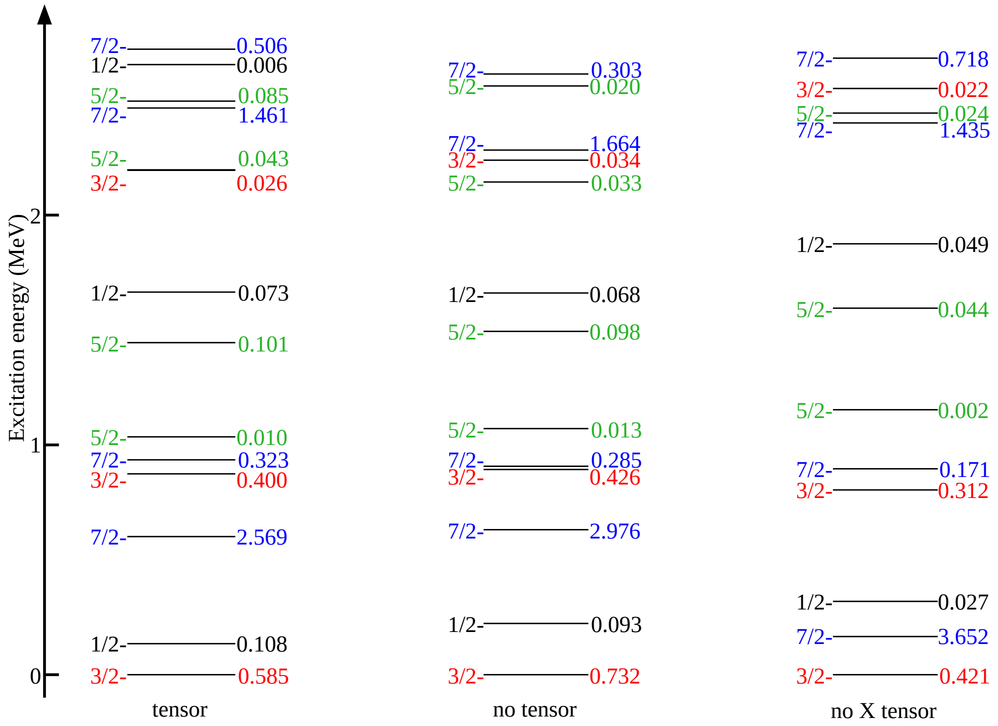
Excitation energy (MeV)
0
1
2
7/2- 0.506
1/2- 0.006
5/2- 0.085
7/2- 1.461
5/2- 0.043
3/2- 0.026
1/2- 0.073
5/2- 0.101
5/2- 0.010
7/2- 0.323
3/2- 0.400
7/2- 2.569
1/2- 0.108
3/2- 0.585
tensor
7/2- 0.303
5/2- 0.020
7/2- 1.664
3/2- 0.034
5/2- 0.033
1/2- 0.068
5/2- 0.098
5/2- 0.013
7/2- 0.285
3/2- 0.426
7/2- 2.976
1/2- 0.093
3/2- 0.732
no tensor
7/2- 0.718
3/2- 0.022
5/2- 0.024
7/2- 1.435
1/2- 0.049
5/2- 0.044
5/2- 0.002
7/2- 0.171
3/2- 0.312
1/2- 0.027
7/2- 3.652
3/2- 0.421
no X tensor

Figure 6.4: Influence of the tensor force on the level scheme of ^{43}S. The spin-parity and the C^2S values are shown in each level up to around 2.7 MeV. Tensor, no tensor, and no X tensor means the level scheme calculated with the original SDPF-MU interaction, the interaction without all the tensor terms, and the one without cross shell tensor terms, respectively.

Table 6.1: Calculated ESPEs of $p_{3/2}$ and $f_{7/2}$ orbits in Ca, Ar, and S isotopes at $N = 28$.

ESPE [MeV]	Ca	Ar	S
$p_{3/2}$	-4.88	-3.72	-2.78
$f_{7/2}$	-9.76	-7.67	-5.44
$N = 28$ gap	4.88	3.96	2.65

Table 6.2: Calculated C^2S sum of three different interactions.

	tensor	no tensor	no X tensor
$1/2^-$	0.19	0.19	0.09
$3/2^-$	1.32	1.45	0.95
$5/2^-$	0.27	0.24	0.13
$7/2^-$	5.42	5.45	6.27
sum	7.20	7.32	7.44

interactions, shown as Figure 6.4, there is not a drastic difference with each other. On the other hand, calculated C^2S values for the ^{44}S→^{43}S channel are different implying the change of the neutron occupancy in these results. Table 6.2 shows the sum of the C^2S values of the 10 lowest states for each spin-parity. Roughly speaking, it corresponds to the sum for the states up to around 4.5 MeV. Though there is only a subtle difference of the C^2S sum of tensor and no tensor results, no X tensor result has a remarkable difference. Especially, the C^2S sum of $7/2^-$ states is larger than those of the other results by about 0.8 and the sum of $3/2^-$ states is smaller by about 0.4. These results suggest that the stronger cross-shell tensor force reproduces the large neutron occupation beyond $N = 28$ shell gap observed expeimentally.

Chapter 7

Summary and outlook

This work investigated the nuclear structure and the mechanism of the structural change in the neutron-rich sulfur isotope in order to understand the breakdown of the $N = 28$ shell closure. For this purpose, one-neutron knockout reaction was utilized, which can deduce the shell evolution of the neutron single-particle orbits.

Prior to this work, only part of the level scheme of ^{43}S was known. By this thesis work, the full level scheme of ^{43}S was constructed for the first time, especially the coincident prompt γ-ray with the decay of the isomeric state was confirmed. Owing to this level scheme, the production cross section of each level by the one-neutron knockout reaction was also determined. Analysis on the parallel momentum distribution for each final state was also performed, resulting in the assignment of the spin-parity.

The observed strength of neutron knockout from $l = 1$ orbit was significantly larger than theoretically predicted values and $3/2^-$ or $1/2^-$ states were concentrated around 1.2 MeV in ^{43}S. This can be attributed as the neutron excitation above the $N = 28$ shell gap in the ground state of ^{44}S, which was one of the direct observations of the quenching of this shell gap. Though the shell model calculations without tensor or cross-shell tensor terms, it was pointed out that the stronger cross-shell tensor force describes the large neutron occupation beyond $N = 28$ shell gap like observed in the present work. Also the strength of the production of $7/2^-$ state just below the neutron threshold of ^{43}S was found to be rather small compared to the shell model calculations. This can imply that many configuration of the wave function participate in both the higher excited states in ^{43}S and the ground state of ^{44}S, resulting in the scattering of the strength. Additionally, an excited state well explained by the neutron knockout from the $l = 2$ orbit was also found. This result implies the change of the neutron occupation under $N = 20$ shell gap, which was previously pointed out in the neutron-rich Si isotopes.

Experimentally, the obvious next steps in this investigation would be the search of excited states predicted in the theoretical work but not observed in this work. For example, the $5/2^-_1$ state, the predicted band member of the rotational band on the ground state, would have small production cross section of this reaction channel. Related to this, the placement of the $1/2^-_1$ state was unfortunately tentative in this work. The firm observation of this state can be the direct confirmation of the prolate deformation of the ground state due to the special order of the spins of the excited states. For this purpose, not only taking a benefit of high statistics, but also utilizing the different reaction probes could be powerful methods. For example, the (p, p') reaction can excite both the single-particle and the collective states simultaneously. The proposed level scheme in this work is not perfect but large part of the structure of ^{43}S was revealed. In this stage, such kind of reaction producing all kinds of states can be useful to search the missing transition in this work. Other than the ground state band, a band above the 1155 keV state can be the candidate of the third band predicted in shell model and AMD calculations. Because these calculations predict controversial deformation about this band, experimental measurement of the deformation parameters of this band is one of the fascinating subject. Though such kind of measurement should be tough and quite high statistics must be necessary, one of the possible tool could be the sub-barrier Coulomb excitation experiment, which can be sensitive to the sign of the quadrupole moment of each state. When we can achieve very neutron-rich phosphor isotopes with $N \geq 29$, another interesting experiment could be the observation of β and β-n decays, which would give us the opportunity to distinguish the unnatural parity state by comparing the observed decay scheme in these two channels. This information would shed light to the change of occupation in the neutron *sd* shell.

For the theoretical side, one of the obvious step could be the expansion of the model space containing neutron *sd* shell. Because many kinds of correlations are thought to participate in the shell structure change in this region, some attempts to arbitrarily change the interactions in the nucleus and compare the resulting spectroscopic information may derive another possible features of the structure of these nuclei.

Acknowledgements

First and foremost, I would like to express my sincere appreciation to my supervisors, Prof. Dr. Hiroyoshi Sakurai and Dr. Kathrin Wimmer. Prof. Sakurai introduced me this interesting research field. He gave me a lot of opportunities to take part in the experiments both in Japan and overseas. Also his very wide range of curiosity and knowledge of the nuclear physics and other region of science inspired me very much. I have learned so many things from him during my six-year study in his group. Dr. Wimmer gave me the great opportunity to participate in the experiment of this thesis work. I have been very happy to work for this experiment because not only of the interesting physics but also of utilizing the sophisticated detectors. Her deep knowledge of the nuclear physics and enthusiastic attitude to tackle the frontier of the nuclear physics are my best model as the researcher. I really appreciate her great patience against my little understanding of the nuclear physics, too poor creativity, and the terrible English skill.

I would like to express my great appreciation to all the collaborators of this experiment for their contributions. Especially, I would like to thank Prof. Dr. Daniel Bazin, Dr. Peter Bender, Prof. Dr. Alexandra Gade, Prof. Dr. Kirby W. Kemper, Dr. Shinsuke Ota, Dr. Dirk Weisshaar, Dr. Philipp Schrock, Mr. Noritaka Kitamura, Dr. Joe Belarge, Mr. Brandon Elman, and Dr. Eric Lunderberg. Their advice and encouragement helped me very much, especially during the beam time.

My gratitude goes to all of the members in the nuclear physics experiment (NEX) group in the University of Tokyo: Prof. Dr. H. Sakurai, Dr. K. Wimmer, Dr. Megumi Niikura, Dr. Zhengyu Xu, Dr. Nobuyuki Kobayashi, Mr. Ryo Taniuchi, Mr. Keishi Matsui, Mr. Takuya Miyazaki, Mr. Shumpei Koyama, Mr. Takeshi Saito, Mr. Shunsuke Nagamine, Mr. Takumi Koiwai, Prof. Dr. Ryugo S. Hayano, Dr. Takatoshi Suzuki, Dr. Hideyuki Tatsuno, Mr. Yuya Fujiwara, Dr. Hexi Shi, Dr. Tadashi Hashimoto, Dr. Koichi Todoroki, Dr. Takumi Kobayashi, Mr. Hiroyuki Yamada, Dr. Yohei Murakami, Dr. Yuni Watanabe, Mr. Hiroshi Horii, Mr. Takashi Ando, and Dr. Yosuke Watanabe. I have really enjoyed my Ph.D. life here in the University of Tokyo.

I would like to express my gratitude to the thesis examiners, Prof. Dr. Nobuaki Imai, Prof. Dr. Aya Bamba, Prof. Dr. Kentaro Yako, Prof. Dr. Haozhao Liang, and Prof. Dr. Kyoichiro Ozawa, for the many valuable discussions on this thesis work.

Last but not least, I would like to thank my family and all my friends for their continuous supports and encouragements.

Bibliography

[1] E. Rutherford, Philosophical Magazine Series 6 **21**, 669 (1911).

[2] H. Gegier, E. Marsden, and E. Rutherford, Proceedings of the Royal Society of London. Series A, Containing Papers of a Mathematical and Physical Character **82**, 495 (1909).

[3] Isotope Science Facility at Michigan State University: Upgrade of the NSCL rare isotope research capabilities, MSU preprint MSUCL-1345, 2006.

[4] C. F. v. Weizsäcker, Zeitschrift für Physik **96**, 431 (1935).

[5] B. A. Brown, "Lecture Notes in Nuclear Structure Physics", 2010.

[6] G. Audi, International Journal of Mass Spectrometry **251**, 85 (2006).

[7] A. Bohr and B. R. Motteleson, *Nuclear Structre* (W. A. Benjamin Inc., 1969).

[8] M. G. Mayer, Physical Review **74**, 235 (1948).

[9] M. G. Mayer, Physical Review **78**, 22 (1950).

[10] O. Haxel, J. H. D. Jensen, and H. E. Suess, Physical Review **75**, 1766 (1949).

[11] P. Ring, Progress in Particle and Nuclear Physics **37**, 193 (1996).

[12] N. Kaiser and W. Weise, Nuclear Physics A **804**, 60 (2008).

[13] O. Sorlin and M.-G. Porquet, Progress in Particle and Nuclear Physics **61**, 602 (2008).

[14] O. Sorlin and M. G. Porquet, Physica Scripta **T152**, 014003 (2013).

[15] Y. Utsuno, T. Otsuka, B. A. Brown, M. Honma, T. Mizusaki, and N. Shimizu, Physical Review C **86**, 051301(R) (2012).

[16] M. Kimura, Y. Taniguchi, Y. Kanada-En'yo, H. Horiuchi, and K. Ikeda, Physical Review C **87**, 011301 (2013).

[17] K. Heyde and J. L. Wood, Reviews of Modern Physics **83**, 1467 (2011).

[18] A. Gade and S. N. Liddick, Journal of Physics G: Nuclear and Particle Physics **43**, 024001 (2016).

[19] D. Santiago-Gonzalez, I. Wiedenhöver, V. Abramkina, M. L. Avila, T. Baugher, D. Bazin, B. A. Brown, P. D. Cottle, A. Gade, T. Glasmacher, K. W. Kemper, S. McDaniel, A. Rojas, A. Ratkiewicz, R. Meharchand, E. C. Simpson, J. A. Tostevin, A. Volya, and D. Weisshaar, Physical Review C **83**, 061305 (2011).

[20] O. Sorlin, D. Guillemaud-Mueller, a. C. Mueller, V. Borrel, S. Dogny, F. Pougheon, K. L. Kratz, H. Gabelmann, B. Pfeiffer, A. Wöhr, W. Ziegert, Y. E. Penionzhkevich, S. M. Lukyanov, V. S. Salamatin, R. Anne, C. Borcea, L. K. Fifield, M. Lewitowicz, M. G. Saint-Laurent, D. Bazin, C. Détraz, F. K. Thielemann, and W. Hillebrandt, Physical Review C **47**, 2941 (1993).

[21] T. Glasmacher, B. A. Brown, M. J. Chromik, P. D. Cottle, M. Fauerbach, R. W. Ibbotson, K. W. Kemper, D. J. Morrissey, H. Scheit, D. W. Sklenicka, and M. Steiner, Physics Letters B **395**, 163 (1997).

[22] F. Sarazin, H. Savajols, W. Mittig, F. Nowacki, N. A. Orr, Z. Ren, P. Roussel-Chomaz, G. Auger, D. Baiborodin, A. V. Belozyorov, C. Borcea, E. Caurier, Z. Dlouhý, A. Gillibert, A. S. Lalleman, M. Lewitowicz, S. M. Lukyanov, F. de Oliveira, Y. E. Penionzhkevich, D. Ridikas, H. Sakuraï, O. Tarasov, and A. de Vismes, Physical Review Letters **84**, 5062 (2000).

[23] D. Sohler, Z. Dombrádi, J. Timár, O. Sorlin, F. Azaiez, F. Amorini, M. Belleguic, C. Bourgeois, C. Donzaud, J. Duprat, D. Guillemaud-Mueller, F. Ibrahim, J. A. Scarpaci, M. Stanoiu, M. J. Lopez, M. G. Saint-Laurent, F. Becker, F. Sarazin, C. Stodel, G. Voltolini, S. M. Lukyanov, V. Maslov, Y. E. Penionzhkevich, M. Girod, S. Péru, F. Nowacki, G. Sletten, R. Lucas, C. Theisen, D. Baiborodin, Z. Dlouhy, J. Mrazek, C. Borcea, A. Bauchet, C. J. Moore, and M. J. Taylor, Physical Review C **66**, 054302 (2002).

[24] L. Cáceres, D. Sohler, S. Grévy, O. Sorlin, Z. Dombrádi, B. Bastin, N. L. Achouri, J. C. Angélique, F. Azaiez, D. Baiborodin, R. Borcea, C. Bourgeois, A. Buta, A. Bürger, R. Chapman, J. C. Dalouzy, Z. Dlouhy, A. Drouard, Z. Elekes, S. Franchoo, L. Gaudefroy, S. Iacob, B. Laurent, M. Lazar, X. Liang, E. Liénard, J. Mrazek, L. Nalpas, F. Negoita, F. Nowacki, N. A. Orr, Y. Penionzhkevich, Z. Podolyák, F. Pougheon, A. Poves, P. Roussel-Chomaz, M. G. Saint-Laurent, M. Stanoiu, and I. Stefan, Physical Review C **85**, 024311 (2012).

[25] J. J. Parker, I. Wiedenhöver, P. D. Cottle, J. Baker, D. McPherson, M. A. Riley, D. Santiago-Gonzalez, A. Volya, V. M. Bader, T. Baugher, D. Bazin, A. Gade, T. Ginter, H. Iwasaki, C. Loelius, C. Morse, F. Recchia, D. Smalley, S. R. Stroberg, K. Whitmore, D. Weisshaar, A. Lemasson, H. L. Crawford, A. O. Macchiavelli, and K. Wimmer, Physical Review Letters **118**, 052501 (2017).

[26] Y. Utsuno, N. Shimizu, T. Otsuka, T. Yoshida, and Y. Tsunoda, Physical Review Letters **114**, 032501 (2015).

[27] S. Grévy, F. Negoita, I. Stefan, N. L. Achouri, J. C. Angélique, B. Bastin, R. Borcea, A. Buta, J. M. Daugas, F. De Oliveira, O. Giarmana, C. Jollet, B. Laurent, M. Lazar, E. Liénard, F. Maréchal, J. Mrázek, D. Pantelica, Y. Penionzhkevich, S. Piétri, O. Sorlin, M. Stanoiu, C. Stodel, and M. G. St-Laurent, European Physical Journal A **25**, 111 (2005).

[28] C. Force, S. Grévy, L. Gaudefroy, O. Sorlin, L. Cáceres, F. Rotaru, J. Mrazek, N. L. Achouri, J. C. Angélique, F. Azaiez, B. Bastin, R. Borcea, A. Buta, J. M. Daugas, Z. Dlouhy, Z. Dombrádi, F. De Oliveira, F. Negoita, Y. Penionzhkevich, M. G. Saint-Laurent, D. Sohler, M. Stanoiu, I. Stefan, C. Stodel, and F. Nowacki, Physical Review Letters **105**, 102501 (2010).

[29] L. Gaudefroy, J. M. Daugas, M. Hass, S. Grévy, C. Stodel, J. C. Thomas, L. Perrot, M. Girod, B. Rossé, J. C. Angélique, D. L. Balabanski, E. Fiori, C. Force, G. Georgiev, D. Kameda, V. Kumar, R. L. Lozeva, I. Matea, V. Méot, P. Morel, B. S. N. Singh, F. Nowacki, and G. Simpson, Physical Review Letters **102**, 092501 (2009).

[30] D. Kameda, T. Kubo, T. Ohnishi, K. Kusaka, A. Yoshida, K. Yoshida, M. Ohtake, N. Fukuda, H. Takeda, K. Tanaka, N. Inabe, Y. Yanagisawa, Y. Gono, H. Watanabe, H. Otsu, H. Baba, T. Ichihara, Y. Yamaguchi, M. Takechi, S. Nishimura, H. Ueno, A. Yoshimi, H. Sakurai, T. Motobayashi, T. Nakao, Y. Mizoi, M. Matsushita, K. Ieki, N. Kobayashi, K. Tanaka, Y. Kawada, N. Tanaka, S. Deguchi, Y. Satou, Y. Kondo, T. Nakamura, K. Yoshinaga, C. Ishii, H. Yoshii,

Y. Miyashita, N. Uematsu, Y. Shiraki, T. Sumikama, J. Chiba, E. Ideguchi, A. Saito, T. Yamaguchi, I. Hachiuma, T. Suzuki, T. Moriguchi, A. Ozawa, T. Ohtsubo, M. A. Famiano, H. Geissel, A. S. Nettleton, O. B. Tarasov, D. Bazin, B. M. Sherrill, S. L. Manikonda, and J. A. Nolen, Physical Review C **86**, 054319 (2012).

[31] R. Chevrier, J. M. Daugas, L. Gaudefroy, Y. Ichikawa, H. Ueno, M. Hass, H. Haas, S. Cottenier, N. Aoi, K. Asahi, D. L. Balabanski, N. Fukuda, T. Furukawa, G. Georgiev, H. Hayashi, H. Iijima, N. Inabe, T. Inoue, M. Ishihara, Y. Ishii, D. Kameda, T. Kubo, T. Nanao, G. Neyens, T. Ohnishi, M. M. Rajabali, K. Suzuki, H. Takeda, M. Tsuchiya, N. Vermeulen, H. Watanabe, and A. Yoshimi, Physical Review Letters **108**, 162501 (2012).

[32] R. Ibbotson, T. Glasmacher, P. Mantica, and H. Scheit, Physical Review C **59**, 642 (1999).

[33] L. A. Riley, P. Adrich, T. R. Baugher, D. Bazin, B. A. Brown, J. M. Cook, P. D. Cottle, C. A. Diget, A. Gade, D. A. Garland, T. Glasmacher, K. E. Hosier, K. W. Kemper, A. Ratkiewicz, K. P. Siwek, J. A. Tostevin, and D. Weisshaar, Physical Review C **80**, 037305 (2009).

[34] T. Mijatović, N. Kobayashi, H. Iwasaki, D. Bazin, J. Belarge, P. Bender, B. Brown, A. Dewald, R. Elder, B. Elman, A. Gade, M. Grinder, T. Haylett, S. Heil, C. Loelius, B. Longfellow, E. Lunderberg, M. Mathy, K. Whitmore, and D. Weisshaar, Physical Review Letters **121**, 012501 (2018).

[35] J. Fridmann, I. Wiedenhöver, A. Gade, L. T. Baby, D. Bazin, B. A. Brown, C. M. Campbell, J. M. Cook, P. D. Cottle, E. Diffenderfer, D. C. Dinca, T. Glasmacher, P. G. Hansen, K. W. Kemper, J. L. Lecouey, W. F. Mueller, E. Rodriguez-Vieitez, J. R. Terry, J. A. Tostevin, K. Yoneda, and H. Zwahlen, Physical Review C **74**, 034313 (2006).

[36] L. A. Riley, P. Adrich, T. R. Baugher, D. Bazin, B. A. Brown, J. M. Cook, P. D. Cottle, C. A. Diget, A. Gade, D. A. Garland, T. Glasmacher, K. E. Hosier, K. W. Kemper, T. Otsuka, W. D. M. Rae, A. Ratkiewicz, K. P. Siwek, J. A. Tostevin, Y. Utsuno, and D. Weisshaar, Physical Review C **78**, 011303 (2008).

[37] L. A. Riley, P. Adrich, N. Ahsan, T. R. Baugher, D. Bazin, B. A. Brown, J. M. Cook, P. D. Cottle, C. A. Diget, A. Gade, T. Glasmacher, K. E. Hosier, K. W. Kemper, A. Ratkiewicz, K. P. Siwek, J. A. Tostevin, A. Volya, and D. Weisshaar, Physical Review C **86**, 047301 (2012).

[38] J. L. Egido, M. Borrajo, and T. R. Rodríguez, Phys. Rev. Lett. **116**, 052502 (2016).

[39] T. R. Rodríguez and J. L. Egido, Physical Review C **84**, 051307 (2011).

[40] Z. P. Li, J. M. Yao, D. Vretenar, T. Nikšić, H. Chen, and J. Meng, Physical Review C **84**, 054304 (2011).

[41] S. Péru and M. Martini, European Physical Journal A **50**, 88 (2014).

[42] X. Y. Wu and X. R. Zhou, Physical Review C **92**, 054321 (2015).

[43] R. Chevrier and L. Gaudefroy, Physical Review C **89**, 051301 (2014).

[44] T. Werner, J. Sheikh, W. Nazarewicz, M. Strayer, A. Umar, and M. Misu, Physics Letters B **333**, 303 (1994).

[45] I. Hamamoto, Physical Review C **79**, 014307 (2009).

[46] N. A. Smirnova, K. Heyde, B. Bally, F. Nowacki, and K. Sieja, Physical Review C **86**, 034314 (2012).

[47] Y. Suzuki, H. Nakada, and S. Miyahara, Physical Review C **94**, 024343 (2016).

[48] D. Tarpanov, H. Liang, N. V. Giai, and C. Stoyanov, Physical Review C **77**, 054316 (2008).

[49] M. Moreno-Torres, M. Grasso, H. Liang, V. De Donno, M. Anguiano, and N. Van Giai, Physical Review C **81**, 064327 (2010).

[50] Z. Wang, Q. Zhao, H. Liang, and W. H. Long, Physical Review C **98**, 034313 (2018).

[51] D. J. Gross and F. Wilczek, Physical Review Letters **30**, 1343 (1973).

[52] H. D. Politzer, Physical Review Letters **30**, 1346 (1973).

[53] S. Weinberg, *The Quantum Theory of Field Volume II* (Cambridge University Press, 1996).

[54] C. A. Bertulani, *Nuclear Physics in a Nutshell* (Princeton University Press, 2007).

[55] T. Otsuka, T. Suzuki, R. Fujimoto, H. Grawe, and Y. Akaishi, Physical Review Letters **95**, 232502 (2005).

[56] A. L. Fetter and J. D. Walecka, *Quantum Theory of Many-Particle Systems* (Dover Publications Inc., 2003).

[57] B. Alex Brown, Phys. Rev. C **58**, 220 (1998).

[58] D. J. Griffiths, *Introduction to Quantum Mechanics* (Cambridge University Press, 2005).

[59] F. Nowacki and A. Poves, Physical Review C **79**, 014310 (2009).

[60] T. Otsuka, T. Suzuki, M. Honma, Y. Utsuno, N. Tsunoda, K. Tsukiyama, and M. Hjorth-Jensen, Physical Review Letters **104**, 012501 (2010).

[61] P. Hansen and J. Tostevin, Annual Review of Nuclear and Particle Science **53**, 219 (2003).

[62] A. Gade and T. Glasmacher, Progress in Particle and Nuclear Physics **60**, 161 (2008).

[63] A. E. L. Dieperink and T. d. Forest, Physical Review C **10**, 543 (1974).

[64] A. M. Mukhamedzhanov and A. S. Kadyrov, Physical Review C **82**, 051601 (2010).

[65] R. J. Glauber, *Lectures in Theoretical Physics* (Interscience, 1959).

[66] D. Bohm, *Quantum Theory* (Prentice-Hall, 1951).

[67] S. R. Stroberg, "SINGLE-PARTICLE STRUCTURE OF NEUTRON-RICH SILICON ISOTOPES AND THE BREAKDOWN OF THE N=28 SHELL CLOSURE", PhD thesis (Michigan State University, 2014).

[68] M. Hussein, R. Rego, and C. Bertulani, Physics Reports **201**, 279 (1991).

[69] L. Ray, Physical Review C **20**, 1857 (1979).

[70] C. A. Bertulani and A. Gade, Computer Physics Communications **175**, 372 (2006).

[71] J. A. Tostevin, Journal of Physics G: Nuclear and Particle Physics **25**, 735 (1999).

[72] P. Renberg, D. Measday, M. Pepin, P. Schwaller, B. Favier, and C. Richard-Serre, Nuclear Physics A **183**, 81 (1972).

[73] S. Kox, A. Gamp, C. Perrin, J. Arvieux, R. Bertholet, J. F. Bruandet, M. Buenerd, R. Cherkaoui, A. J. Cole, Y. El-Masri, N. Longequeue, J. Menet, F. Merchez, and J. B. Viano, Physical Review C **35**, 1678 (1987).

[74] V. Maddalena, T. Aumann, D. Bazin, B. A. Brown, J. A. Caggiano, B. Davids, T. Glasmacher, P. G. Hansen, R. W. Ibbotson, A. Navin, B. V. Pritychenko, H. Scheit, B. M. Sherrill, M. Steiner, J. A. Tostevin, and J. Yurkon, Phys. Rev. C **63**, 024613 (2001).

[75] B. A. Brown, P. G. Hansen, B. M. Sherrill, and J. A. Tostevin, Physical Review C **65**, 061601 (2002).

[76] A. Gade, P. Adrich, D. Bazin, M. D. Bowen, B. A. Brown, C. M. Campbell, J. M. Cook, T. Glasmacher, P. G. Hansen, K. Hosier, S. McDaniel, D. McGlinchery, A. Obertelli, K. Siwek, L. A. Riley, J. A. Tostevin, and D. Weisshaar, Physical Review C **77**, 044306 (2008).

[77] R. J. Philpott, W. T. Pinkston, and G. R. Satchler, Nuclear Physics A **119**, 241 (1968).

[78] G. R. Satchler, D. D. Armstrong, A. G. Blair, E. R. Flynn, R. J. Philpott, and W. T. Pinkston, Physical Review **182**, 1141 (1969).

[79] A. Moalem, J. F. A. Van Hienen, and E. Kashy, Nuclear Physics A **307**, 277 (1978).

[80] J. R. Terry, "PROBING SINGLE-PARTICLE STRUCTURE NEAR THE ISLAND OF INVERSION BY DIRECT NEUTRON KNOCKOUT FROM INTERMEDIATE-ENERGY BEAMS OF ^{26,28}Ne AND ^{30,32}Mg", PhD thesis (Michigan State University, 2006).

[81] J. Tostevin, Nuclear Physics A **682**, 320 (2001).

[82] J. A. Tostevin and A. Gade, Physical Review C **90**, 057602 (2014).

[83] J. P. Schiffer, C. R. Hoffman, B. P. Kay, J. A. Clark, C. M. Deibel, S. J. Freeman, A. M. Howard, A. J. Mitchell, P. D. Parker, D. K. Sharp, and J. S. Thomas, Physical Review Letters **108**, 022501 (2012).

[84] G. J. Kramer, H. P. Blok, and L. Lapikás, Nuclear Physics A **679**, 267 (2001).

[85] J. Lee, J. A. Tostevin, B. A. Brown, F. Delaunay, W. G. Lynch, M. J. Saelim, and M. B. Tsang, Physical Review C **73**, 044608 (2006).

[86] G. Audi, M. Wang, A. Wapstra, F. Kondev, M. MacCormick, X. Xu, and B. Pfeiffer, Chinese Physics C **36**, 1287 (2012).

[87] A. Gade and B. M. Sherrill, Physica Scripta **91**, 053003 (2016).

[88] D. J. Morrissey, Nuclear Physics A **616**, 45 (1997).

[89] D. Bazin, J. A. Caggiano, B. M. Sherrill, J. Yurkon, and A. Zeller, Nuclear Instruments and Methods in Physics Research, Section B: Beam Interactions with Materials and Atoms **204**, 629 (2003).

[90] S. Paschalis, I. Y. Lee, A. O. MacChiavelli, C. M. Campbell, M. Cromaz, S. Gros, J. Pavan, J. Qian, R. M. Clark, H. L. Crawford, D. Doering, P. Fallon, C. Lionberger, T. Loew, M. Petri, T. Stezelberger, S. Zimmermann, D. C. Radford, K. Lagergren, D. Weisshaar, R. Winkler, T. Glasmacher, J. T. Anderson, and C. W. Beausang, Nuclear Instruments and Methods in Physics Research, Section A: Accelerators, Spectrometers, Detectors and Associated Equipment **709**, 44 (2013).

[91] K. Wimmer, D. Barofsky, D. Bazin, L. M. Fraile, J. Lloyd, J. R. Tompkins, and S. J. Williams, Nuclear Instruments and Methods in Physics Research Section A: Accelerators, Spectrometers, Detectors and Associated Equipment **769**, 65 (2015).

[92] A. Stolz, T. Baumann, T. N. Ginter, D. J. Morrissey, M. Portillo, B. M. Sherrill, M. Steiner, and J. W. Stetson, Nuclear Instruments and Methods in Physics Research Section B: Beam Interactions with Materials and Atoms **241**, 858 (2005).

[93] D. J. Morrissey, B. M. Sherrill, M. Steiner, A. Stolz, and I. Wiedenhoever, Nuclear Instruments and Methods in Physics Research, Section B: Beam Interactions with Materials and Atoms **204**, 90 (2003).

[94] G. F. Knoll, *Radiation detection and measurement* (Wiley, 2000).

[95] J. Yurkon, D. Bazin, W. Benenson, D. J. Morrissey, B. M. Sherrill, D. Swan, and R. Swanson, Nuclear Instruments and Methods in Physics Research, Section A: Accelerators, Spectrometers, Detectors and Associated Equipment **422**, 291 (1999).

[96] N. H. Frank, "SPECTROSCOPY OF NEUTRON UNBOUND STATES IN NEUTRON RICH OXYGEN ISOTOPES", PhD thesis (Michigan State University, 2006).

[97] M. Berz, K. Joh, J. A. Nolen, B. M. Sherrill, and A. F. Zeller, Physical Review C **47**, 537 (1993).

[98] D. Weisshaar, D. Bazin, P. C. Bender, C. M. Campbell, F. Recchia, V. Bader, T. Baugher, J. Belarge, M. P. Carpenter, H. L. Crawford, M. Cromaz, B. Elman, P. Fallon, A. Forney, A. Gade, J. Harker, N. Kobayashi, C. Langer, T. Lauritsen, I. Y. Lee, A. Lemasson, B. Longfellow, E. Lunderberg, A. O. Macchiavelli, K. Miki, S. Momiyama, S. Noji, D. C. Radford, M. Scott, J. Sethi, S. R. Stroberg, C. Sullivan, R. Titus, A. Wiens, S. Williams, K. Wimmer, and S. Zhu, Nuclear Instruments and Methods in Physics Research, Section A: Accelerators, Spectrometers, Detectors and Associated Equipment **847**, 187 (2017).

[99] S800 Documentation, `https://wikihost.nscl.msu.edu/S800Doc/doku.php?id=start`.

[100] K. Wimmer, GrROOT software.

[101] Evaluated Nuclear Structure Data File, `http://www.nndc.bnl.gov/ensdf/`.

[102] S. Agostinelli, J. Allison, K. Amako, J. Apostolakis, H. Araujo, P. Arce, M. Asai, D. Axen, S. Banerjee, G. Barrand, F. Behner, L. Bellagamba, J. Boudreau, L. Broglia, A. Brunengo, H. Burkhardt, S. Chauvie, J. Chuma, R. Chytracek, G. Cooperman, G. Cosmo, P. Degtyarenko, A. Dell'Acqua, G. Depaola, D. Dietrich, R. Enami, A. Feliciello, C. Ferguson, H. Fesefeldt, G. Folger, F. Foppiano, A. Forti, S. Garelli, S. Giani, R. Giannitrapani, D. Gibin, J. Gómez

Cadenas, I. González, G. Gracia Abril, G. Greeniaus, W. Greiner, V. Grichine, A. Grossheim, S. Guatelli, P. Gumplinger, R. Hamatsu, K. Hashimoto, H. Hasui, A. Heikkinen, A. Howard, V. Ivanchenko, A. Johnson, F. W. Jones, J. Kallenbach, N. Kanaya, M. Kawabata, Y. Kawabata, M. Kawaguti, S. Kelner, P. Kent, A. Kimura, T. Kodama, R. Kokoulin, M. Kossov, H. Kurashige, E. Lamanna, T. Lampén, V. Lara, V. Lefebure, F. Lei, M. Liendl, W. Lockman, F. Longo, S. Magni, M. Maire, E. Medernach, K. Minamimoto, P. Mora de Freitas, Y. Morita, K. Murakami, M. Nagamatu, R. Nartallo, P. Nieminen, T. Nishimura, K. Ohtsubo, M. Okamura, S. O'Neale, Y. Oohata, K. Paech, J. Perl, A. Pfeiffer, M. G. Pia, F. Ranjard, A. Rybin, S. Sadilov, E. Di Salvo, G. Santin, T. Sasaki, N. Savvas, Y. Sawada, S. Scherer, S. Sei, V. Sirotenko, D. Smith, N. Starkov, H. Stoecker, J. Sulkimo, M. Takahata, S. Tanaka, E. Tcherniaev, E. Safai Tehrani, M. Tropeano, P. Truscott, H. Uno, L. Urban, P. Urban, M. Verderi, A. Walkden, W. Wander, H. Weber, J. P. Wellisch, T. Wenaus, D. C. Williams, D. Wright, T. Yamada, H. Yoshida, and D. Zschiesche, Nuclear Instruments and Methods in Physics Research Section A: Accelerators, Spectrometers, Detectors and Associated Equipment **506**, 250 (2003).

[103] L. A. Riley, UCGretina, unpublished.

[104] F. James and M. Roos, Computer Physics Communications **10**, 343 (1975).

[105] R. Brun and F. Rademakers, Nuclear Instruments and Methods in Physics Research Section A: Accelerators, Spectrometers, Detectors and Associated Equipment **389**, 81 (1997).

[106] M. S. Basunia, Nuclear Data Sheets **127**, 69 (2015).

[107] H. Weick, `http://web-docs.gsi.de/~weick/atima/`.

[108] O. B. Tarasov and D. Bazin, Nuclear Instruments and Methods in Physics Research Section B: Beam Interactions with Materials and Atoms **266**, 4657 (2008).

[109] NushellX, `http://www.garsington.eclipse.co.uk`.

[110] H. L. Crawford, A. O. Macchiavelli, P. Fallon, M. Albers, V. M. Bader, D. Bazin, C. M. Campbell, R. M. Clark, M. Cromaz, J. Dilling, A. Gade, A. Gallant, J. D. Holt, R. V. F. Janssens, R. Krücken, C. Langer, T. Lauritsen, I. Y. Lee, J. Menéndez, S. Noji, S. Paschalis, F. Recchia, J. Rissanen, A. Schwenk, M. Scott, J. Simonis, S. R. Stroberg, J. A. Tostevin, C. Walz, D. Weisshaar, A. Wiens, K. Wimmer, and S. Zhu, Physical Review C **95**, 064317 (2017).

[111] A. Gade, D. Bazin, C. A. Bertulani, B. A. Brown, C. M. Campbell, J. A. Church, D. C. Dinca, J. Enders, T. Glasmacher, P. G. Hansen, Z. Hu, K. W. Kemper, W. F. Mueller, H. Olliver, B. C. Perry, L. A. Riley, B. T. Roeder, B. M. Sherrill, J. R. Terry, J. A. Tostevin, and K. L. Yurkewicz, Phys. Rev. C **71**, 051301 (2005).

[112] M. Baranger, Nuclear Physics, Section A **149**, 225 (1970).